Back-contacted back-junction silicon solar cells

Krister Mangersnes

THESIS

submitted in partial fulfillment of the requirements for the degree of

philosophiæ doctor

Department of Physics
Faculty of Mathematics and Natural Sciences
University of Oslo

October 2010

Series of dissertations submitted to the
Faculty of Mathematics and Natural Sciences, University of Oslo
No. 1041

ISSN 1501-7710

Cover: Inger Sandved Anfinsen.
Printed in Norway: AIT Oslo AS.

Produced in co-operation with Unipub.
The thesis is produced by Unipub merely in connection with the
thesis defence. Kindly direct all inquiries regarding the thesis to the copyright
holder or the unit which grants the doctorate.

"The armies separated; and, it is said, Pyrrhus replied to one that gave him joy of his victory that one more such victory would utterly undo him. For he had lost a great part of the forces he brought with him, and almost all his particular friends and principal commanders; there were no others there to make recruits, and he found the confederates in Italy backward. On the other hand, as from a fountain continually flowing out of the city, the Roman camp was quickly and plentifully filled up with fresh men, not at all abating in courage for the loss they sustained, but even from their very anger gaining new force and resolution to go on with the war."

Lucius Mestrius Plutarchus, 46-120 AD

Til Leonore

Preface

This document concludes my nearly four years as a Ph.D. student at the Institute for Energy Technology (IFE), Department of Solar Energy. It also summarizes four years of intense learning and much frustration. We set off with the aim of making high-efficiency back-contacted back-junction silicon solar cells. Though a bit disappointing, we soon realized that this was too ambitious considering the time frame, the size of the project, and the available equipment at the time. Nevertheless, I think we ended up with some very interesting results, most of which is presented herein.

Several people have contributed to the scientific content of this thesis. Even more people have contributed to my social well-being as a Ph.D. student at IFE. I would therefore like to begin with thanking all you fine people at the Department of Solar Energy for making may stay at IFE a pleasant one. I would like to thank you for a remarkably large number of coffee breaks of respectful lengths, and for a decent number of "solar beers" at, some times, not so decent locations. Thank y'all.

On the scientific side, I would first and foremost like to thank my main supervisor, Sean Erik Foss. Your competence within an impressive lot of different fields together with your patience, kindness, and helpfulness have been invaluable for the conclusion of this thesis. I would also like to thank my three subsidiary supervisors, Aasmund Sudbø, Tor Arne Fjeldly, and Erik Stensrud Marstein. You have all contributed in different ways at different times in the process, and your help has been greatly acknowledged. Birger Retterstøl Olaisen is the fortunate combination of really clever and really helpful, and for that I am really grateful. I would like to thank Annett Thøgersen for performing transmission electron microscopy (TEM) for me. Jo Gjessing was most dedicated when performing ray tracing, a necessary piece to conclude the device simulation model. Jeyanthinath Mayandi was somehow always present in the lab, and always very helpful. I would also like to thank the head of the department, Arve Holt, for giving me the opportunity of pursuing this Ph.D., which was gratefully financed by the Research Council of Norway.

Last, but most of all I would like to thank my lovely partner, Michelle. I could not have done this without your loving support, patience, and compassion.

Oslo, October 2010 *Krister Mangersnes*

Abstract

Conventional silicon solar cells have a front-side contacted emitter. Back-contacted back-junction (BC-BJ) silicon solar cells, on the other hand, have both the complete metallization and the active diffused regions of both polarities on the backside. World-record efficiencies have already been demonstrated for this type of cell design in production, both on cell and module level. However, the production of these cells is both complex and costly, and a further cost reduction in fabrication is needed to make electricity from BC-BJ silicon solar cells cost-competitive with electricity on the grid ("grid-parity").

During the work with this thesis, we have investigated several important issues regarding BC-BJ silicon solar cells. The aim has been to reduce production cost and complexity while at the same time maintaining, or increasing, the already high conversion efficiencies demonstrated elsewhere. This has been pursued through experimental work as well as through numerical simulations and modeling. Six papers are appended to this thesis, two of which are still under review in scientific journals. In addition, two patents have been filed based on the work presented herein.

Experimentally, we have focused on investigating and optimizing single, central processing steps. A laser has been the key processing tool during most of the work. We have used the same laser both to structure the backside of the cell and to make holes in a double-layer of passivating amorphous silicon and silicon oxide, where the holes were opened with the aim of making local contact to the underlying silicon. The processes developed have the possibility of using a relatively cheap and industrially proven laser and obtain results better than most state-of-the-art laser technologies. During the work with the laser, we also developed a thermodynamic model that was able to predict the outcome from laser interaction with amorphous and crystalline silicon.

Alongside the experimental work, we have developed a two-dimensional BC-BJ silicon solar cell device model. The simulations, which are based on the finite

element method, have been performed with the ATLAS device simulator within the Silvaco simulation framework from Silvaco Inc., USA. The device model has been used to optimize the design of a BC-BJ silicon solar cell based on experimental results obtained during the work with this thesis. The model is able to quantitatively predict the performance of cells with different designs, qualities, and dimensions through optical and electrical simulations, and thereby giving us a good indication of the efficiency potential of the cell structure. It has also given us valuable insight into the physics determining the performance of a BC-BJ silicon solar cell. From this insight, important conclusions regarding the design rules of this type of solar cell devices could be drawn. Finally, the device model was used to investigate quantum mechanical tunneling mechanisms in the junction between the adjacent, highly-doped regions of opposite polarity on the backside of the cell. Through the simulations we found some simple design rules that need to be followed in order to avoid shunting-like behavior due to unwanted trap-assisted tunneling in the lateral tunneling junction. At the same time, band-to-band tunneling entails potential current breakdowns at low to moderate reverse biases. This implies that local hot-spots can be avoided since the heat distribution under reverse bias will be distributed throughout the whole junction area. Thus, by careful optimization and tailoring of the doping profiles, the tunneling may enable the use of back-junction silicon solar cells in a solar module without the need for bypass diodes.

Contents

Chapter 1

Introduction

In 2008, average worldwide power consumption was 15 TW[1]. Approximately 86 percent of this was derived from the combustion of fossil fuels[1]. Figure 1.1 shows the development of worldwide energy consumption from 1965 to 2008. The increase in energy consumption is simply a result of the world's growing population as well as an increase in the average gross domestic product (GDP) per capita[2]. The population is expected to reach 9 billion between 2040 and 2050[3]. In addition, the GDP per capita of a country is known to be directly proportional to its energy consumption per capita[2]. Thus, when taking into account that the average GDP per capita is growing even faster than the population, a drastic increase in the world's energy demand and consumption seems inevitable in the near future. This prospected increase in energy consumption is one of the biggest challenges faced by our generation. The global petroleum resources are limited. Some claim that the production of oil has already entered a terminal decline, and that proactive mitigation of an energy crisis might not be possible[4, 5]. More optimistic sources claim that peak oil will happen in 2020 or even later, and that it is possible to maintain a high production of oil several decades from now[6]. Nevertheless, the fossil resources are getting less accessible. Oil is pumped out from deeper wells. Oil rigs are being built in distant areas with hostile climate, and more technologically challenging solutions need to be implemented to withdraw the remaining resources. Not only does this increase the price of production, but

[1] This comprises commercially traded fuels only. Excluded, therefore, are fuels such as wood, peat, and animal waste which, though important in many countries, are unreliably documented in terms of consumption statistics. Also excluded are wind, geothermal, and solar power generation.

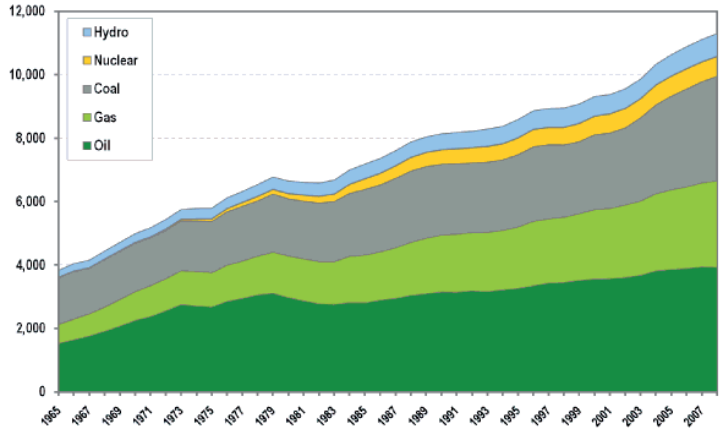

Figure 1.1: Worldwide energy consumption from from 1965 to 2008. The units are in million tons of oil equivalent. (Source: BP statistical review of world energy 2009[1]).

also the risk of serious oil spills like the Deepwater Horizon oil spill in the Gulf of Mexico in 2010[7]. Action needs to be taken to ensure a sustainable energy supply in the future, and there is already a strong ongoing political effort to allocate energy consumption away from fossil fuels. In addition, there has been much focus on the role of fossil fuels on global warming. According to the Intergovernmental Panel on Climate Change (IPCC) most of the observed temperature increase since the middle of the 20th century was very likely caused by increasing concentrations of greenhouse gases in the atmosphere resulting from human activity, such as fossil fuel burning and deforestation[8]. This has greatly increased focus on renewable energy both from a scientific and political point of view, and several sources of renewable energy are experiencing a significant growth in investments and installed capacity[9]. At the beginning of 2009, the total production capacity of renewable energy was 1.1 TW[2], with hydroelectric as the dominating source with a share of 83 %[9]. When evaluating the potential of different sources of

[2]This includes all power generating sources of renewable energy, but excludes heating sources such as solar collectors for hot water, geothermal, and biomass. Neither are renewable transport fuels, such as ethanol and biodiesel, included.

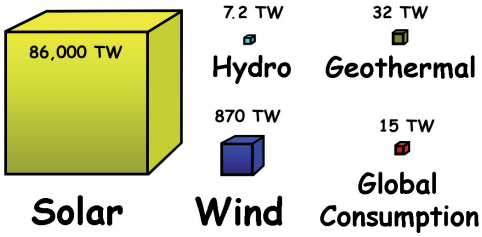

Figure 1.2: Available resources of renewable energy compared to the total energy consumption. (Source:
http://en.wikipedia.org/wiki/World_energy_resources_and_consumption)

renewable energy, one needs to take into account the available resources. Solar energy is, by far, the most abundant energy source. In Figure 1.2 the available total energy from different renewable energy sources are represented as the volume of different cubes and compared to the global average consumption. The available solar resources are about 6000 times the total global energy consumption. Thus, less than 0.02 % of the solar resources are sufficient to entirely replace fossil fuels and nuclear power as an energy source. Figure 1.3 shows worldwide insolation and the possible locations of large solar power plants that in total could provide the total global energy demand. At the end of 2009, the total installed capacity of solar power was 13 GWp[9][3]. This only accounts for approximately 0.04 % of the total global energy consumption. Still, grid-connected photovoltaic (PV) electricity has been the fastest growing energy source over the last ten years, with an average annual increase of about 42 %[9]. In other words, a doubled installed capacity every second year, see Figure 1.4. To be able to continue this growth, and to make solar power a major supplier in the future energy market, the technology needs to be cost competitive compared to alternative sources of energy.

[3]Wp, or watt-peak, is a measure of the nominal power of a solar cell device under standard illumination and operating conditions; a light intensity of 1000 W/m^2, with a spectrum similar to sunlight hitting the earth's surface at latitude 35°N in the summer (airmass 1.5) and a temperature of 25 °C.

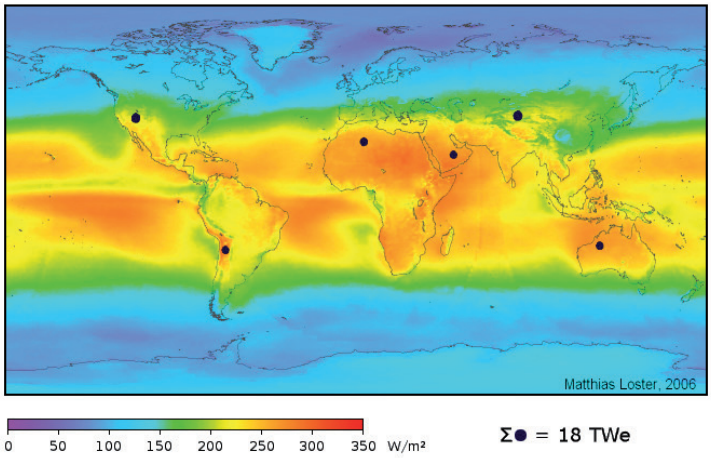

Figure 1.3: Map of average global insolation. The black dots represent possible locations of large solar power plants that in total could provide the world's total energy demand. (Source:http://www.ez2c.de/ml/solar_land_area/)

20 years ago, solar cells were still regarded as a niche market, and interesting only in off-grid and space applications areas where other sources of power either were unavailable or too expensive. Today, the situation is completely changed. Increased cell performance at reduced production and installation costs have cut down energy pay-back times for some solar modules to close to one year[10, 11]. With a further reduction in solar electricity prices, the technology will become cost-competitive in yet larger markets. In a recent roadmap on solar power from the International Energy Agency (IEA), PV is projected to provide 5 % of global electricity consumption in 2030, rising to 11% in 2050, corresponding to a installed capacity of more than 3 TWp[12][4]. Today, 80 % of the installed capacity of solar electric comes from crystalline silicon solar cells[13]. Despite being a poor optical absorber, silicon is by far the most commonly used base material for solar cells. The combination of abundance, availability, non-toxicity, and conve-

[4]Though this corresponds to a 250 times increased capacity compared to 2009 values, most of the solar industry and several environmental organizations find this estimate far too modest.

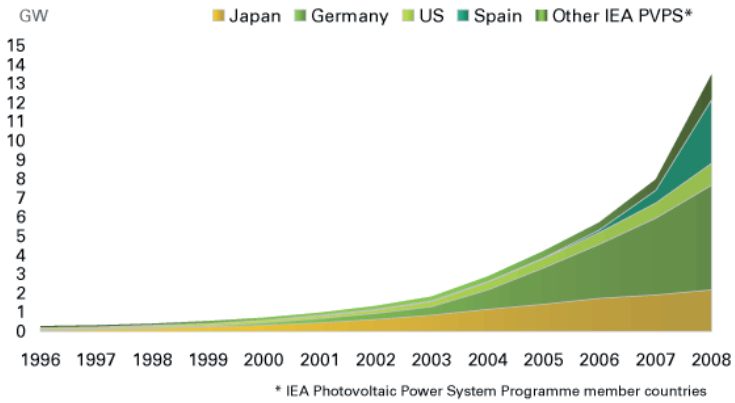

Figure 1.4: Total installed capacity of solar electricity from 1996 to 2008.(Source: BP statistical review of world energy 2009[1])

nient physical properties make silicon a natural choice of material for PV also in the future[14]. The relatively young PV industry also has benefitted greatly from the huge knowledge base of the microelectronic industry. Still, a necessary road ahead also for silicon solar cells is a further reduction in the price of solar electricity. This can be done either by cutting production and installation costs without hampering cell performance, or by increasing power output without increasing production and installation costs. Preferably both.

One very promising high-efficiency solar cell concept is the back-contact back-junction (BC-BJ) silicon solar cell[15, 16]. This type of cell design has already been proven to be compatible both with high efficiency and large-scale production[17]. In fact, it is the silicon solar cell concept that have demonstrated the highest efficiencies both on cell and module level in production[18]. Still, several issues need to be solved for BC-BJ silicon solar cells, both to increase the efficiency further towards the theoretical limit[19], and to reduce the production costs. In this thesis several important aspects related to BC-BJ silicon solar cells are addressed with the aim of both increasing efficiency and reducing costs. This is done through simulations, modeling, and laboratory experiments.

1.1 Thesis outline

Chapter 2 starts with a short introduction to silicon solar cells in general. Subsequently, back-contacted back-junction (BC-BJ) silicon solar cells are presented more in detail. Other types of back-contacted silicon solar cell designs are also briefly mentioned, and a short historic overview is given at the end of the chapter. Chapter 3 comprises the background and theory of the experiments performed during the work with this thesis. The most central equipment used for processing and characterization are presented. Plasma-enhanced chemical vapor deposition (PECVD) and laser technology have been especially central in the experimental work, and will be discussed somewhat more thoroughly. Also included in the chapter is a discussion of laser interaction with crystalline and amorphous silicon. In chapter 4 some experimental results that have not been included in any of the papers are presented. The main experimental results are given in papers II, III, and V, but some work of interest has not been published, and is therefore discussed herein. In general, experimental focus has been set on processes related to the backside of a BC-BJ silicon solar cell, and as will be explained in the next chapter, the front- and backside of a BC-BJ silicon solar cell can be optimized more or less independently. Complete solar cells have not been made during work with this thesis. On the other hand, it has been possible to investigate the influence from single processing steps on the performance of a finished solar cell through device simulations. A sketch of a possible process flow for a full BC-BJ silicon solar cell process is given at the end of chapter 4. In chapter 5 the background of the simulations performed with the ATLAS device simulator within the Silvaco simulation framework is presented. A conclusion is given in chapter 6.

Most of the work performed and described in this thesis and the appended papers was done by the author, but with some exceptions. Transmission electron microscopy (TEM) was performed by Annett Thøgersen, Institute for Energy Technology, Department of Solar Energy (IFE-Solar). Secondary ion mass spectroscopy (SIMS) was done by Alexander Azarov, Center for Materials Research, University of Oslo. Capacitance-voltage (C-V) measurements were performed by Edouard Monakov, IFE-Solar. Most of the simulation work was also done

by the author, but again with some exceptions. Ray tracing was performed by Jo Gjessing, IFE-Solar, while SPICE module simulations and ATHENA process simulations were done by Sean Erik Foss, also IFE-Solar.

Six papers are appended to this thesis, two of which are still under review in scientific journals. They all cover different and important issues regarding processing and simulations of BC-BJ silicon solar cells.

Paper I gives us valuable insight into the physics determining the performance of a BC-BJ silicon solar cell. From this insight important conclusions regarding the design rules of this type of solar cell devices can be drawn. The paper serves as a starting point for the simulation model, which has been gradually developed alongside with the experimental work during the whole Ph.D. process. Paper II deals with laser structuring of the backside of a BC-BJ silicon solar cell. Optimized laser and etching parameters are demonstrated to enable ablation (removal) of large areas of silicon from a silicon wafer without influencing the material quality in the processed regions, making it possible to produce self-aligned interdigitated finger patterns with flexible designs and dimensions. In paper III the same laser is utilized to ablate holes in a double-layer of passivating amorphous silicon (a-Si) and silicon oxide (SiO_2) without damaging the underlying crystalline silicon (c-Si). This is done with the aim of making local contacts on the back of a BC-BJ silicon solar cell. To further investigate the interaction between the laser and a-Si and c-Si, a thermodynamic model is developed that is able to predict the laser threshold fluence (energy density) for SiO_2 ablation as a function of the thickness of the a-Si layer. The model is presented in paper IV. In paper V the quality of aluminum contacts deposited through the laser ablated holes discussed in paper III is investigated. The quality of the contacts is first optimized experimentally, before the results are used to numerically optimize the design of a BC-BJ silicon solar cell by device simulations, and so to get an indication of the efficiency potential of the cell design we are working with. The last paper, VI, is dedicated to numerical investigation of potential quantum-mechanical tunneling of charge carriers in the junction between the adjacent, highly doped regions of opposite polarity on the back of a BC-BJ silicon solar cell. This is done through

both device, process, and circuit simulations.

1.2 List of publications

Paper I: K. Mangersnes and S. E. Foss. "Numerical optimization of a back-junction solar cell." Proceedings of the 22nd EUROPEAN PHOTOVOLTAIC SOLAR ENERGY CONFERENCE, pages 1701-1704, Milano 2007.

Paper II: K. Mangersnes and S. E. Foss, "Laser ablation of PECVD oxide for structuring of interdigitated silicon solar cells". Proceedings of the 24th EUROPEAN PHOTOVOLTAIC SOLAR ENERGY CONFERENCE, pages 2001-2003, Hamburg 2009.

Paper III: K. Mangersnes, S. E. Foss, and A. Thøgersen. "Damage free laser ablation of SiO_2 for local contact opening on silicon solar cells using an a-Si:H buffer layer." JOURNAL OF APPLIED PHYSICS, 107, 043528, 2010.

Paper IV: K. Mangersnes and S. E. Foss. "A thermodynamic model for the laser fluence ablation threshold of PECVD SiO_2 on thin a-Si:H films deposited on crystalline silicon." AMORPHOUS AND POLYCRYSTALLINE THIN-FILM SILICON SCIENCE AND TECHNOLOGY, (Mater. Res. Soc. Symp. Proc. Volume 1245, A16.02 , 2010).

Paper V: K. Mangersnes, S. E. Foss, and J. Gjessing. "Investigating the specific contact resistance on boron emitters in laser ablated holes in a passivating double-layer of a-Si:H and a-SiO_x:H." Submitted to Solar Energy Materials and Solar Cells, Oct 2010.

Paper VI: K. Mangersnes and S. E. Foss. "Tunneling in back-junction silicon solar cells." To be submitted to Solar Energy Materials and Solar Cells, 2010.

1.3 Filed patent applications

K. Mangersnes and S. E. Foss. "Buffer invention." U.S. provisional no. 12/838,695, filed 2010-07-19. German Gebrauchsmuster no. 202010011680.5, filed 2010-08-30.

K. Mangersnes and S. E. Foss. "Sputter Invention." U.S. provisional no. 61/407171, filed 2010-10-28.

Chapter 2

Back-contacted back-junction silicon solar cells

2.1 The basics of silicon solar cells

A solar cell is a device that converts sunlight directly into electricity through the photovoltaic effect[20]. The efficiency of the cell quantifies the fraction of solar energy that it converts into electrical energy. In principle it depends on two parameters. The generation of current by absorbed incident illumination and the loss of charge carriers via so-called recombination mechanisms. A built in p-n diode separates charge carriers of opposite polarity, and drives the light-generated current through the cell and to the terminals. Finally, several solar cells will be electrically connected and encapsulated as a module. In mathematical terms the efficiency, η, of a solar cell is given as;

$$\eta = \frac{P_{\text{out}}}{P_{\text{in}}} = \frac{FF \cdot J_{\text{SC}} \cdot V_{\text{OC}}}{P_{\text{sun}}}, \tag{2.1}$$

where P_{in} is the incoming power density and P_{out} is the maximum output power density of the cell. J_{SC} and V_{OC} are the short-circuit current density and the open-circuit voltage, respectively, while FF is the solar cell fill factor. FF describes the squareness of the current-voltage (J-V) curve. P_{sun} is the power density incident on the cell from the sun. Solar cell J-V characteristics are usually measured

under a set of standard test conditions where P_{sun} is 0.1 W/cm^2 of a normally incident air-mass (AM) 1.5 spectrum at 25 °C. A typical J-V curve of a high-efficiency silicon solar cell is shown in Figure 2.1. The J-V-curve of a solar cell

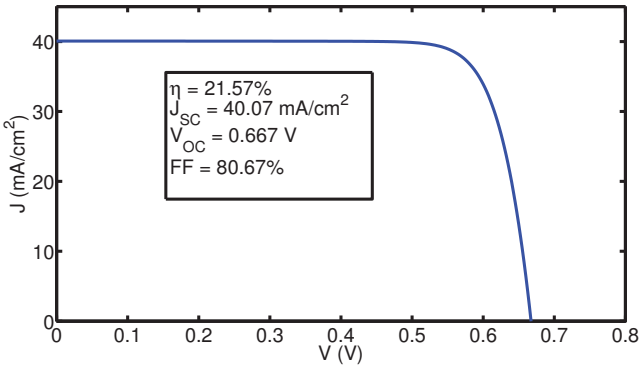

Figure 2.1: A typical current-voltage (J-V) curve of a high-efficiency solar cell.

is commonly shown in the first quadrant with the light-induced current density defined as positive and the dark current negative. The squareness of the curve is limited by the current's exponential dependence on voltage in a p-n diode. A one-diode equivalent circuit of a solar cell that also includes parasitic series and shunt resistances is shown in Figure 2.2. The corresponding J-V equation is given by

$$J(V) = J_{\text{SC}} - J_0 \exp\left[(V + JR_S)/V_{\text{th}}\right] - \frac{V + JR_{\text{S}}}{R_{SH}}, \tag{2.2}$$

where J_0 is the dark saturation current density, V is the applied voltage, V_{th} is the thermal voltage[1], R_{S} is the series resistance, and R_{SH} is the shunt resistance. R_{S} and R_{SH} should be as small and large as possible, respectively, in order to maximize the efficiency of a solar cell. Even if silicon is a natural choice as base material for solar cells, there are theoretical limitations to the possible maximum efficiency. In a single p-n junction device, low-energetic photons will pass through

[1]The thermal voltage is a proportionality factor that relates the electrostatic potential to the electrical current through a p-n diode. It is given as $V_{\text{th}} = \frac{kT}{q}$, where T is the absolute temperature and k and q are the Boltzmann constant and the magnitude of the electron charge, respectively.

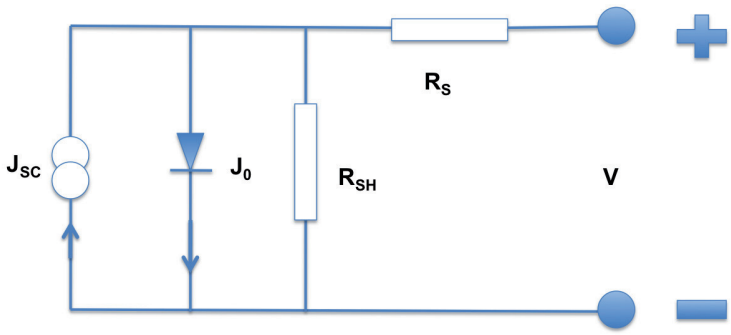

Figure 2.2: A one-diode equivalent circuit of a silicon solar cell, including parasitic series (R_S) and shunt (R_{SH}) resistances . J_{SC} and J_0 are the light-induced and dark current densities, respectively.

the cell without being absorbed. Higher-energetic photons will loose their excess energy, compared to the bandgap, as lattice heat. Energy is also lost across the p-n junction, at the contacts, and due to recombination. These loss mechanisms limit the maximum efficiency of a single-junction silicon solar cell to approximately 30 %, according to Shockley and Queisser[19]. The present world record efficiency is 25 % for a monocrystalline silicon solar cell[21, 22] and 20.4 %[2] for a multicrystalline cell[22, 24]. In production the efficiency of state of the art large area modules is typically 3-5 % lower than that of the record cells[17, 22, 25].

2.2 Back-contacted back-junction silicon solar cells

Back-contacted silicon solar cells comprise solar cells where the electrical busbars of both polarities are located on the backside[3]. In specific, back-contacted back-junction (BC-BJ) silicon solar cells, which is the main topic of this thesis,

[2]The cited articles from Zhao et al. and Schultz et al. report efficiencies of 24.7 % and 20.3 % for the mono- and multicrystalline silicon solar cells, respectively. More recently, the solar reference spectrum has been revised[23]. This entailed a 0.3 % absolute increase in efficiency for the monocrystalline cell and 0.1 % for the multicrystalline cell, leading to new world record efficiencies for silicon solar cells of 25 % and 20.4 %, respectively.

[3]An excellent review of back-contacted silicon solar cells was given by Kerschaver and Beaucarne[15].

have both the complete metallization and the complete contacted diffused regions located on the backside of the cell. It was originally designed with the emitter and back-surface field and the respective contacts forming an interdigitated finger pattern[16]. This interdigitated back-contact (IBC) structuring is still the most common way of aligning the structures on the backside of the cell, and the phrases IBC and BC-BJ are both commonly used to describe this cell design. Herein we will use the latter. A schematic drawing of a BC-BJ silicon solar cell is shown in Figure 2.3. This cell design entails numerous advantages compared to conven-

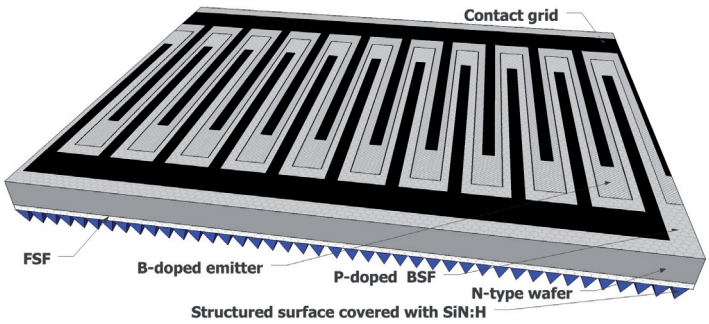

Figure 2.3: Schematic drawing of a back-contacted back-junction silicon solar cell. The cell is shown upside-down, and the dimensions are not to scale. FSF and BSF, are the front- and back-surface fields, respectively.

tional front-contacted silicon solar cells. Moving all contacts to the backside eliminates front-surface contact reflection. Thus, the conventional trade off between reflection and series resistance in the contact fingers is completely omitted. As a consequence, the sunward and rear side can be more or less independently optimized for optical and electrical performance, respectively. The low blue response commonly seen in front-contacted silicon solar cells, due to the high recombination in the front side emitter, is significantly improved. This justifies optical optimization for a broader set of wavelengths, and double-layer anti-reflection coatings are commonly used in combination with conventional alkaline surface texturing for reduced front-side reflection. BC-BJ silicon solar cells therefore

usually have a darker color appearance than conventional silicon solar cells. In combination with the clean, non-metallized front surface, this makes BC-BJ silicon solar cells especially attractive from an architectonic point of view, which is becoming more important with building-integrated photovoltaics. A BC-BJ solar module from Sunpower Corporation is shown in Figure 2.4. Moreover, having

Figure 2.4: A solar module from Sunpower Inc. The module is made from BC-BJ silicon solar cells, and holds the world-record efficiency for a commercially available silicon solar module. (Source:http://www.sunconnex.com/default.asp?page=SunPower-SPR)

contacts of both polarities on the same side may simplify cell interconnection in

modules, and allows for an increased packing density of cells[17, 26, 27].

On the processing side, however, there are some challenges. This is mostly related to the closely spaced interdigitated fingers of opposite polarity on the backside of the cell, see Figure 2.3. The processing therefore requires careful alignment of both diffused regions and contacts. Since photolithography is regarded unsuited for cost-effective large-scale production of silicon solar cells, low-cost alternatives, such as screen-printing, are commonly used for one or several alignment steps in BC-BJ research and production[17, 28]. This limits the minimum pitch to the order of mm. This is in contrast to the cells produced in the early stages of BC-BJ silicon solar cell research and production. With the use of photolithography a pitch in the order of 50 μm was easily obtained. This might still be possible to justify for concentrator applications, but for one-sun flat solar panels, photolithography is too expensive as a patterning tool to make the cells cost competitive. Another process-related challenge is the silicon material quality. Since the emitter is located on the backside of the cell, and the charge carriers are generated predominantly near the front surface, the carriers have to diffuse through the whole thickness of the wafer. With a pitch in the order of mm the average required diffusion distance of minority carriers is even more lateral than vertical. The required maximum diffusion length, $L_{\max}$, therefore depends on the wafer thickness, W, and the width of the back-surface field, d_{BSF}, see Figure 2.5. $L_{\max}$ can be calculated as

$$L_{\max} = \sqrt{\frac{1}{4} d_{\mathrm{BSF}}^2 + W^2}. \tag{2.3}$$

With a wafer thickness of 200 μm and a BSF width of 600 μm this results in a maximum diffusion length of approximately 360 μm. This is indeed a two-dimensional problem, and device simulations should at least be in two dimensions. The need of long diffusion lengths call for high-quality monocrystalline wafers with long minority carrier lifetimes and excellent surface passivation. The minority carrier lifetime also needs to remain high through the whole process and under illumination. This can be a challenge, but the use of n-type (instead of p-type) wafers has been shown to facilitate the challenges related to process and light-induced degradation of the silicon material, see section 2.4.

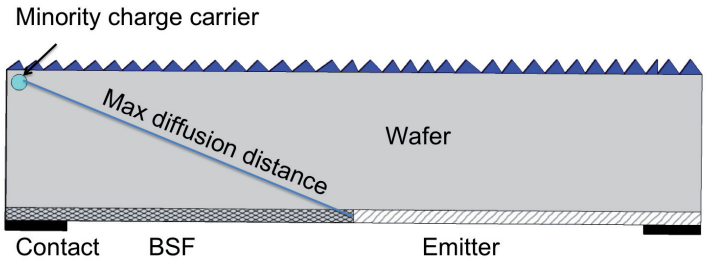

Figure 2.5: Schematic, simplified, side-view drawing of the smallest repeating unit of a back-contacted back-junction silicon solar cell. The diagonal line shows the maximum required diffusion length for minority charge carriers. BSF is the back-surface field. The drawing is not to scale.

2.2.1 The emitter-wrap-through cell design

The emitter-wrap-through (EWT) solar cell concept is quite similar to the BC-BJ solar cell design[29]. The complete metallization is still located on the back of the cell, but a part of the collecting emitter is now close to the front surface. This lowers the requirements for high minority carrier lifetime materials compared to BC-BJ cells, as the average diffusion length is significantly reduced. The extension to the backside contacted junction is done through laser drilled vias in the wafer. On a 5 inch square wafer, between 10000 and 20000 holes are typically used as transporting channels for minority carriers collected at the front or through the complete thickness of the silicon wafer. The EWT cell concept includes almost all the advantages of a BC-BJ silicon solar cell, but with reduced requirements for material quality. A scanning-electron microscope (SEM) picture of some of the vias of an EWT silicon solar cell is shown in Figure 2.6.

2.2.2 The metallization-wrap-through cell design

The metallization-wrap-thorugh (MWT) solar cell is the back-contact solar cell concept that most resembles the conventional front-contacted solar cell[30]. A

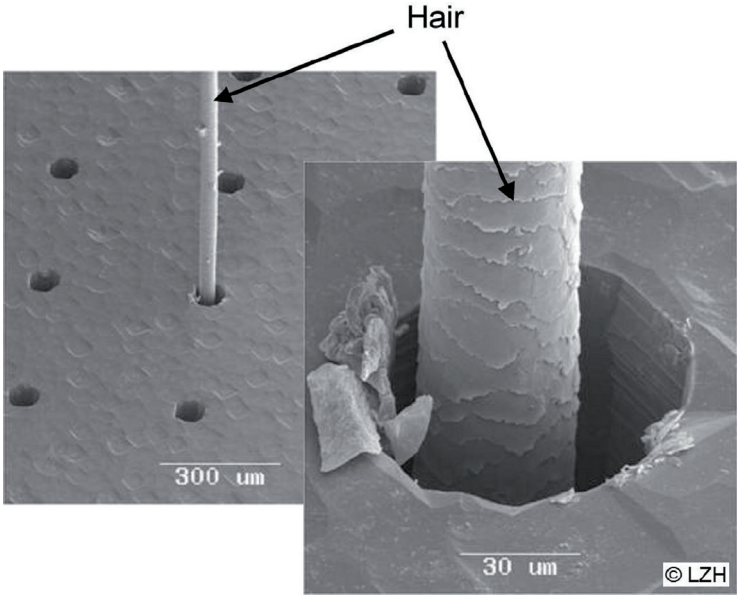

Figure 2.6: The laser-drilled vias of an emitter-wrap-through (EWT) silicon solar cell, shown together with a human hair for comparison of the dimensions. The picture is taken from an article by Aart Schoonderbeek and Andreas Ostendorf found on the technical news website "SPIE Newsroom", and printed with permission from Laser Zentrum Hannover (LZH).
(Source: "http://spie.org/x25041.xml?ArticleID=x25041").

schematic drawing of a MWT cell is shown in Figure 2.7. In this cell design the emitter and contact fingers are located at the front surface, but the busbars for interconnection are still at the rear side. The extension from the front side metal fingers to the busbars is done via laser drilled holes in the wafer. The holes are filled with metal through a standard metallization process, usually screen-printing. This facilitates the transition from a conventional cell process. As for EWT cells, the MWT solar cell design does not have the same requirement for long carrier lifetimes material as BC-BJ cells, and can therefore be produced on conventional multicrystalline silicon wafers. At the same time, the reflection losses are reduced, and module assembly is still simplified compared to conventional front-contacted

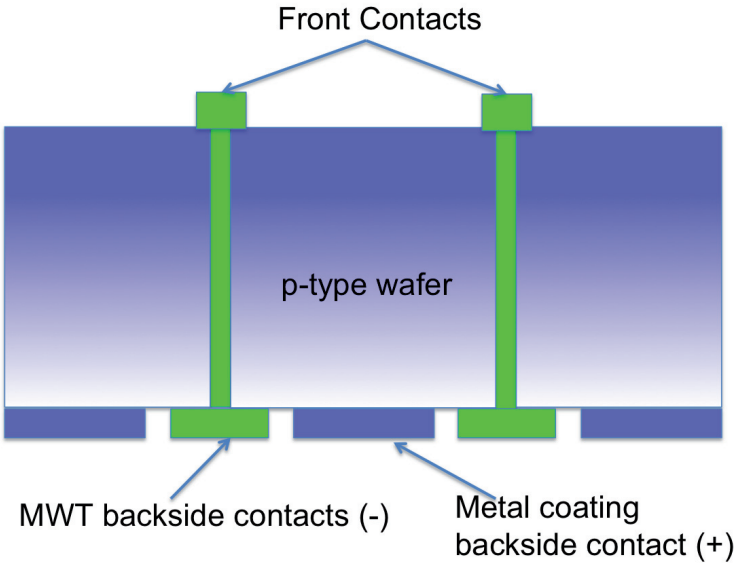

Figure 2.7: Simplified, schematic drawing of a (p-type) metallization-wrap-through (MWT) silicon solar cell. The drawing is not to scale.

silicon solar cells.

2.3 Short historic overview of the BC-BJ solar cell

The BC-BJ silicon solar cell concept was first suggested by Schwartz and Lammert more than 30 years ago[16, 31]. It was originally envisioned as a cell design for concentrator applications. With the first version Schwartz reported an efficiency of 17% under 50 suns concentration. The emitter and base diffusions, and the respective contacts where arranged in an interdigitated finger pattern on the backside, see Figure 2.3. Other geometrical arrangements of the diffusions and contacts have been demonstrated as well. The most famous is the point contact cell of Swanson et al.[32] from 1984, where the backside diffusions are arranged in arrays of single points. An improved version of this cell was later demonstrated to give an efficiency of 28.4 % under 200 suns concentration[33]. The align-

ment of the backside diffusions, contact openings, and contacts were done by photolithography in early stages of BC-BJ silicon solar cell development. Four to six photolithography steps were used to produce the cells[34]. Photolithography is not compatible with cost-efficient production of solar cells, and thus the interest in the BC-BJ solar cell concept was mainly for niche and academic reasons[35]. The main contributions in the field of BC-BJ solar cells during the 1980's and 1990's came from Professor Swanson's photovoltaic group at Stanford University. R. A. Sinton (also from the Stanford group) simplified the processing of BC-BJ solar cells by introducing processes for self-aligned diffusions and contact separation[34, 36]. This was a necessary step towards cost-effective BC-BJ silicon solar cells. Professor Swanson commercialized his technological ideas through the Sunpower Corporation, which he started up in 1985. Today, Sunpower is the world leading manufacturer of BC-BJ silicon solar cells, with a total production capacity of 625 MWp. In 2002, the company introduced their A-300 cell concept for one-sun solar module applications[37]. The cell is produced without any photolithography steps, and only uses low-cost manufacturing process steps. In the first round this led to an efficiency decrease compared to previous cells processed with photolithography, but the A-300 cell design has later been improved to demonstrate world-record efficiencies for BC-BJ silicon solar cells under one-sun illumination. Recently, the R&D unit at Sunpower has reported a full cell area efficiency of 24.2 % for the A-300 solar cell, and a large area efficiency of 20.4 % for the A-300 solar module[18], see Figure 2.4. These are the world records for a large area silicon solar cell and for a commercially available silicon solar module, respectively[22].

Other groups and companies are working with BC-BJ silicon solar cells as well. One very elegant cell concept that deserves to be mentioned is the RISE (Rear Interdigitated Single Evaporation) silicon solar cell from Institut für Solarenergieforschung Hameln (ISFH), developed by Engelhart et al.[38]. The RISE solar cell has been developed both as a BC-BJ silicon solar cell and as an EWT cell, see subsection 2.2.1. The cell design utilizes laser as the central processing equipment, both as a pattering tool and for local contact opening through a passivating backside layer of

thermal SiO_2[39, 40][4]. In addition, the cell concept implements some of the ideas of Sinton et al. from the late 1980's and early 1990's regarding self-alignment and contact separation[34, 36]. 22 % efficiency has been demonstrated on a 4 cm^2 p-type FZ wafer[41][5]. The RISE silicon solar cell is presently being tested in pilot lines, and is expected to enter the commercial market within the coming years. More thorough historic overviews of BC-BJ silicon solar cells can be found in the review article by Kerschaver and Beaucarne[15] and in the thesis of F. Granek [42].

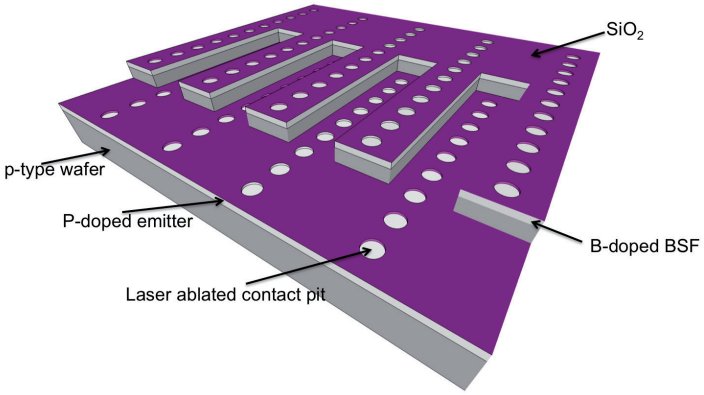

Figure 2.8: Schematic, simplified, rear-view drawing of the RISE silicon solar cell developed at Institut für Solarenergieforschung Hameln (ISFH). The boron-doped back-surface field (BSF) is at an elevated level compared to phosphorus-doped emitter. The cell is shown before contacting and is not to scale.

2.4 n-type vs. p-type wafers

The standard in the solar cell industry has been p-type wafers with n-type diffused emitters. In theory, electrons have a higher mobility than holes, and for equal carrier lifetimes p-type wafers will therefore outperform n-type wafers due to the longer diffusion length of electrons as minority carriers. The world record 25 %

[4] In the RISE-EWT solar cell, a laser is also used to drill the vias/holes in the wafer.
[5] Harder et al. have demonstrated an efficiency above 21 % also for the RISE-EWT solar cell.

efficient silicon solar cell was made on p-type FZ high-purity silicon material[21]. These cells are processed in very clean facilities. In large-scale production, however, it is more or less impossible not to induce chemical and mechanical imperfections to the wafers. And herein lies the big advantage of n-type silicon solar cells. The performance of n-type cells has been shown to be less hampered by chemical and mechanical impurities. In fact, n-type silicon solar cells hold numerous advantages compared to p-type cells.

- n-type cells are not prone to light-induced degradation due to splitting of boron-oxygen complexes[43, 44].
- n-type cells are less sensitive to chemical impurities activated during high-temperature diffusion and oxidation steps[45, 46].
- n-type cells are less sensitive to laser-induced damage[44, 47].

Sunpower and Sanyo, the two companies that have reported the highest efficiencies of silicon solar cells in large-scale production both use n-type monocrystalline wafers as a base material in their A-300 and HIT solar cells, respectively[17, 48].

Chapter 3

Experimental Background

This chapter gives a general overview and a short theoretical background of the methods, materials, and equipment most frequently used during the work with this thesis.

3.1 Wafers, cleaning, and etching

3.1.1 Wafers and cleaning

We have used 4-inch, n-type, Cz, 1-3 Ω·cm double-side polished wafers from Siltronix in all major experiments. The wafers have a thickness of 300 μm. p-type wafers from the same manufacturer were in some cases added to monitor the sheet resistance of phosphorus emitters. Prior to all experiments the wafers were cleaned in 5 % HF, Piranha (4:1, H_2SO_4: H_2O_2), and HCl[49].

3.1.2 Alkaline etching

After laser ablation of SiO_2 (see paper II), we used KOH to etch away the thermally induced damage from the laser and to reestablish a clean and smooth silicon surface. Alkaline etching of silicon and its passivating layers was extensively investigated by Seidel et al., both for undoped and doped silicon[50, 51]. In sum-

mary, they suggest the following reaction for alkaline etching of Si;

$$\mathrm{Si} + 2\mathrm{OH}^- + 2\mathrm{H_2O} \rightarrow \mathrm{SiO_2(OH)_2^{--}} + 2\mathrm{H_2}, \tag{3.1}$$

and

$$\mathrm{SiO_2} + 2\mathrm{OH}^- \rightarrow \mathrm{SiO_2(OH)_2^{--}} \tag{3.2}$$

for etching of SiO_2, indicating that the alkali atoms have no effective role in the etching process. The oxide we have used during the work with this thesis is deposited at low temperature with PECVD (see section 3.2). The PECVD oxide structure is less dense than a thermal oxide, and it typically contains 1 to 10 atomic % of hydrogen[52]. The etch rate in KOH therefore differs from that reported by Seidel et al. for thermal oxides. In general, the low temperature SiO_2 does not withstand alkaline etching as well as a thermal oxide, but the etch rate is still significantly lower than for silicon. To be able to keep a stable and controlled temperature in the aqueous KOH solution, the KOH-containing beaker was put into a larger beaker filled with water and indirectly heated by a heating plate, see Figure 3.1. Noor et al. investigated the resulting surface roughness on n-type <100> silicon wafers after etching in aqueous KOH solutions of varying concentrations and temperatures[53], see Figure 3.2 [1]. In addition to optimizing for surface smoothness after laser ablation, the etch rate of silicon is also important to keep in mind for reduced processing times. We found, in agreement with Noor et al., that a KOH concentration of 55 % (weight) gave the smoothest surfaces for temperatures of 65 °C and 80 °C. The etch rate of silicon in alkaline solutions is decreasing with increasing alkaline concentrations above 20 % (weight)[50]. At the same time, the etch rate increases with temperature. All considerations taken into account, a 55 % (weight) KOH concentration at 80 °C gave the best results. With these etching parameters the etch rate of <100> silicon is about 0.6 μm per minute[50], while the measured etch rate of PECVD SiO_2 was found to be approximately 10 nm per minute.

[1] Noor et al. do not explain how the surface roughness is measured, and we therefore assume that the roughness is the arithmetic average, R_a, from the surface mean, which is the most common way of defining it.

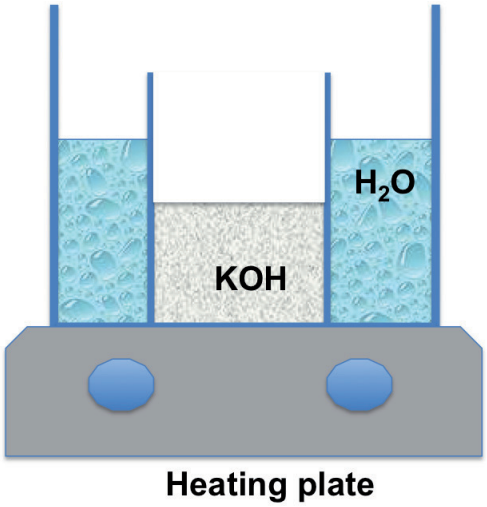

Figure 3.1: The setup used to keep a stable temperature in the aqueous KOH etching solution.

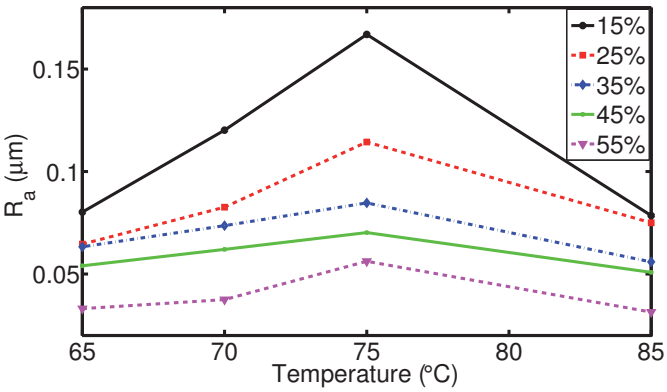

Figure 3.2: The resulting surface roughness as a function of temperature on <100> n-type silicon after etching in aqueous KOH solutions of varying temperatures and concentrations (weight %). The data points are from Noor et al.[53].

3.2 PECVD

Plasma-enhanced chemical vapor deposition (PECVD) is a technique commonly used to deposit thin films from vapor phase to solid state on substrates. It is a subset of general chemical vapor deposition techniques that is aided by a plasma (normally) created by a radio-frequency discharge between two electrodes. The deposition is a result of chemical reactions in or between one or several precursor gasses in the plasma and the substrate. The volatile byproducts are removed by the gas flow through the reactor chamber. A Plasmalab 133 parallel plate system from Oxford Instruments[54] was used during the work with this thesis, see Figure 3.3. The substrate is placed on the lower electrode, which is heated. The combination of different precursor gases, deposition time, temperature, pressure, power density, and flow of the different gases make it possible to deposit a wide range of thin films. Each type of film can be optimized for its purpose by altering the deposition parameters and by finding the optimum ratio between the flow of different precursor gases. In this work the Oxford Instruments PECVD system has been used to deposit hydrogenated amorphous silicon (a-Si:H, a-Si for simplicity) and hydrogenated amorphous silicon oxide (a-SiO_x:H, SiO_2 for simplicity).

3.2.1 Hydrogenated amorphous silicon

Crystalline silicon (c-Si) has a diamond like structure based on covalent sp^3 bonding. The convenient electrical and optical properties of c-Si, in combination with its abundance, have made it the most commonly used material in the semiconductor industry. Amorphous silicon, on the other hand, is a disordered form of silicon, and the physical properties differ significantly from that of c-Si. In contrast to c-Si, a-Si has a direct optical bandgap of approximately 1.7 eV[55]. It is, thus, a strong optical absorber in the visible part of the spectrum. The disordered atomic structure also implies that a-Si has a low thermal conductivity. The conductivity depends on the hydrogen content, but is in the order of 0.01 W/cm·K[56, 57]. This is more than two orders of magnitude lower than that of c-Si, see Figure 3.10.

In addition, there has been shown to be an additional thermal resistance at the

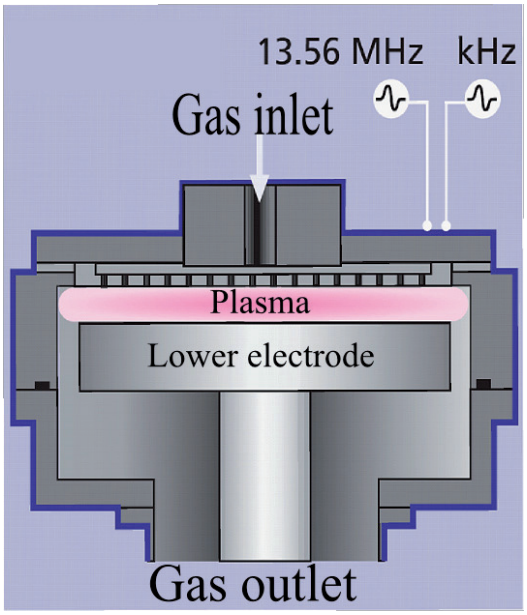

Figure 3.3: Schematic overview of a parallell-plate plasma-enhanced chemical vapor deposition (PECVD) system. (Source: "http://www.oxford-instruments.com")

interface between thin film a-Si and bulk c-Si. This was investigated and quantified by Kuo et al. [58] and Volz et al.[59], and will be discussed more thoroughly in sections 3.3.1 and 3.3.2.

Locally, a-Si resembles its crystalline counterpart, but there is no long range order. The atomic structure of a-Si:H as obtained from density functional theory (DFT) calculations is shown in Figure 3.4. Each Si atom is in general bounded to four neighbors at tetrahedral angles ($\theta = 109°$) and a bond length of 0.35 nm. A spread in bond angle of about 10 % and a spread in bond length of approximately 2 % cause the disordering. a-Si also contains a large portion of dangling (unsatisfied) bonds. The density of these imperfections is typically in the order of 10^{15} to 10^{16} cm^{-3}. When prepared by PECVD, a-Si contains in the order of 10 atomic % of hydrogen[64]. Hydrogen is known to passivate dangling bonds, and thereby lower

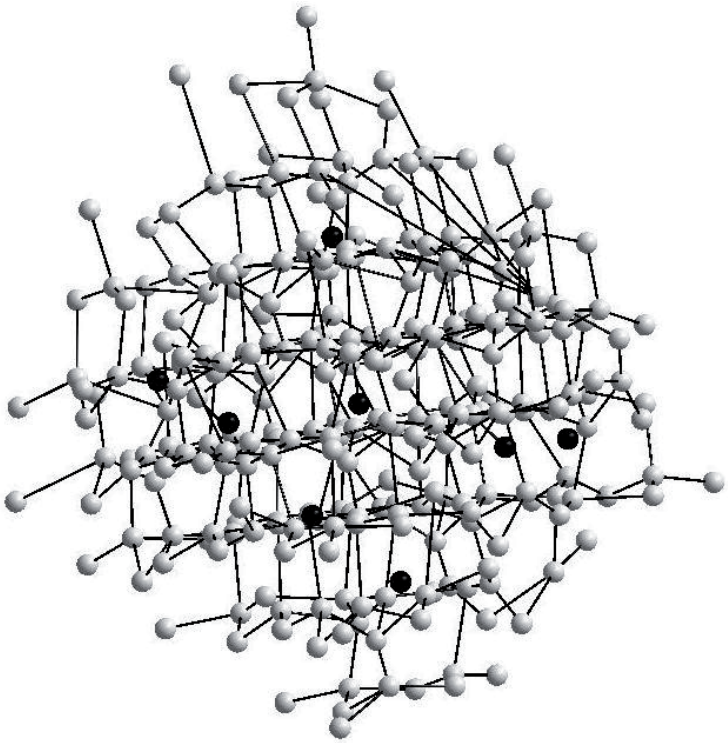

Figure 3.4: The atomic disordered structure of a-Si:H as obtained by density functional theory (DFT) calculations with the Vienna Ab-Inito Simulation Package (VASP)[60, 61, 62, 63]. The grey and black balls represent silicon and hydrogen atoms, respectively. The hydrogen is found both interstitially and bonded to silicon dangling bonds. The simulations are performed by Smagul Karazhanov at the Department of Solar Energy, IFE.

the impact of the defects in the amorphous structure.

For deposition we used undiluted silane (SiH_4) as the only precursor gas in the PECVD chamber[65]. The deposition temperature and pressure were 230 °C and 300 mTorr, respectively. When a-Si was used as a surface passivation layer, a very low RF input power density of 0.008 W/cm^2 was used during deposition to avoid

surface damage as a consequence of ion bombardment. A slightly higher power density was used to ignite the plasma during the first few seconds of the deposition. With this power density we measured the deposition rate to be approximately 5 nm per minute. The overall reaction that must occur is

$$\mathrm{SiH_4(g)} \rightarrow \mathrm{Si(s)} + 2\mathrm{H_2(g)}, \tag{3.3}$$

where s and g denote solid and gas phase, respectively. In general, the reaction is usually more complicated. The oscillating electric field causes the unstable silane to dissociate, producing a mixture of ions, electrons, and radicals; a plasma. The dominant precursor to a-Si:H is the SiH_3 radical. This radical, which is short of one hydrogen atom, and so has a reactive dangling bond, is transported to the substrate by the gas flow. When SiH_3 attaches to the surface where there is a dangling bond, this will lead to film growth[66].

The implementation of hydrogenated amorphous silicon to the solar cell and thin film transistor (TFT) technology has been challenged by the well described metastability of the material. Both light and applied bias induce chemical changes in a-Si[66];

$$\mathrm{SiHHSi} + \mathrm{Si\text{–}Si} \Leftrightarrow 2\mathrm{SiHDSi}, \tag{3.4}$$

where Si–Si represents a weak bond, and D represents a dangling bond. For TFTs, the increased number of dangling bonds, i.e., bandgap states, leads to a shift in the threshold voltage[66], while for a-Si solar cells it induces a degradation of the photocurrent[67]. The latter is known as the Staebler-Wronski effect[68, 69]. The induced changes have been shown to be reversible upon annealing. Since the light-induced carriers break Si-H bonds, it also degrades the surface passivation quality of a-Si films on Si. For backside passivation, however, this is less of an issue since the charge carrier generation in the a-Si layer is very low. The passivation quality of backside a-Si has been reported to be long-term stable[70, 71].

In contrast to e.g. PECVD SiN_x, the passivation mechanisms in a-Si on Si are purely chemical[70, 72]. The passivation originates from termination of dangling bonds at the interface and not by an electric field induced by surface charge. This

is important in BC-BJ silicon solar cells to avoid channel tunneling near the back-surface[73]. A capacitance-voltage (C-V) plot of an a-Si film, deposited with the same Oxford Plasmalab system discussed earlier in this section, on a c-Si substrate is shown in Figure 3.5. The clean exponential form of the curves indicates that there is no surface charge between the materials, and that we have a (near) perfect surface between the amorphous film and the crystalline bulk. Finally, a-Si has been shown to be excellent for passivation of c-Si surfaces, either solely or in a stack with a PECVD dielectric[64, 70, 71, 74, 75, 76].

We have used the qualities of a-Si for several purposes during the work in this thesis. In paper II a thin layer of a-Si was deposited on both sides of each sample for surface passivation, i.e. to terminate the dangling bonds at the c-Si wafer surface. This was done after laser processing, etching, and cleaning and prior to

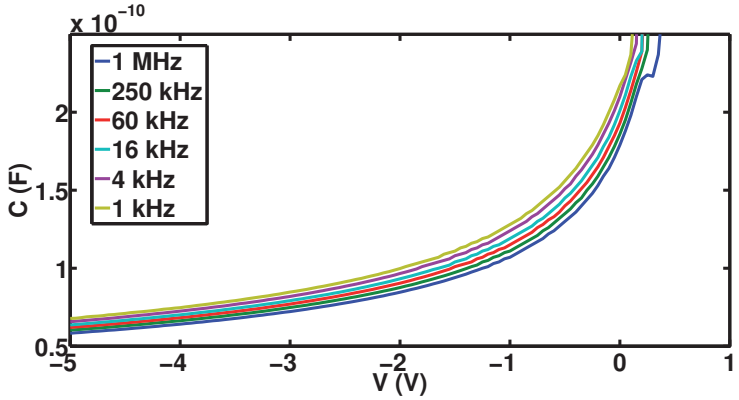

Figure 3.5: Capacitance-voltage (C-V) plot of a thin film of a-Si on n-type bulk c-Si at different AC frequencies.

lifetime measurements. Surface passivation is done to, as far as possible, exclude surface recombination from the effective recombination lifetime measurements, see section 3.5. In paper III other aspects of the a-Si film is exploited. We took advantage of the high optical absorption and low thermal conductivity of the material. a-Si is utilized to absorb laser irradiation and to locally remove a covering

transparent layer of PECVD SiO_2 for point contact formation. The high optical absorption and low thermal conductivity of a-Si, aided by the interface resistance to c-Si, induce a high energy density in the a-Si film after laser irradiation. This leads to an indirect ablation of SiO_2 at laser fluences (energy densities) five times lower than that needed to ablate SiO_2 on c-Si. The residual SiO_2– a-Si double-layer has been shown to be excellent for surface passivation for the back of a silicon solar cell[70, 71]. With the modeling work in paper IV we aimed to get a better theoretical understanding of the physics involved in laser ablation of SiO_2 with and without the buffer layer of a-Si. Both a static and a dynamic model were developed, and both were in good agreement with the experimental data, see sections 3.3.1 and 3.3.2. In paper V we investigated the contact resistance for contacting through the same passivating double-layer of a-Si and SiO_2.

3.2.2 Hydrogenated amorphous silicon oxide

SiO_2 (a-SiO_x:H) was deposited with the Oxford Instruments Plasmalab PECVD system described above. To get deposition we must have;

$$\mathrm{SiH_4(g) + 2O \rightarrow SiO_2(s) + 2H_2}. \tag{3.5}$$

O_2 can be used, but since oxygen is reactive with silane independent of the plasma, considerable nucleation will take place uniformly in the whole PECVD system, not only on the sample. Thus, other oxygen sources are usually preferred. CO_2 is also a likely source of oxygen, but carbon incorporation can have a deleterious effect on device performance. N_2O is therefore usually preferred in PECVD oxide deposition processes. The probable chemical route is

$$\mathrm{3SiH_4 + 6N_2O \rightarrow 3SiO_2 + 4NH_3 + 4N_2}. \tag{3.6}$$

We used a flow of 1000, 800, and 17 sccm of N_2O, N_2, and SiH_4, respectively. The temperature, pressure, and RF input power density were 300 °C, 500 mTorr, and 0.06 W/cm^2, respectively. The flow of N_2 improves the homogeneity of the oxide film as it dilutes the other precursor gasses, but it does not take part in the chemical reactions. We found the deposition rate to be approximately 45 nm per minute.

Since the PECVD oxide is deposited at low temperature, and not thermally grown, it has an amorphous structure. The atomic structure of a-SiO_2 as obtained from DFT calculations is shown in Figure 3.6. It is less dense than a thermal oxide, and PECVD SiO_2 typically has a hydrogen content of 1-10 atomic %[52]. It has been used for several purposes during the work with this thesis.

- It has been used as a diffusion barrier against liquid dopant-containing spray-on sources, and against gaseous BBr_3 and $POCl_3$ in our tube furnace. The SiO_2 has a finite resistance against dopants, and a thick layer was needed to get sufficient resistance against the dopants for typical diffusion processes, see section 4.1.

- The oxide was used as an etching barrier against aqueous KOH solutions. KOH was used to clean up the induced damage after laser ablation of large areas (see paper II). In contrast to a-SiN_x, amorphous silicon oxide has a finite etch rate in KOH. This etch rate, which depends on the KOH concentration and temperature, needs to be taken into account under device fabrication. It is important because a certain thickness of the oxide film is needed to make it work successfully as a diffusion barrier. In addition, laser parameters used for structuring (see paper II) and contact opening (see paper III and V) are sensitive to the thickness of the oxide layer due to interference effects, see Figure 3.7. The etch rate of PECVD SiO_2 in an aqueous KOH solution of 55 % (weight) at 80 °C was found to be less than 10 nm per minute.

- The oxide served as an anti-reflection coating for the green laser light during indirect ablation of oxide, see section 3.3. An optimized thickness of the oxide layer lowers the energy threshold for ablation. This is done by tailoring the thickness of the SiO_2 into a reddish color, which implies that it will have low reflection in the green part of the spectrum, see Figure 3.7.

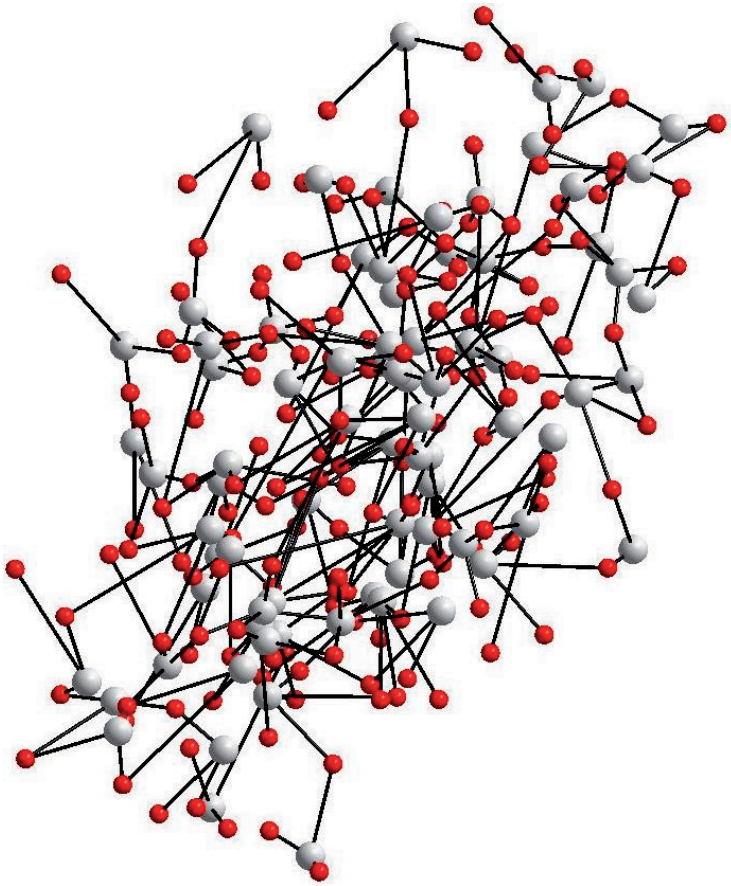

Figure 3.6: Atomic structure of a-SiO_2 as obtained by density functional theory (DFT) calculations with the Vienna Ab-Inito Simulation Package (VASP)[60, 61, 62, 63]. The grey and red (dark in greyscale print) balls represent silicon and oxygen atoms, respectively. The simulations were performed by Smagul Karazhanov at the Department of Solar Energy, IFE.

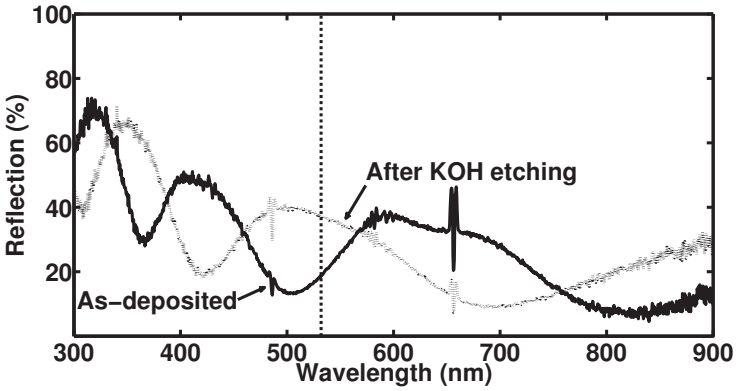

Figure 3.7: Reflectance measurements of a 450 nm thick SiO_2 film on c-Si bulk. The reflection increases from 18 % as-deposited and near optimized (solid black line) to 37 % after immersing the sample to an aqueous KOH etching bath (grey dotted line) for a wavelength of 532 nm (indicated by the vertical dotted line), corresponding to that of the green laser used in these experiments.

3.3 Laser

The laser we have used during the work with this thesis is a diode pumped, frequency doubled (532 nm), Nd:YVO_4 RSM 20E from Rofin-Sinar. The system is Q-switched, and the pulse duration varies between 30 and 350 nanoseconds depending on the diode current and the repetition frequency. In focus the $\frac{1}{e^2}$ spot diameter is 40 μm. The laser beam charcteristics were measured by a BC106-VIS CCD camera beam profiler from Thorlabs. With this laser system we have the possibility of varying the diode current from 12 A to 40 A, the pulse repetition frequency from 10 kHz to 100 kHz, in addition to changing the focal plane. The other laser parameters, such as pulse duration and energy, vary internally with the diode current and pulse frequency. The measured fluence as a function of diode current at 20 kHz repetition frequency is shown in Figure 3.8. The two different curves in the figure represent measurements of the laser fluence with six months time difference with the same parameter settings. The difference was found to result from a degradation of the laser diode power. We measured the fluence with an Ophir Laserstar power meter and a BFi-OPTiLAS pyrolectric sensor.

The laser has been a central processing tool during the work with all the experimental papers (II, III, and V). We have used the same laser to structure large areas for patterning of the backside of BC-BJ silicon solar cells (see paper II), and to make local contact openings through a stack of PECVD a-Si and SiO_2. The latter was investigated in papers III, IV, and V. First through the influence on the local surface recombination velocity (see subsection 3.5.1), then by modeling (see subsections 3.3.1 and 3.3.2), and finally by investigating the contact resistance by using the transfer length method (see section 3.7).

3.3.1 Laser interaction with crystalline and amorphous silicon

In both crystalline and amorphous silicon, laser energy is absorbed by excitation of charge carriers across the bandgap. The optical (linear) absorption coefficient, α, is given as

$$\alpha = \frac{4\pi k}{\lambda}, \tag{3.7}$$

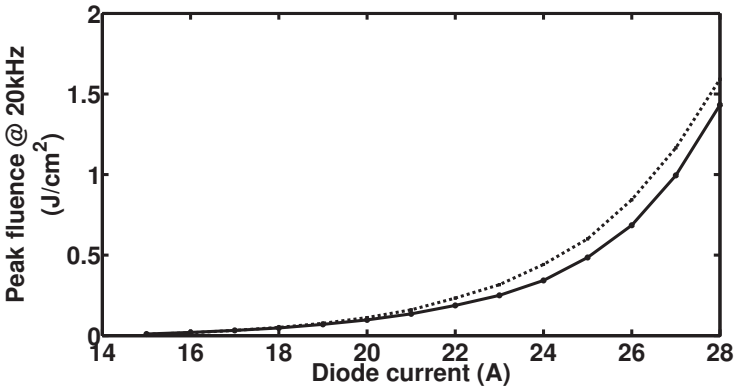

Figure 3.8: Single pulse peak fluence as a function of diode current for our Nd:YVO_4 green laser. The two different curves represent measurements of laser fluence with six months time difference with the same parameter settings.

where λ denotes the wavelength, and k the imaginary part of the complex refractive index, $\tilde{n} = n - ik$. The optical intensity at a depth x in the material can be calculated by the Bouger-Beer-Lambert law[2] through[77]

$$\frac{dI(x)}{dx} = -\alpha x. \tag{3.8}$$

A possible solution to this equation for an incident optical intensity I_0 at a sample with surface reflection R is

$$I = I_0(1 - R)e^{-\alpha x}, \tag{3.9}$$

if we assume that the attenuation of the optical intensity is solely caused by absorption. The $\frac{1}{\mathrm{e}}$ optical absorption depth is then simply given by $\frac{1}{\alpha}$, and often denoted l_α. In the most general case, α is temperature dependent. The temperature dependent optical absorption coefficient of silicon, $\alpha(T)$, at $\lambda = 532$ nm has

[2]The law is also frequently called the Lambert-Beer law or simply Beer's law. It was first derived experimentally by P. Bouger in 1729 and then theoretically by I. G. Lambert in 1760. A mesoscopic interpretation of α was first given by A. Beer in 1952.

been measured and parameterized by Jellison et al.[78];

$$\alpha(T) = 5.02 \times 10^3 \mathrm{e}^{T/430}, \tag{3.10}$$

for 300 K $< T < 1000$ K, see Figure 3.9. The referenced temperature range is marked with a double arrow in the figure. In the simulations we have continued this exponential increase also in the range 1000 K to 1685 K, where the latter corresponds to the melting temperature of c-Si. At the transition temperature an abrupt change in the absorption coefficient is marked in the figure (3.9)[79]. For liquid silicon ($T >$ 1685 K), an absorption coefficient of 1×10^6 cm^{-1} (still for $\lambda = 532$ nm) was measured by Rezek et al.[79]. For a-Si, we do not have data other than for at 300 and 1420 K, marked with circles in the figure. We know, however, that the absorption coefficient of a-Si has been found to increase linearly with temperature at other wavelengths[80], and we assume this to be valid also at 532 nm.

The first interaction between laser and material is always purely optical, but when the duration of the laser pulse exceeds the duration of the thermal relaxation mechanisms in the material (in the order of 10^{-11} s in silicon), heat will start to dissipate into the material. The absorbed laser energy is transferred via electron-electron, electron-phonon, and phonon-phonon interactions. The thermal diffusion length, l_{th}, is often approximated by

$$l_{\mathrm{th}} \approx \sqrt{2D\tau_p}, \tag{3.11}$$

where D is the thermal diffusivity and τ_p is the laser dwell time. The thermal diffusivity quantifies a material's ability to adjust its temperature according to the surroundings. It is given as the ratio between the thermal conductivity, κ, and the volumetric heat capacity, $C_p = \rho c_p$, with ρ being the mass density and c_p the specific heat capacity;

$$D = \frac{\kappa}{\rho c_p}. \tag{3.12}$$

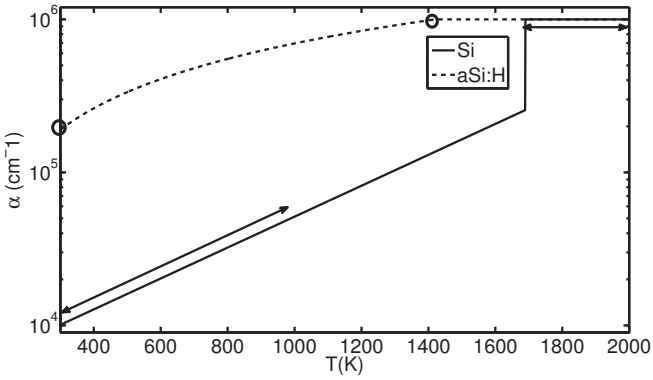

Figure 3.9: The absorption coefficients of crystalline and amorphous silicon at a wavelength of 532 nm. The referenced temperature range is marked with a double arrow on the c-Si curve. For the a-Si curve the only two referenced temperatures are marked with circles.

l_{th} describes the $\frac{1}{e^{1/2}}$ spatial decay[3] in the temperature distribution

$$T(x,t) \approx \frac{Q}{\rho c_p \sqrt{4\pi D t}} \mathrm{e}^{\frac{-(x)^2}{4Dt}}. \tag{3.13}$$

This is a fundamental solution of the one-dimensional linear heat equation for a point source in infinite space;

$$\frac{\partial T}{\partial t} = D\frac{\partial^2}{\partial x^2}T + \frac{Q}{\rho c_p}\delta(x,t), \tag{3.14}$$

where Q is the total energy release, and δ the Dirac delta function.

In general, l_{th} depends on the particular boundary problem under consideration, and may differ from Equation (3.11). Both the thermal conductivity, the heat capacity, and the density of mass are usually temperature dependent. In addition, the laser source has a finite distribution in space and time. This leads to a more

[3]The $\frac{1}{e}$ spatial decay in the temperature is also often used to describe l_{th}, which then can be approximated as $2\sqrt{D\tau_p}$.

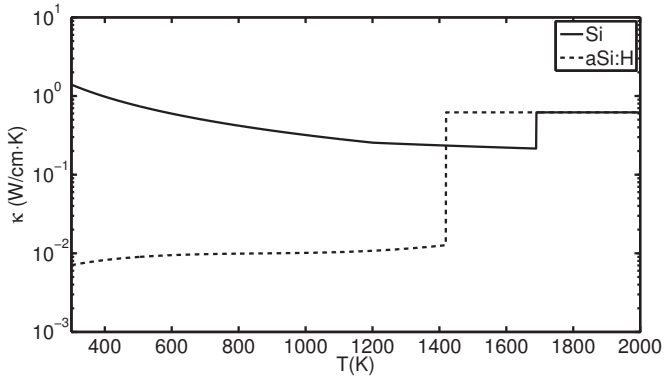

Figure 3.10: The thermal conductivity of c-Si and a-Si:H. The values for the solid state c-Si and a-Si have been imported from Ong et al.[57], while the thermal conductivity of liquid silicon was reported by Kobatake et al.[81]. We have simulated the thermal conductivity with abrupt changes at the transition temperature.

general version of the heat diffusion equation (still in one-dimension)[4];

$$c_p(T)\rho(T)\frac{\partial T(x,t)}{\partial t} = \frac{\partial}{\partial x}\cdot\kappa(T)\left(\frac{\partial}{\partial x}\nabla\cdot T(x,t)\right) + S(x,t) \tag{3.15}$$

where the laser source term, $S(x,t)$, is given by

$$S(x,t) = \sqrt{\frac{4\ln 2}{\pi}}\frac{(1-R)F_p\cdot\alpha}{\tau_p}\exp\left(-\alpha x - 4\ln 2\frac{(t-t_{\rm peak})^2}{\tau_p^2}\right), \tag{3.16}$$

and has units of $\mathrm{W/cm}^3$. $t_{\rm peak}$ denotes the time for the peak fluence, F_p, in the Gaussian time distribution. The pulse duration, $t_{\rm p}$, is given at full-width-half-maximum (FWHM). The fluence is the pulse energy density, and it is given in J/cm^2. The peak fluence, F_p, of a perfect Gaussian beam profile is two times the average energy density;

$$F_p = \frac{2E_p}{\pi\phi_0^2}, \tag{3.17}$$

[4]This equation does not take into account heat transport by convection and thermal radiation.

where E_p is the pulse energy, and ϕ_0 is the $\frac{1}{e^2}$ radius of the Gaussian beam. In the modeling we have limited ourselves to one-dimensional simulations, and have therefore only used the Gaussian peak.

The complexity of Equation (3.15) is now far beyond the analytically solvable. We therefore applied a finite difference scheme to solve the equation. To also include the possibility of phase transitions we upgraded to the so-called total enthalpy version of Equation (3.15)[77];

$$\frac{\partial \Delta H(x,t)}{\partial t} = \frac{\partial}{\partial x} \cdot \kappa(T) \left(\frac{\partial}{\partial x} \nabla \cdot T(x,t) \right) + S(x,t), \tag{3.18}$$

where $\Delta H(x,t)$ is the total enthalpy;

$$\Delta H(x,t) \approx \int_{T_0}^{T} \rho(T') c_p(T') \mathrm{d}T' + \mathbf{\Theta}(T - T_m)\Delta H_m + \mathbf{\Theta}(T - T_V)\Delta H_V. \tag{3.19}$$

$\mathbf{\Theta}$ is the Heaviside function (1 if argument is positive, 0 if negative), ΔH_m and ΔH_v are the enthalpies of melting and vaporization, respectively, with T_m and T_v being the corresponding melting and vaporization temperatures. Since the phase transitions are of first order their derivatives become infinite at the transition temperature. This can potentially lead to numerical instabilities when solving Equation (3.18). We avoided the instabilities by representing the Dirac delta function by a Gaussian function with $\Delta T = 5$ K.

The sample is assumed to be at ambient temperature before each laser pulse. This assumption gives us the initial condition;

$$T(x,t) = T_0|_{t=0}. \tag{3.20}$$

Our experiments are performed at 20 kHz laser repetition frequency. This implies that there are 50 μs between each pulse which has a duration of approximately 100 ns. The initial condition is therefore valid also for spatial overlapping pulses since the time between two pulses is significantly longer than it takes for the sample to be back to ambient temperature after the pulse. We also assume that the

temperature is equal to the ambient temperature at infinite depth in the material;

$$T(x,t) = T_0|_{x\to\infty}. \tag{3.21}$$

We have run the simulations with 10 μm of c-Si under the a-Si film. This is sufficient to keep the error associated with boundary condition 3.21 at a negligible level. Finally, we have also assumed that there is no energy loss at the front surface;

$$\frac{\partial T}{\partial x} = 0|_{x=0}. \tag{3.22}$$

This is a simplification, but for pulsed laser sources the energy loss at the surface, usually due to emission and convection, is negligible compared to the energy diffusion towards the bulk of the c-Si wafer. The left hand side of Equation (3.22) is therefore usually put equal to zero with a good approximation[82].

The interface thermal resistance between a-Si and c-Si was implemented by introducing the resistance over a layer with a thickness of 5 nm between the materials. A value of 0.0054 $cm^2 \cdot K/W$ was used according to Kuo et al. [58], corresponding to a thin layer of native oxide between a-Si and c-Si. In general, the interface between two different materials is always resistive to heat flow, even for atomically perfect interfaces. This is due the different vibrational and electronic properties on each side of the interface. The interface causes scattering of both electrons and phonons, and it leads to a discontinuity in the temperature distribution across the surface. For more in-depth modeling of laser interaction with c-Si, see for instance [83], and for laser interaction with a-Si, see [82].

3.3.2 Laser fluence ablation threshold

The dynamic model described in the previous subsection gives insight into the temporal and one-dimensional spatial temperature distribution of heat in a-Si on c-Si. We found a good agreement between experimental and modeled data. In order to be able to predict the laser fluence ablation threshold for a given thickness of the a-Si film, we have also developed a simplified analytically solvable static laser ablation model. The model is based on a model described by Matthias et al.[84]

when studying laser ablation of metal films on quartz. Our version of the model has been revised to also include the possibly of optical absorption in the substrate, in our case c-Si, and a thermal diffusion barrier at the a-Si−c-Si interface. All parameters are assumed to be constant, and we have used the values at 1000 K listed and referenced in paper IV. We assume that the absorbed laser irradiation is completely transferred into heat, and that there is a uniform temperature rise within the volume defined by the thermal diffusion length, l_{th}, after the laser pulse. By the first law of thermodynamics

$$\Delta T = Q_{\mathrm{abs}}/C_p. \tag{3.23}$$

ΔT is the temperature increment, Q_{abs} is the absorbed laser energy (density) and C_p is the volumetric heat capacity at constant pressure. We assume that a phase transition (solid-liquid or liquid-vapor) occurs at a critical energy density, $\epsilon_T = F_T/l_{\mathrm{th}}$, where F_T is the laser fluence threshold at the critical energy density. By accounting for the reflection, R, at the surface and light that is not absorbed in the film, (1-e$^{-\alpha d}$), nor in the substrate, (1-e$^{-\beta d_s}$), where α and β and d and d_s are the optical absorption coefficients and thicknesses of the a-Si film and the c-Si substrate, respectively, we end up with the following expression for the absorbed energy;

$$Q_{\mathrm{abs}} = F \cdot l_{\mathrm{th}}(1-R)\left[(1-e^{-\alpha d}) + \mathrm{e}^{-\alpha d}(1+\mathrm{e}^{-\beta d_s})\right], \tag{3.24}$$

where F is the incident pulse fluence. By setting Q_{abs} equal to the critical energy density, ϵ_T, at the temperature of the phase transition, and combining Equations (3.23) and (3.24), we get the following expression for the fluence threshold for melting

$$F_{TM} = \frac{\Delta T_M}{(1-R)\left[(1-\mathrm{e}^{-\alpha d}) + \mathrm{e}^{-\alpha d}(1-e^{-\beta d_s})\right]} l_{\mathrm{th}} C_{\mathrm{p}}, \tag{3.25}$$

where ΔT_M is the needed temperature increment for melting. Still, the above equation does not take into account the different thermal diffusion lengths and the different heat capacities of a-Si and c-Si. In the following the heat capacities have been taken additively into account and weighted between the film and the substrate. It changes linearly from the heat capacity of c-Si at $d = 0$ (surface) to the heat capacity of a-Si at $d = l_{\mathrm{th}}$ and above. We define this heat capacity as the

effective heat capacity, $C_{\mathrm{p,eff}}$. We also need to find an effective thermal diffusion length, $l_{\mathrm{th,eff}}$. In order to find an appropriate expression for the latter, we need to find an effective thermal conductivity, and thereby an effective diffusivity, see equation (3.11). The effective thermal conductivity is found by adding the thermal resistivities of a-Si, c-Si, and the interface as

$$\frac{d + l_{\mathrm{th,si}}}{\kappa_{\mathrm{total}}} = \frac{d}{\kappa_{\mathrm{aSi}}} + \frac{l_{\mathrm{th,si}}}{\kappa_{\mathrm{cSi}}} + R_{\mathrm{int}}, \tag{3.26}$$

where κ_{aSi} and κ_{cSi} are the thermal conductivities of a-Si and c-Si, respectively, R_{int} is the interface resistance, and $l_{\mathrm{th,si}}$ is the thermal diffusion length of c-Si. Finally,

$$D_{\mathrm{eff}} = \frac{\kappa_{\mathrm{total}}}{C_{\mathrm{p,eff}}}, \tag{3.27}$$

and $l_{\mathrm{th,eff}} = \sqrt{2D_{\mathrm{eff}}\tau_p}$. This leaves us with the following expression for the fluence ablation threshold for melting;

$$F_{TM} = \frac{\Delta T_M}{(1-R)\left[(1-\mathrm{e}^{-\alpha d}) + \mathrm{e}^{-\alpha d}(1-\mathrm{e}^{-\beta d_s})\right]} l_{\mathrm{th,eff}} C_{\mathrm{p,eff}}. \tag{3.28}$$

The corresponding expression for surface vaporization can then easily be found by replacing ΔT_M by the needed temperature increment for vaporization, ΔT_V, plus the latent heat for melting divided by the volumetric heat capacity of a-Si;

$$F_{TV} = \frac{\Delta T_V + \Delta H_M / C_{p,\mathrm{aSi}}}{(1-R)\left[(1-e^{-\alpha d}) + e^{-\alpha d}(1-e^{-\beta d_s})\right]} l_{\mathrm{th,eff}} C_{\mathrm{p,eff}}. \tag{3.29}$$

The latter model was found to be in good agreement with experimental data for the fluence threshold for laser ablation when including a thermal interface resistance of 0.0054 cm^2·K/W, which corresponds to a sample with a native oxide between a-Si and c-Si[58, 59]. The match between the experimental data from paper III and the model and the effect of altering the interface thermal resistance from 0.0013 cm^2·K/W to 0.0054 cm^2·K/W can be seen in Figure 3.11. 0.0013 cm^2·K/W corresponds to a clean surface between the two materials[58].

The covering PECVD oxide is not regarded as a part of the thermal simulations. It has an effect on the surface reflection, which has been taken into account, but

the oxide is regarded thermally insulating.

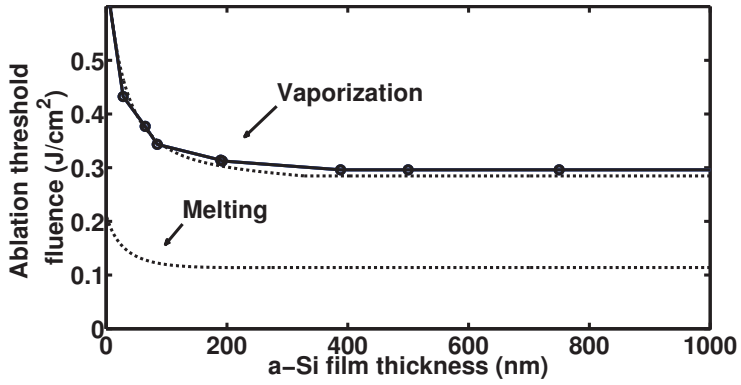

(a)

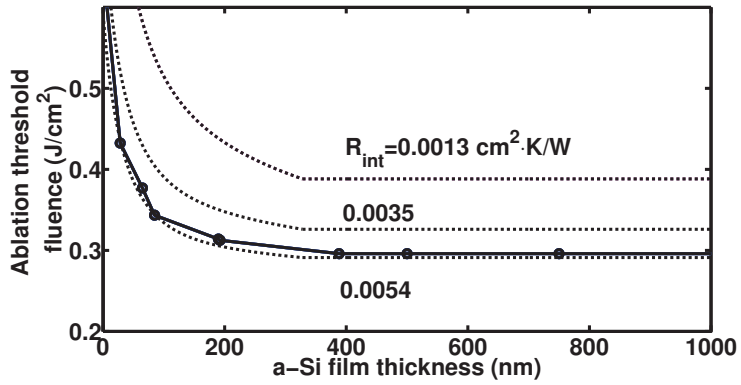

(b)

Figure 3.11: (a) Experimental data for the laser fluence ablation threshold of a-Si as a function of the film thickness (solid line with circles), shown together with the models for surface melting (Equation (3.28)) and vaporization (Equation (3.29)). The experimental data is from paper III. **(b)** The effect of increasing the interface thermal resistance from 0.0013 to 0.0054 cm^2·K/W in the model for surface vaporization (Equation (3.29)).

3.4 Doping

During the work with this thesis, the facilities at the IFE solar laboratory have been gradually upgraded. Initially, doping of wafers was done by a custom-made spray-on system where diluted spin-on-dopant (SOD) sources were sprayed on to the samples. SODs typically consist of phosphorous pentoxide (P_2O_5) or boron trioxide (B_2O_3) interchained with SiO_2 dissolved in alcohols and ketones[85]. The samples are dried to remove the solvents. Phosphorus and boron are then released upon reduction of P_2O_5 and B_2O_3, respectively, at high temperature in a belt furnace as;

$$2P_2O_5(l) + 5Si(s) \rightarrow 4P(s) + 5SiO_2(s), \tag{3.30}$$

and

$$2B_2O_3(l) + 3Si(s) \rightarrow 4B(s) + 3SiO_2(s), \tag{3.31}$$

and driven into the substrate.

Figure 3.12 shows a spatially resolved sheet resistance map of a series of wafers used in a preliminary experiment to optimize the homogeneity of boron-emitters on n-type 5 inch Cz wafers. The external air flow of the atomizing nozzle is gradually reduced from left to right. Though the optimized result shown in the figure is satisfactory, the spray-on system was found hard to maintain and keep stable, and re-optimization of the spraying parameters had to be done frequently. We therefore switched to using a tube furnace when this became available in the IFE laboratory.

The diffusion process in a tube furnace is fundamentally the same as diffusion in a belt furnace. It can also be divided into two sequences; deposition and drive-in. In contrast to SODs, where P_2O_5 and B_2O_3 and are sprayed directly onto the silicon wafer, gaseous phosphorus oxychloride ($POCl_3$) or boron tribromide (BBr_3) is fed into the tube to react with externally supplied O_2 as

$$4POCl_3(g) + 3O_2(g) \rightarrow 2P_2O_5(l) + 6Cl_2(g), \tag{3.32}$$

and

$$4\mathrm{BBr_3(g)} + 3\mathrm{O_2(g)} \rightarrow \mathrm{B_2O_3(l)} + 6\mathrm{Br_2(g)}, \tag{3.33}$$

for phosphorous and boron diffusion, respectively[85, 86]. The gaseous $POCl_3$ or BBr_3 condense on the silicon wafer surface and form a solid oxide. The drive-in step is then activated by temperature, and the reduction takes place as describe above in Equations (3.30) and (3.31) for phosphorous and boron, respectively. We found the homogeneity and reproducibility of the diffused layers to be significantly improved with the tube furnace[5].

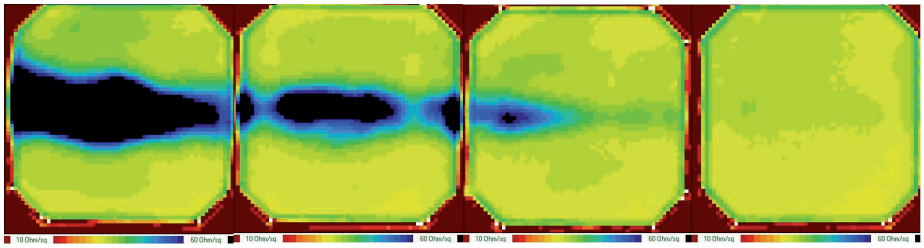

Figure 3.12: Spatially resolved sheet resistance map of a series of wafers used for optimization of the boron emitter homogeneity deposited by our custom-made spray-on system. The external airflow of the atomizing nozzle was reduced from left-most to the right-most picture. The resulting p^+ sheet resistance for the optimized spray-on parameters in these experiments had a spread in homogeneity of < 3 % at 60 $\Omega/\square$.

3.5 Lifetime and saturation current measurements

The effective minority carrier lifetime, τ_{eff}, of a silicon wafer can be expressed as the sum of the recombination rates in the bulk and on the surface. The recombination rate is in general inversely related to the recombination lifetime, and the

[5]The greatest disadvantage of $POCl_3$ and BBr_3 diffusion is the batch nature of the process. It is time and energy consuming, and as the industry is heading towards thinner wafers, the common way a stacking wafers vertically in a quartz boat will eventually leave manufacturers with an unacceptable yield[85].

effective lifetime of a sample can be expressed as

$$\frac{1}{\tau_{\text{eff}}} = \frac{1}{\tau_{\text{bulk}}} + \frac{1}{\tau_{\text{surface}}}, \tag{3.34}$$

where τ_{bulk} and τ_{surface} are the bulk and surface recombination lifetimes, respectively. The recombination rate in the bulk can further be divided into the sum of independent recombination mechanisms via the inverse recombination lifetimes as

$$\frac{1}{\tau_{\text{bulk}}} = \frac{1}{\tau_{\text{rad}}} + \frac{1}{\tau_{\text{Auger}}} + \frac{1}{\tau_{\text{SRH}}}. \tag{3.35}$$

τ_{rad}, τ_{Auger}, and τ_{SRH} are the radiative, Auger, and Shockley-Read-Hall recombination lifetimes, respectively. Since silicon is an indirect bandgap semiconductor, radiative recombination is low and negligible to a good approximation. Auger recombination is intrinsic to the material, and depends only on the base resistivity. It therefore sets an upper boundary for the theoretical effective lifetime of silicon. Shockley-Read-Hall recombination, on the other hand, occurs via defects levels in the bandgap, and depends therefore on the material quality. It is usually the dominant bulk recombination source in solar cells.

The surface of a silicon wafer can be regarded as a large imperfection in the crystal, and it represents a continuum of defects in the bandgap. If the surface recombination rate is low and equal on each side, τ_{surface} can be approximated by

$$\frac{1}{\tau_{\text{surface}}} = \frac{2S_{\text{eff}}}{W}, \tag{3.36}$$

where W is the wafer thickness and S_{eff} is the surface recombination velocity.

In silicon solar cells recombination in the emitter is also usually significant. It is therefore common to add the emitter recombination rate, $\frac{1}{\tau_{\text{e}}}$, to the other bulk recombination mechanisms in the expression for the effective recombination lifetime (see Equation (3.35)). Under the assumptions that the emitter is in low

injection[6], and that the depletion approximation is valid[7], it is possible get an analytical expression for an effective virtual surface recombination velocity that includes both surface and emitter recombination. The emitter, or depletion region, is treated as a virtual surface, and it can be shown that the expression for the effective emitter recombination velocity is given as [76, 85]

$$S_{\text{eff}} = J_{0e}\frac{N_{\text{D}} + \Delta p}{qn_i^2}, \tag{3.37}$$

where J_{0e} is the emitter saturation current density, N_{D} is the base doping density of an n-type wafer, n_i is the intrinsic carrier density, and Δp is the excess/photogenerated carrier density. By inserting equations (3.36) and (3.37) into (3.35), the total effective recombination lifetime of a silicon wafer with two equal emitters can be expressed as[87, 88]

$$\frac{1}{\tau_{\text{eff}}} = \frac{1}{\tau_{\text{SRH}}} + \frac{1}{\tau_{\text{auger}}} + 2J_{0e}\frac{N_{\text{D}} + \Delta p}{Wqn_i^2}. \tag{3.38}$$

In the next section we will show that the latter expression can be used to extract the empirical value for the emitter saturation current density, J_{0e}, as long as the recombination lifetime is not limited by Auger recombination in the bulk[88].

3.5.1 The generalized photoconductance method

The generalized photoconductance method combines the steady state and transient photoconductance methods into a unified robust measurement technique[89, 90]. The carrier continuity equation can be expressed as

$$\frac{d\Delta n}{dt} = g_E - U, \tag{3.39}$$

when there is no net current transport in the sample. Δn is the excess/photogenerated carrier density, and U and g_E is the recombination and generation rate, respec-

[6]The high doping density of the emitter ensures that it is always in low injection under standard operating conditions.

[7]Under the depletion approximation it is assumed that the space charge region is depleted of mobile charge carriers, and that the bulk of the semiconductor is everywhere neutral. These two regions are divided by an abrupt boundary.

tively. By simple manipulation we find that

$$\tau_{\text{eff}} = \frac{\Delta n}{g_E - \frac{d\Delta n}{dt}}, \tag{3.40}$$

under the assumption that τ_{eff} is inversely proportional to the recombination rate. The charge carriers generated in the sample due to illumination cause the conductance of the sample to increase. This elevated conductance is known as the photoconductance, σ_p. Assuming that the excess carrier densities of majority and minority carriers are equal, the photoconductance can be expressed as[90]

$$\sigma_p = q\Delta n(\mu_n + \mu_p)W, \tag{3.41}$$

where Δn now is the average excess carrier density throughout the whole thickness, W, of the wafer. μ_n and μ_p are the electron and hole mobilities, respectively.

We used a Sinton WTC-100 setup to extract the emitter saturation current density, J_{0e} under high injection conditions. To get accurate results the injection of minority carriers needs to be at least 10 times the doping density[87]. Trap-assisted recombination mechanisms saturate at a fixed level when the injection of photogenerated carries exceed the doping density. Since Auger recombination is intrinsic to the material, it can be deducted from Equation (3.38). This leaves the emitter saturation current density as the only unknown and the parameter limiting the effective lifetime. J_{0e} is calculated as the slope of the inverse Auger-corrected lifetime, which becomes linear at high injection. An output window from the Sinton WTC-100 software setup is shown in Figure 3.13.

3.5.2 μW-PCD

In microwave PCD (μW-PCD) the photoconductance is measured through the reflectance of a microwave signal directed at the sample. The decay of the reflected microwave power is utilized for estimation of the excess carrier decay. A laser pulse is commonly used to generate the charge carriers, since the very rapid decay times of laser diodes ensure negligible steady state contributions even for low

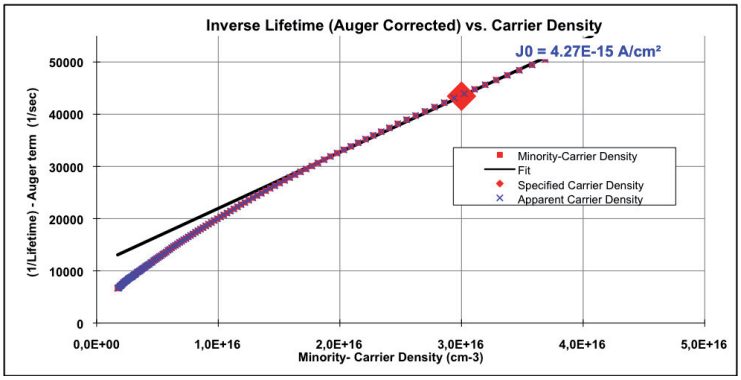

Figure 3.13: Screen print from the Sinton WTC-100 software setup. The emitter saturation current density, J_{0e}, is extracted from high-injection generalized photoconduction measurements, as the slope of the generated Auger-corrected lifetime curve.

lifetime wafers. The effective lifetime can, thus, be approximated by

$$\tau_{\text{eff}} = -\frac{\Delta n}{\frac{d\Delta n}{dt}}, \tag{3.42}$$

where the steady state generation term from Equation (3.40) has been removed. A Semilab WT-2000 setup was used to generate spatially resolved carrier lifetime maps during the work with paper II. A schematic drawing of the equipment is shown in Figure 3.14, while a spatially resolved lifetime map can be seen in Figure 3.15.

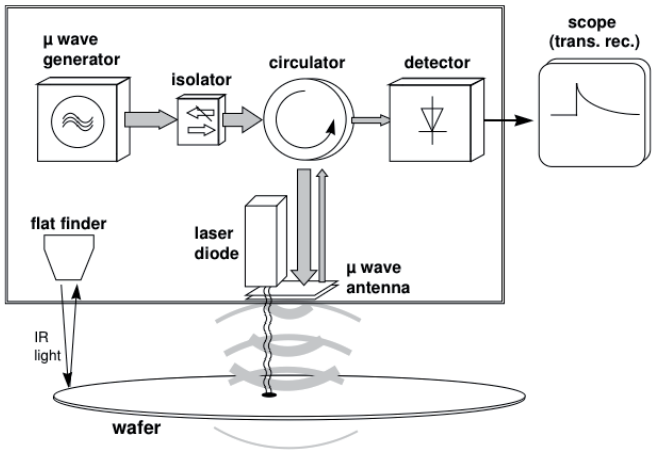

Figure 3.14: Schematic drawing of a Semilab WC-2000 μW-PCD system. (Source: Semilab Rt., Budapest, Hungary.)

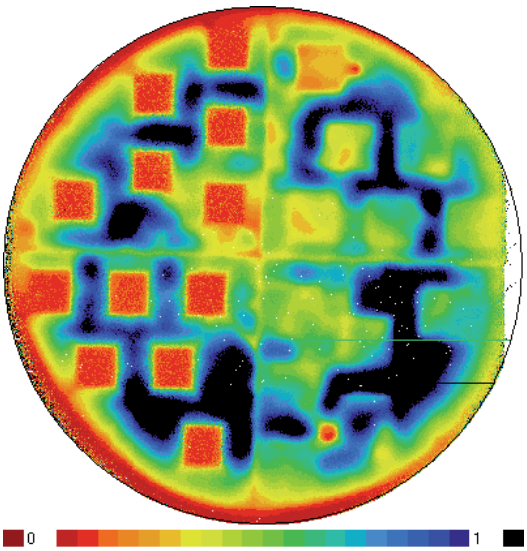

Figure 3.15: A spatially resolved minority carrier lifetime map of four different samples put back together into the original 4 inch round wafer. The minority carrier lifetime is here shown in a relative scale, where black means long lifetime and red means low lifetime. The low lifetime areas in the left samples result from laser induced damage. The measurements were done with a Semilab WT-2000 equipment. This picture is taken from paper II.

3.6 Thickness measurements

3.6.1 Ellipsometry

We used a variable angle spectroscopic ellipsometer (VASE) from J. A. Wollam Co., Inc. to determine the thickness of single layers of a-Si:H and SiO_2 and double-layers thereof. Ellipsometry is commonly used to determine optical properties and thicknesses of thin films. It lends its name from the general, elliptic, polarization state of light. The technique is both versatile, powerful and robust. In principle, the ellipsometer measures the change in polarization of light upon reflection from a sample. The polarization state of the incident light is conveniently decomposed into a transverse (s) and a parallel (p) component relative to the sample surface. The complex reflection ratio, ρ, is typically parametrized by Ψ and Δ as

$$\rho = \frac{r_p}{r_s} = \tan(\Psi)e^{i\Delta}, \tag{3.43}$$

where r_p and r_s are are the normalized amplitudes of the p and s components, respectively. $\tan(\Psi)$ is, thus, the amplitude ratio after reflection, while Δ is the corresponding phase shift. Since the technique only utilizes relative, rather than absolute, values, ellipsometry is insensitive to fluctuations in the light source, and no standard sample or reference beam is needed. However, as the ellipsometry technique is indirect, it is not possible to directly convert the measured values into physical material properties. It requires comparison of simulated data from a model with the measured values. The film thickness is determined by interference between light reflecting from the surface and light traveling through the film(s) and reflecting from the surface between the thin film and the substrate and between thin films in multilayer stacks. The interference can be either constructive or destructive, depending on the relative phase of the rejoining light. In general, the light interference involves both phase and amplitude information, and the phase information obtained from Δ is sensitive enough to obtain information of films down to sub-monolayer thickness. In our modeling the film thickness was used as a fitting parameter without adjusting the default optical constants for a-Si and SiO_2 from Palik[55]. A very good fit between measured and simulated data was obtained for both SiO_2 and a-Si. For some samples we also double-checked the

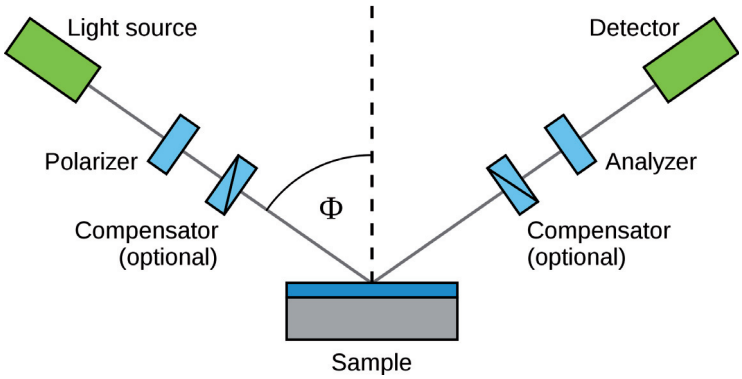

Figure 3.16: Schematic drawing of an ellipsometry setup. (Source: http://en.wikipedia.org/wiki/Ellipsometry)

film thickness with a profilometer to confirm that the ellipsometer numeric fit was a global minimum.

3.7 Contact deposition and resistance measurements

For contact deposition we used DC-magnetron sputtering of aluminum. A plasma is initiated by applying a large voltage across a gap of low-pressure inert gas. Highly energetic ions strike a target containing the material to be deposited. Contrary to the PECVD case, the target, and not the sample, must be placed on the electrode with the minimum ion flux. We have used argon to supply the chamber with an appropriate pressure for deposition, 3.1×10^{-3} mbar. We used a deposition power of 3 kW. The available sputtering system in our lab is an inline system from Leybold Optics.

3.7.1 The transfer length method

Solar cell contact resistance, and a technique for its measurement was discussed by Schroder and Meier[91, 92]. We used the so-called transfer length method to extract the contact resistance at the semiconductor-metal interface after laser

ablation of a-Si:H and a-SiO_x:H and subsequent sputtering of aluminum. The so-called transfer length, L_T, is a measure of the distance over which most of the current is transferred from the emitter into the contact and vice versa, see Figure 3.17. The relation between L_T and the specific contact resistance, ρ_c, is given by;

$$L_T = \sqrt{\rho_c / R_S}, \tag{3.44}$$

where R_S is the emitter sheet resistance. The specific contact resistance, ρ_c arises because of the potential barrier between metal and semiconductor and has units of $\Omega{\cdot}cm^2$. A more detailed description of the method and the results obtained can be found in paper V.

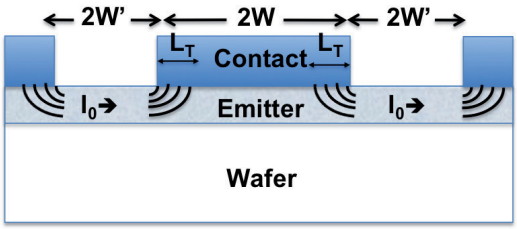

Figure 3.17: Schematic drawing of the current flow into and out of a contact. L_T is the so-called transfer length, which is a measure of the distance over which the current is transferred from the emitter into the contact pad and vice versa. The Figure is taken from paper V. 2W and 2W' which are the width of a contact bar and the width between two contact bars, respectively, belong to a more detailed description of the transfer length method and can be found in the paper.

Chapter 4

Results and discussion

In this chapter experimental results that are not discussed in the appended papers are presented. The results are mainly related to process steps that are needed in order to combine the already presented processing steps if they are to be used in the production of a BC-BJ silicon solar cell.

4.1 Diffusion barriers

During the work with this thesis, several different diffusion barriers have been tested with the aim to aid the separation of the doped areas of different polarity on the backside of a BC-BJ silicon solar cell. We have tested the barriers both against phosphorous and boron diffusion. However, the approach we have envisioned for structuring of the backside of the BC-BJ silicon solar cell only requires that the diffusion barrier holds against phosphorous doping. This is because the wafer is assumed uniformly doped with boron on the backside prior to the laser structuring. Early in the process of testing diffusion barriers we sprayed on liquid dopant-containing sources from a custom-made spraying system, see section 3.4. Tested diffusion barriers were PECVD SiO_2 (a-SiO_x:H) and SiN_x and a screen-printed TiO_2-containing paste. An early test of SiN_x as a diffusion barrier against a phosphorous-containing spray-on source is shown in Figure 4.1. The SiN_x was deposited through a shadow mask to obtain the desired pattern. The figure shows a spatially resolved sheet resistance map after heavy phosphorus dif-

fusion, and the interdigitated finger pattern clearly shows the contrast between where the nitride layer was deposited (high sheet resistance) and the areas in between. However, the measurements suffer slightly from the limited resolution of the mapping equipment. The obtained sheet resistance values are thus only to be considered as an indication of the doping level. Both PECVD SiN_x and screen-

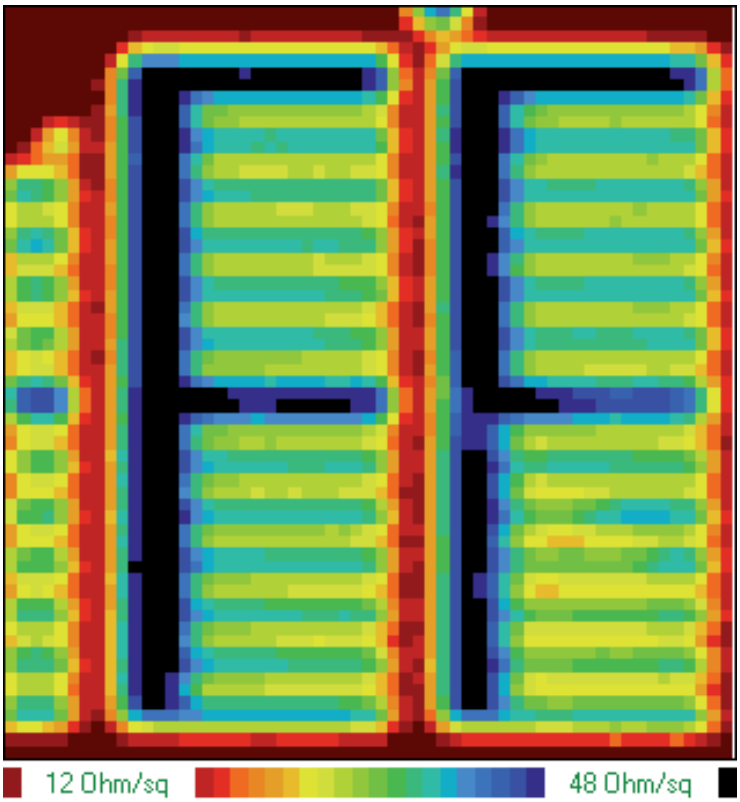

Figure 4.1: Spatially resolved sheet resistance map from a Semilab WT-2000. A finger-patterned PECVD SiN_x layer has been tested as a diffusion barrier against phosphorous doping. The dopant was diluted in solvents, sprayed on, dried, and driven-in using a belt furnace.

printed TiO_2 were found to react chemically with the boron-containing spray-on dopant source, and thus were extremely difficult to remove after diffusion. This

is the reason why we mainly have used SiO_2 as both a diffusion barrier and as an etching mask during the work with this thesis. We also continued to use (PECVD) SiO_2 after switching to using tube furnaces and gaseous dopant sources to keep the work consistent. However, the experiments in paper II, III, and V could also easily have been done with PECVD SiN_x instead of SiO_2. It would just require a re-optimization of the laser parameters. Actually, SiN_x has a better resistance both against KOH etching and phosphorus and boron doping, as it is denser than SiO_2. Figure 4.2 shows the phosphorous concentration in silicon as measured by secondary ion mass spectroscopy (SIMS) after diffusion through SiO_2 layers of different thicknesses. With a SiO_2 thickness of 450 nm, which is what we mainly have used during the work with this thesis, the phosphorous peak is reduced by 4 orders of magnitude and falls off to the base level (measured on n-type 1-3 Ω·cm wafers) within 40 nm. The small offset of the peak doping from the surface is most likely attributed to redistribution of dopants during a built-in oxidation step in the diffusion process. Fast diffusion of phosphorous in the thermal oxide on the surface will give the profiles seen in Figure 4.2, even if the segregation coefficient of phosphorous is around 10 during oxidation, meaning that the resulting doping concentration in the silicon will be higher than in the oxide[52]. We performed the same diffusion barrier test also for boron doping. The result is shown in Figure 4.3. As can be seen from the figure, the penetration of boron through SiO_2 is more significant than that of phosphorous. The segregation coefficient of boron is less than 1, which makes the peak offset from the surface more significant for the unmasked boron profile than for the corresponding phosphorous profile[52]. However, we believe that the absence of an offset for the masked boron-profiles is due to slow oxidation of the surface for low boron concentrations.

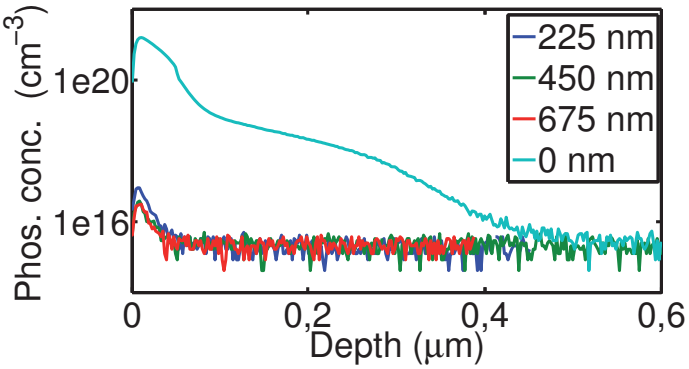

Figure 4.2: Phosphorus concentration as a function of depth after diffusion in a tube furnace. Layers of a-SiO$_x$:H with different thicknesses have been tested as diffusion barriers. 0 nm represents an unmasked sample. The results are obtained from secondary ion mass spectroscopy (SIMS).

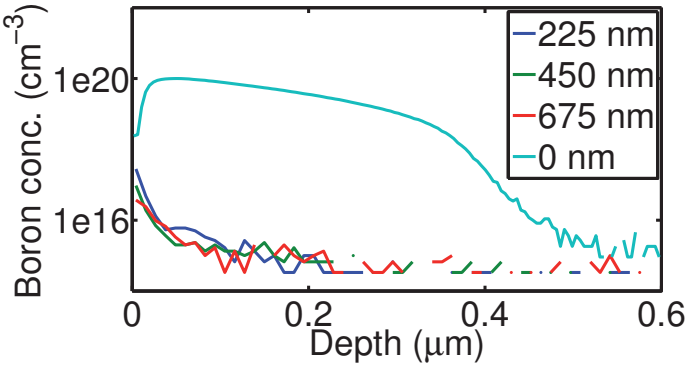

Figure 4.3: Boron concentration as a function of depth after diffusion in a tube furnace. Layers of a-SiO$_x$:H with different thicknesses have been tested as diffusion barriers. 0 nm represents an unmasked sample. The results are obtained from secondary ion mass spectroscopy (SIMS).

4.2 Contact separation

Different methods exist for contacting of BC-BJ silicon solar cells. The approach we have used resembles somewhat a method developed by Sinton et al. for self-aligned contacts on BC-BJ silicon cells[34]. Their method is based on evaporation of metal on the full backside surface and subsequent chemical contact separation due to different morphologies, and thus etch rates, on the horizontal and vertical planes of the structure, see Figure 4.4. A version of this method is also adapted in the RISE solar cell developed by Engelhart et al. at Institut für Solarenergieforschung, Hameln (ISFH)[38, 93], see section 2.3.

Instead of evaporation we have used in-line sputtering, mainly due to the availability of equipment, see section 3.7. We have used the geometry of the backside structures together with a constantly moving sample carrier to obtain a low metal coverage fraction on the flanks. Subsequently, we used an isotropic aluminum etch to separate the metal contacting the different polarity regions on the backside of the cell by removing the thin aluminum layer on the flanks, see Figure 4.5. The coverage fraction depends solely on the sputtering angle and on the trench depth, see Figure 4.4. A somewhat similar approach was also attempted by Hezel et al., when developing a self-aligned contacting technique by oblique evaporation[94, 95, 96]. Their method was, on the other hand, not originally intended for back-contacted solar cells. A sample with deposited aluminum is shown after etching in Figure 4.6.

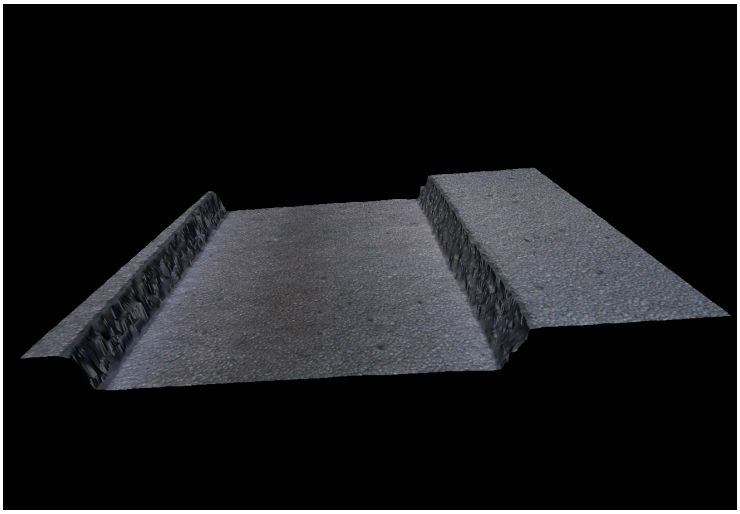

Figure 4.4: Optical microscope profiling picture of a sample after aluminum deposition by sputtering. The width and depth of the trench are 100 μm and 12 μm, respectively.

(a)

(b)

(c)

Figure 4.5: (a) Sketch of the backside of a BC-BJ cell prior to sputtering. The drawing is shown upside-down and is not to scale **(b)** Same structure after sputtering of aluminum **(c)** Structure shown after isotropic etching of aluminum. The thin aluminum layer at the flanks is removed, while a layer of reduced thickness remains on the horizontal planes. This process separates the metal contacting the different polarity regions on the backside of a BC-BJ silicon solar cell.

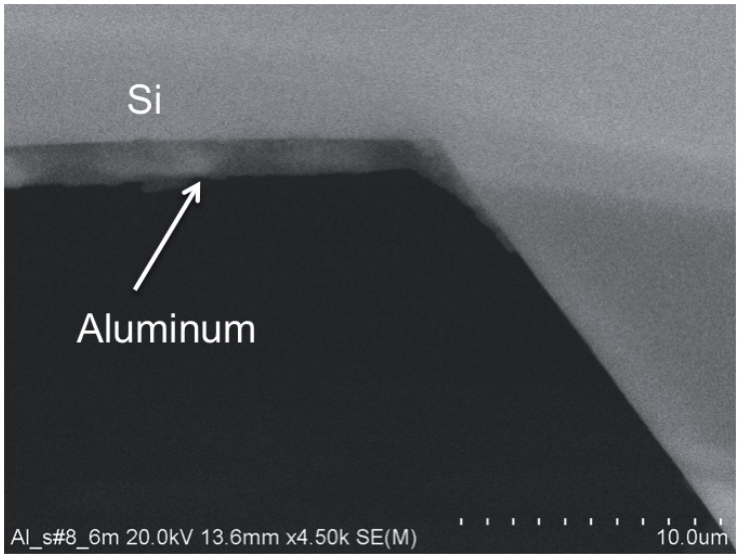

Figure 4.6: SEM picture of a sample after aluminum sputtering and an isotropic etch uniformly removing the aluminum on the sample. The picture shows that the metal is completely removed at the flank, while remaining in the trench.

4.3 Sketch of a BC-BJ silicon solar cell process flow

In the following section, a sketch of one possible manufacturing process for a full BC-BJ silicon solar cell is presented. The process is partly based on the experiments described in this thesis and in the appended papers. The different process steps are not described in detail, and cleaning steps prior to and during the process are left out. It is also worth noting that the process steps presented in the appended papers and in this thesis might separately be as useful for other solar cells design as for BC-BJ silicon solar cells. The figures in the following illustrate some of the different process steps. The wafers are shown upside-down and the figures are not to scale.

- We start with a n-type Cz wafer. The base resistivity should preferably in the order of 2 Ω·cm[35].

- The emitter (p^+) is introduced by single-sided boron diffusion. The diffusion can be done with the wafers back-to-back in the diffusion furnace. Alternatively it can be done by pre-depositing a low-temperature diffusion barrier, preferably SiN_x, on the front-side by PECVD prior to the diffusion.

- A layer of SiO_2 is deposited by PECVD on the backside of the wafer. The SiO_2 is first to function as an anti-reflection coating for the laser irradiation,

then as an etching mask against an aqueous KOH solution, and finally as a barrier against phosphorous diffusion.

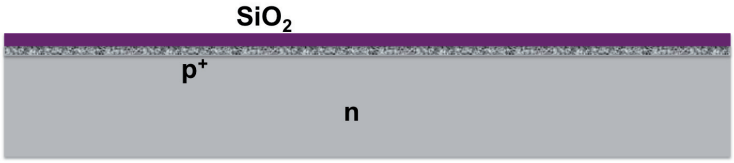

- The SiO_2 is locally removed together with the underlying p^+ layer by laser ablation. This results in an interdigitated finger pattern on the backside of the of the wafer. The laser irradiation leaves a thermally damaged zone near the wafer surface.

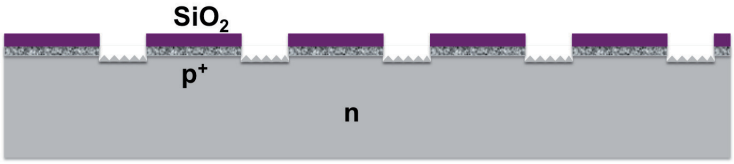

- The thermally induced damage is removed by etching in a high concentration high temperature aqueous KOH solution, see paper II.

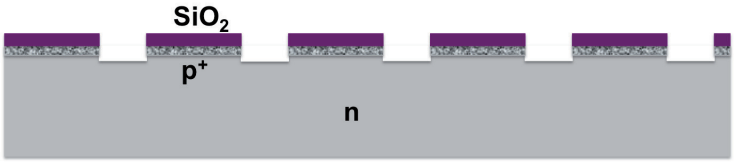

- The front-side is textured in a weak alkaline solution. The texturization can potentially be done in the same process step as the damage removal, but this will need some further optimization as the desired concentrations for the two different alkaline etching processes are quite different.

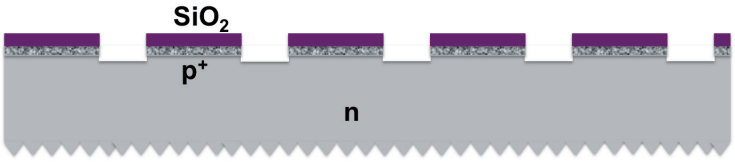

- The non-ablated SiO_2 layer serves as a barrier against phosphorous diffusion. At the same time a n^+ back-surface field (BSF) is established in the SiO_2-ablated, KOH-etched grooves, resulting in interdigitated fingers of opposite polarity with the BSF at an elevated level compared to the emitter. A front-surface field (FSF) can be introduced during the same process step, or in an additional diffusion step. The SiO_2 is stripped off in HF after the diffusion.

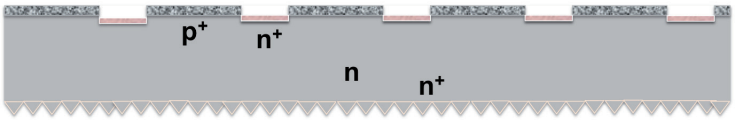

- The backside of the wafer is covered by a double-layer of PECVD SiO_2 and a-Si. The double-layer passivates the back-surface and serves as a buffer for the laser irradiation. The desired thickness of the different layers depends on the laser used in the subsequent laser ablation step. Herein, the best results were obtained with an a-Si layer thickness of 180 nm and a SiO_2 layer thickness of approximately 400 nm, see paper III. A laser with a shorter pulse duration and possibly also shorter wavelength would lower the thickness requirements of the a-Si layer, see paper III and IV.

SiO_2/a-Si

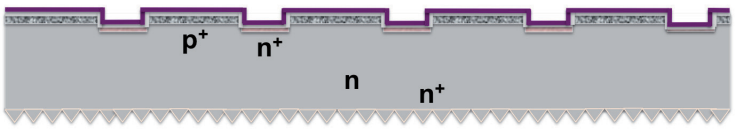

- A laser is used to make local contact openings to the doped silicon through the double-layer of a-Si/SiO_2. The desired coverage fraction of laser holes depends on the quality of the laser ablation and the contacts deposited in the following step. Based on the experiments and simulations described in paper V, the metal coverage fraction should preferably be in the range 5-10 %.

SiO_2/a-Si

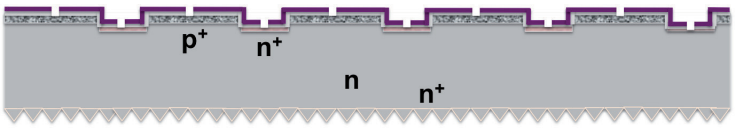

- Aluminum is deposited by oblique in-line sputtering. The geometry of the sample together with the movement of the sample carrier relative to the target, results in a graded aluminum layer thickness. Sputtering was chosen mainly because of equipment availability. For large area cells, alternative or additional contacting schemes should be investigated.

Al/SiO_2/a-Si

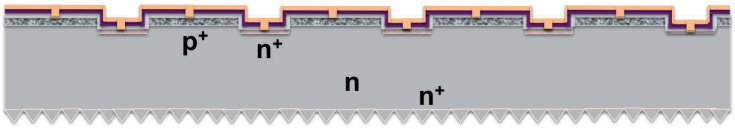

- An isotropic aluminum etching solution is used to remove the aluminum at the flanks, thus separating the p^+ and n^+ contacts. See previous section 4.2 for more detailed figures.

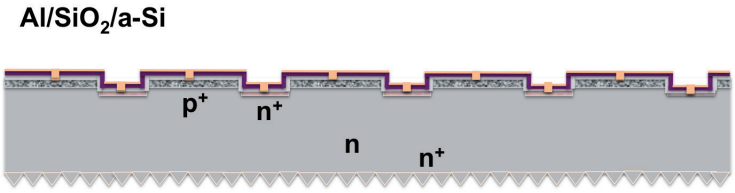

- Finally, an anti-reflective/passivating coating is deposited on the textured front-surface. The coating could be made from solely a PECVD SiN_x layer. It is also possible to deposit a PECVD double-layer consisting of a very thin a-Si layer near the surface and a SiN_x layer on top. The possibility of a graded SiN_x/a-Si layer should also be looked into. Yet another possibility is to introduce a thin thermal oxide in combination with the SiN_x layer. The thermal oxide would have to be introduced at an earlier stage in the process, preferably before the back-surface passivation step.

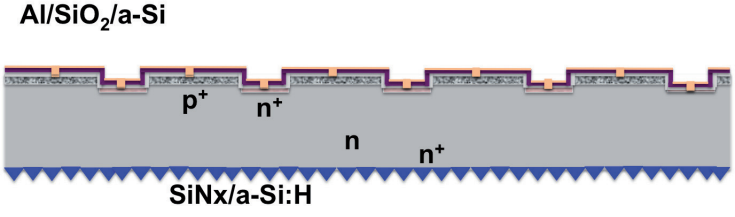

Chapter 5

Simulating back-junction silicon solar cells

5.1 The Silvaco-ATLAS device simulator

During the work with this thesis, we have used the ATLAS device simulator[97] within the Silvaco simulation framework[98] to model the performance of BC-BJ silicon solar cells. The device simulator enables simulation of electrical, optical, and thermal behavior of semiconductor devices through the finite element method. Our device model has evolved gradually during the whole Ph.D process. The simulations performed during the work with paper I is done with an early version of the device model. Still, the results from the paper give valuable insight into the physical mechanisms important for the performance of a BC-BJ silicon solar cell, and thereby also the design rules that have to be taken into account in the production of such a solar cell. In paper V a more mature version of the ATLAS BC-BJ device model is used together with an external ray tracing program to optimize the semiconductor to metal contact area fraction, and to explore the performance potential of a BC-BJ silicon solar cell design partially based on our experimental results.

When running current-voltage simulations of solar cells, the temperature rise has not been taken into account. That is, we have run the simulations at room temper-

ature (300 K), which is the default in ATLAS. Only during the work with paper III did we include the thermal behavior in the simulations. This was done to study the heat distribution in a silicon sample after an incident laser pulse. This chapter mainly describes some of the background and the simple basics of the device simulation model, rather than focusing on simulation results.

5.1.1 Defining a unit cell and mesh

Solar cells are relatively large semiconductor devices compared to for instance modern transistors. A commercially available silicon solar module is typically made out of 6 inch wafers, square (multicrystalline) or semi-square, (monocrystalline) with a thickness of approximately 200 μm. This is, in general, too large to obtain a satisfactory accuracy when simulating the device by the finite element method. We have therefore looked at the smallest repeating unit within our device, a so-called unit cell, shown in Figure 5.1. A sketch of a complete BC-BJ silicon solar cell is shown in Figure 2.3. The unit cell is sketched without anti-reflective coatings and textured surfaces. This is because the initial ray tracing and calculation of optical losses have been done externally to ATLAS and prior to the electrical simulations, see section 5.1.4. Unit cell simulations give insight into the behavior of the active area of the solar cell. To look at the performance of the total solar cell area one also needs to account for busbars and edge areas. The latter has not been included in the simulations performed during the work with this thesis.

The mesh needs to be sufficiently dense to make sure that the accuracy of the calculations is at a satisfactory level, while at the same time running efficient calculations without unnecessarily long computing times. The mesh density was optimized by repeating calculations with a sequence of finer meshes. A screenshot of a mesh used for simulations in the ATLAS device simulator is shown in Figure 5.2. The mesh has a higher density in the areas where there is high optical intensity and where the gradient of the electric potential is large. A built-in regrid function within ATLAS has been used to allow for a smooth transition of triangle sizes from dense to less dense regions in the mesh.

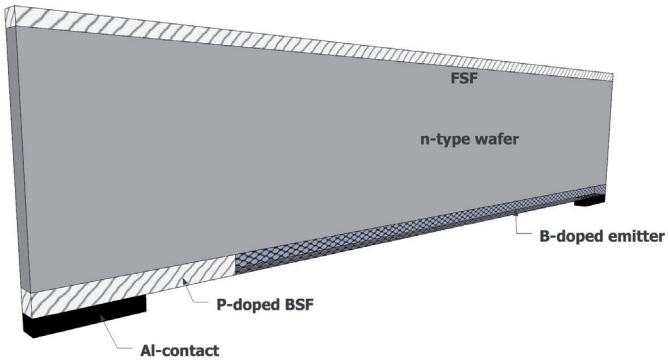

Figure 5.1: Schematic, simplified drawing of the two-dimensional unit cell used in the simulations of back-contacted back-junction silicon solar cells. The simulations are run in two dimensions. The width in the third dimension is set to 1 μm by default. BSF and FSF are the back-surface and front-surface fields, respectively. The drawing is not to scale.

5.1.2 Doping

Specification of doping concentrations and profiles can be done in a number of ways in Silvaco-ATLAS. Whole areas, such as a wafer or a unit cell, can be doped to a uniform background level for the wanted base resistivity. Doping profiles of emitter and back- and front surface fields can be given with a gaussian or complimentary error-function profile with specified peak concentration and width or junction depth. This was done in simulations performed during the work with paper I. The profiles can also be read from file to match experimentally measured profiles. In the simulations performed during the work with paper V, we used experimental diffusion profiles as determined with secondary ion mass spectroscopy (SIMS). Examples of SIMS profiles used in the simulation experiments are shown in Figures 4.2 and 4.3 for phosphorus and boron profiles, respectively. Finally, there is also a possibility of doing virtual diffusion experiments within the ATHENA process simulator, which is also a part of the Silvaco simulation framework. These profiles can then be implemented into the device simulations. The latter was tested during the work with paper VI.

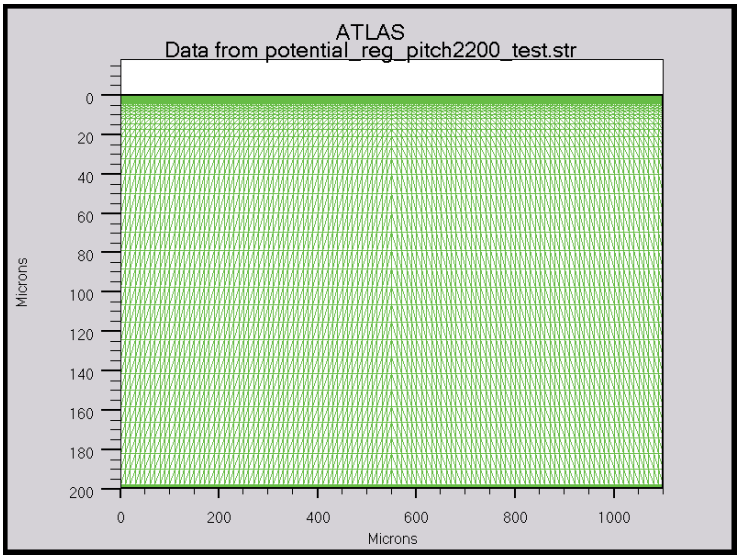

Figure 5.2: The mesh of a unit cell used the in ATLAS device simulator. The axis units are in μm, and the total mesh consists of approximately 35000 nodes. The density of the grid is significantly higher near the front- and back-surfaces.

Front-surface field

The advantages of using a front-surface field in BC-BJ silicon solar cells with a pitch compatible with industrial production with low-cost patterning techniques were extensively investigated and discussed by Granek and Hermle[28, 42, 99, 100, 101]. In summary, they conclude that an optimized front surface field

- reduces the influence from the front surface recombination velocity on the solar cell performance,
- improves the UV-stability of the cells compared to BC-BJ silicon solar cells without a FSF,
- improves the low illumination performance compared to cells without a FSF, and
- reduces the lateral series resistance of majority carriers.

They found that a deep gaussian profile gave the best results. In accordance with the results of Granek and Hermle, we have implemented a FSF with a Gaussian profile, a peak doping concentration of 3.8×10^{18} cm^{-3}, and a junction depth of 1.44 μm. The sheet resistance of the a profile is 148 $\Omega/\square$.

Base resistivity

McIntosh et al. investigated the influence of base resistivity on the performance of BC-BJ silicon solar cells[35]. They found that the optimum base resistivity of a BC-BJ cell processed with low-cost patterning techniques should be close to 2 Ω·cm for a wafer in the thickness range 160-280 μm. The efficiency of the cells did not drop significantly up to a base resistivity of 10 Ω·cm. The base doping is mostly a trade off between high short-circuit current density due to low recombination of minority carriers at high wafer resistivity, and high open-circuit voltage and low base series resistance at low wafer resistivity. We have therefore run most of our simulations with a wafer base doping of 2.4×10^{15} cm^{-3}, corresponding to a base resistivity of 2 Ω·cm for n-type wafers.

5.1.3 Contacts

Since the contact interface between metal and semiconductor is highly doped both for the emitter and the BSF ($\approx 10^{20}$ cm^{-3}), we have defined our contacts as ohmic electrodes rather than a specific material (aluminum in our case). This is done to avoid that the contacts are being treated as Schottky barriers, and thus unnecessarily increase the computing times. The current-flow in a BC-BJ silicon solar cell, and thus into the contacts, is substantially lateral. Therefore, a distributed (specific) contact resistance has been specified. The specific contact resistance is defined as the slope of the J-V curve at $V = 0$;

$$\rho_c = \left\{ \frac{\partial V}{\partial J} \right\} |_{V=0}. \tag{5.1}$$

In ATLAS this is calculated as

$$R_i = \frac{\rho_c}{w \cdot d_i}. \tag{5.2}$$

R_i is the resistance associated with node i at the surface, ρ_c is the user specified distributed contact resistance, d_i is the width of the surface segment associated with node i, and w is the width of the unit cell in the third dimension. The specific contact resistance used in the device simulation model during the work with paper V was set to 0.8 mΩ·cm^2, based on experimental results from the same paper. In our solar cell process, contacting was done by sputtering of aluminum through laser ablated holes in a double-layer of a-Si:H and a-SiO$_x$:H, see paper III, IV, and V.

5.1.4 Optical properties

Ray Tracing

The evaluation of optical loss mechanisms was performed externally to ATLAS. This was done due to limited possibilities of performing ray tracing with the full solar spectrum on structured surfaces in ATLAS. The ray tracing simulator TracePro[102] was used to calculate the optical losses due to reflection, parasitic absorption, escaped light, and free carrier absorption (FCA). The front surface was assumed perfectly covered with upright pyramids with a base width of 4 μm and an angle of 54.7° of the side walls to the surface orthogonal. The pyramids, which are typically fabricated by etching of the silicon surface in a weak alkaline solution, are introduced to lower the overall surface reflections. This is the industry standard for monocrystalline silicon solar cells. The pyramids were assumed covered with an anti-reflection coating of 10 nm SiO$_2$ close to the surface and 60 nm SiN$_x$ on top of the oxide. The thickness of the silicon wafer was set to 200 μm. On the backside, the original doping profiles were replaced by 300 nm deep uniform box profiles of phosphorus and boron. This was done to simplify the simulations while at the same time ensuring that the overall integrated FCA in the uniform profiles coincides with that of the actual doping profiles used in the device simulations. The unit cell used for the device simulation when also including the optical loss calculations is shown in Figure 5.3. We chose to cut off the optical simulations at 1100 nm due to very long absorption lengths, and thus computing times, above this wavelength. However, the intensity of the AM 1.5 solar spectrum is relatively low between 1100-1150 nm, and the error introduced

by this cut-off is expected to underestimate the short-circuit current density with around 0.2 mA/cm^2. At the same time, ray tracing has been reported to overestimate the anti-reflection effect of the pyramids[103]. The overestimation originates from the fact that light is not able to resolve the geometrical sharp corners of the textures, thereby allowing some direct transmission or reflection, not found in the ray tracing[103]. The main results from the ray tracing are shown in Figure 5.4. Primary reflection is the limiting optical loss mechanism at short wavelengths, while escaped light is dominating at long wavelengths.

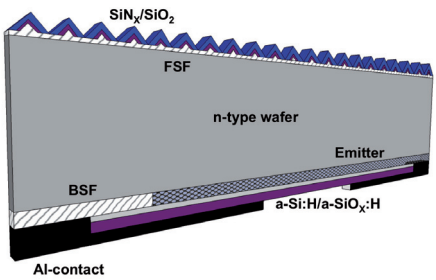

Figure 5.3: Schematic drawing of the unit cell used for the two-dimensional device simulations when also including ray tracing. The optical losses were calculated externally to ATLAS and prior to device simulation with the program TracePro. FSF and BSF are the front-and back-surface fields, respectively. The figure is simplified and not to scale.

Free carrier absportion

Free carrier absorption (FCA) is an intrinsic absorption process in silicon that involves transitions between free electrons or holes. It does not create an additional electron-hole pair, and can be a significant optical loss mechanism in some solar cell designs. An expression of FCA commonly used for solar cells was parametrized by Green [104];

$$\alpha_{fc} = 2.6 \times 10^{-18} \times n \times \lambda^3 + 2.7 \times 10^{-18} \times p \times \lambda^2, \tag{5.3}$$

where n and p are the electron and hole concentrations (in cm^{-3}), respectively, while λ is the wavelength in μm. FCA as function of wavelength is shown in Figure 5.5.

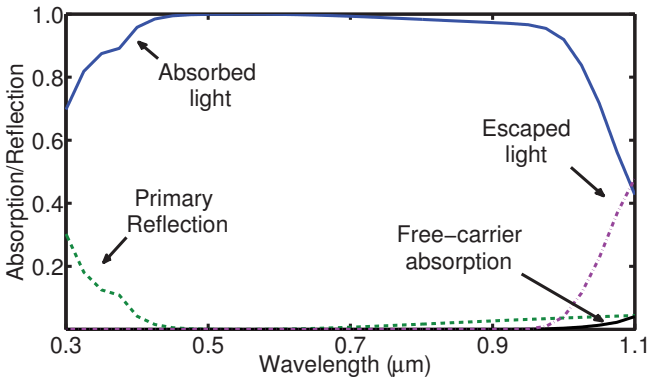

Figure 5.4: The fraction of light absorbed as a function of wavelength as calculated with ray tracing. The major optical loss mechanisms are also indicated in the figure.

The modified AM 1.5 solar spectrum

The calculated absorbed light was weighted against the standard AM 1.5 solar spectrum[23], see Figure 5.6. This was done by interpolating the absorbed light data points to obtain the same density of data points as in the AM 1.5 solar spectrum in the same wavelength range. Each data point in the original spectrum was then multiplied with the corresponding fraction of light absorbed at the same wavelength to obtain the modified spectrum. Finally, the modified spectrum was used as an input to the ATLAS device simulator in Silvaco.

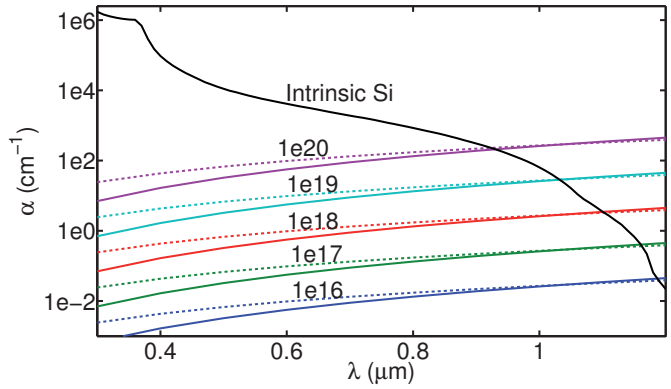

Figure 5.5: Free carrier absorption as function of wavelength for different doping concentrations according to Equation (5.3). The solid lines show FCA in n-doped silicon, while the dashed lines show the corresponding FCA in p-doped silicon. The absorption coefficient for intrinsic silicon is also shown for comparison.

5.1.5 Interfaces

Surface reflection and transmission

Since the incident solar spectrum already has been modified to account for primary reflection losses, the front surface is assumed non-reflective for incident illumination. Internally, however, the surfaces are now assumed fully reflective since also the escaped light has been accounted for in the ray tracing program. In other words, of the incoming modified spectrum nothing is reflected, transmitted, or lost optically in any way.

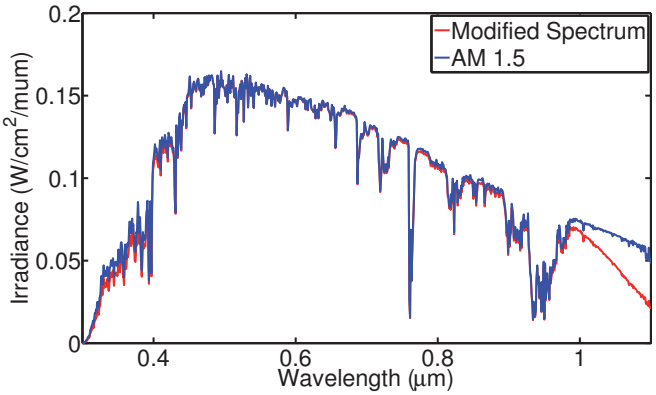

Figure 5.6: The standard AM 1.5 solar reference spectrum shown together with the modified solar spectrum used as input to the ATLAS device simulator. The modified spectrum is corrected for the optical losses such as surface reflection, escaped light, metal parasitic absorption, and free carrier absorption in the solar cell. The short wavelength losses are mainly due to primary reflection while the reduced irradiance at long wavelengths is caused by escaped light, free carrier absorption, and backside metal absorption.

Surface recombination

The front-surface recombination velocity has been calculated according to Cuevas et al.[105] assuming a thermally oxidized surface;

$$\begin{aligned} S &= S_0 && \text{for } N_D < N_{\text{ref}} \\ S &= S_0(N_D/N_{\text{ref}}) && \text{for } N_D \geq N_{\text{ref}}, \end{aligned} \tag{5.4}$$

where S_0 = 70 cm/s and $N_{\text{ref}} = 7 \times 10^{17}$ cm^{-3}, while N_D is the phosphorus doping concentration. On the backside, we have assumed the surface covered by a double-layer of passivating a-Si:H and a-SiO$_x$:H, see papers III and V. The surface recombination velocity has been calculated according to Aberle et al. as[76];

$$S_{eff} = \frac{J_{oe} N_A}{{n_i}^2}, \tag{5.5}$$

where J_{oe} is the emitter saturation current density, and input from experimental results obtained in paper III. The metal-semiconductor interface, i.e. the contact points, have been modeled with a surface recombination velocity of 3×10^6 cm/s[106].

5.1.6 Physical models

Bulk recombination

We used the default ATLAS model for Auger recombination which has been implemented according to Dziewior et al. as[107]

$$U_{Aug} = A_p(n^2p - n_0^2p_0) + A_n(np^2 - n_0p_0^2) \tag{5.6}$$

where n and p and n_0 and p_0 are the concentrations and equilibrium concentrations of electrons and holes, respectively. The Auger coefficients, A_p and A_n, are set to 9.9×10^{-32} cm^6/s and 2.8×10^{-31} cm^6/s, respectively.

In addition, we used a concentration dependent Shockley-Read-Hall recombination model which is also implemented to the ATLAS simulation software[108, 109, 110];

$$U_{SRH} = \frac{np - n_i^2}{\tau_{n,SRH}(p + p_t) + \tau_{p,SRH}(n + n_t)}. \tag{5.7}$$

n_t and p_t are the densities of electron and hole traps, respectively. $\tau_{n,SRH}$ and $\tau_{p,SRH}$ are the Shockley-Read-Hall lifetimes of electrons and holes, respectively, depending on the local doping concentration.

Carrier mobility

The carrier mobility has been specified by using a look-up table model to relate the low-field mobility at 300K to the impurity concentration[97]. The table contains empirical data for the carrier mobility of Silicon (only) at different doping concentrations.

Apparent bandgap narrowing

In the presence of heavy doping, experimental results have shown that the pn product in silicon becomes doping dependent[111]. This is in complete analogy with the law of mass action in ideal gasses. The relation $n_i^2 = n_0 p_0$ is not valid if the charge carries interact strongly with each other. Several different formulae for the decreased bandgap in silicon devices due to heavy doping have been suggested[112, 113, 114, 115]. However, a, parametrization of Cuevas et al. has found widespread use in the solar cell community[106];

$$\Delta E_G = A \ln(N/N_{\text{ref}}). \tag{5.8}$$

ΔE_G is here the change in bandgap due to the doping concentration, N. A is a constant

$$\begin{aligned} A &= 0 && \text{if } N < N_{\text{ref}} \\ A &= 14 \text{ meV} && \text{if } N \geq N_{\text{ref}}, \end{aligned} \tag{5.9}$$

and $N_{\text{ref}} = 1.4 \times 10^{17}$ cm^{-3}. The change in bandgap influences the carrier statistics through a change in the intrinsic carrier concentration;

$$n_i = n_{i0} \exp(\Delta E_G / 2kT) \tag{5.10}$$

It can be shown that this leads to a change in the effective dopant concentration as [116];

$$N_{\text{eff}} = N^{(1-A/kT)} N_{\text{ref}}^{(A/kT)}. \tag{5.11}$$

The most commonly used bandgap narrowing models referenced above are all empirical models deduced from transport measurements of highly doped silicon. Physical effects like carrier-carrier and carrier-impurity interactions are not separated from each other[117]. The model of Cuevas, which is the one we have used, includes several heavy doping effects. The combined total heavy doping effect is called the apparent bandgap narrowing. The model has therefore implicitly built in the effect of Fermi-Dirac statistics which also becomes significant at high doping densities. Fermi-Dirac statistics and apparent bandgap narrowing

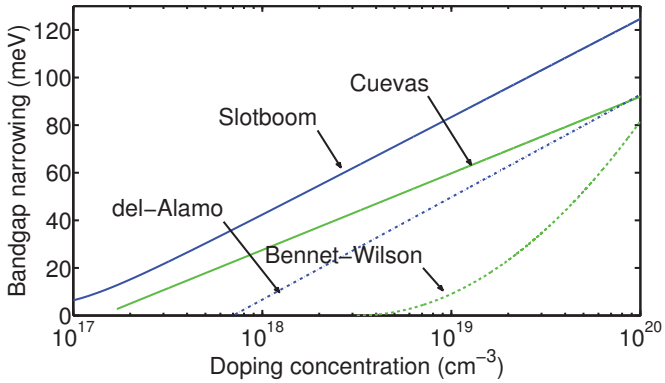

Figure 5.7: Apparent bandgap narrowing as a function of doping concentration according to different commonly cited references.

models can therefore not be used simultaneously in a consistent way. In the one-dimensional solar simulator program PC1D the BGN model of Cuevas is used but requires simple Boltzmann statistics to produce accurate results. A more consistent bandgap narrowing model derived from quantum mechanical principles was developed by Schenk[118] and implemented in the Dessis device simulator for simulation of solar cells by Schumacher et al.[117]. In our case this is beyond the scope, and Cuevas' model suffices for now. It is also worth noting that in paper I, which served as a preliminary investigation both of BC-BJ silicon solar cells and also the ATLAS device simulator itself, we used Slotboom's BGN model together with Fermi-Dirac statistics. As can be seen from Figure 5.7 there is a rather large discrepancy between the different models for BGN. Slotboom's model, which is the default in ATLAS, implies a more significant bandgap decrease than the other models. Even del-Alamo's model, which implies a more modest narrowing effect than the model of Slotboom et al., has been shown to overestimate the decrease in the bandgap for very heavy doping[117]. The use of Fermi-Dirac statics models will reduce carrier-carrier interactions, and thereby recombination. It is thus opposing the effect of bandgap narrowing. Even if it is inconsistent to use fermion carrier statistics together with empirical models for bandgap narrowing, the effect

of using Fermi-Dirac statistics was found to more or less cancel out the overestimated narrowing from Slotboom's empirical apparent bandgap narrowing, see Figure 5.7.

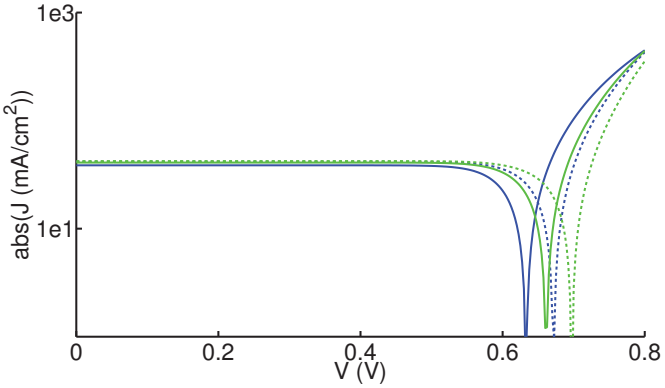

(a)

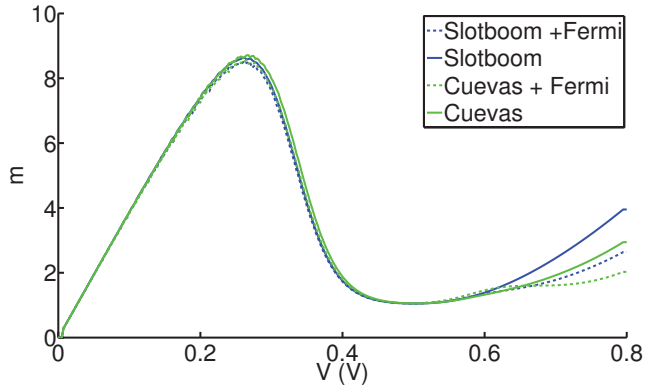

(b)

Figure 5.8: (a) Current-density (J, absolute value)-voltage (V) curves resulting from the activation of different combinations of bandgap narrowing models with different carrier statistics models. The solid lines show J-V curves with the use of Fermi-Dirac carrier statistics, while the dashed lines show simulations performed with simple Boltzmann carrier statistics. The blue lines indicate the use of Slotboom's bandgap narrowing model, while the green lines where simulated with the use of the bandgap narrowing model of Cuevas et al. **(b)** The local ideality factor, m, as function of applied voltage. The same combinations of line-color and style as described above also applies for the m-V curve. For a brief introduction to m-V-curves, see Section 5.2.

5.2 m-V curves

A powerful method to investigate the characteristics of a solar cell is to study the local ideality factor, m, as a function the applied voltage, V. m is related to the slope of the J-V curve, and can often reveal information that is not directly available from that curve. We let m be a free parameter so that

$$m = \frac{1}{V_{th}} \frac{dV}{d(\ln J_S)}. \tag{5.12}$$

V_{th} is the thermal voltage (see section 2.1), and J_S is the shifted current density, i.e. J minus the photogenerated current, J_{SC};

$$J_S(V) = J_0 \left[\exp((V + JR_S)/V_{th}) - 1\right] + \frac{V + JR_S}{R_{SH}}. \tag{5.13}$$

We have assumed that the light-generated current density is equal to the short-circuit current density, which is usually a good approximation. It is thus only distinguished from the dark current density by the sign before the voltage drop induced by the series resistance, (JR_S);

$$J_{\text{dark}}(V) = J_0 \left[\exp((V - JR_S)/V_{th}) - 1\right] + \frac{V - JR_S}{R_{SH}}. \tag{5.14}$$

This is a fundamental difference between p-n diodes in the dark and under illumination. Under illumination the total voltage is the sum of the applied voltage over the terminals and the voltage drop over the series resistance of the device. In the dark it is the applied voltage that drives the current, and the total voltage is the difference between the applied voltage and the voltage drop over the cell. This can be seen as a shift in the m-V curve between the shifted and dark J-V characteristics, see Figure 5.9. In practical devices, R_S and J_0 will in general be different in the dark and under illumination. The free parameter, m, must not be confused with the ideality factor that is associated with single recombination mechanisms. The resulting $m(V)$ comes from a combination of different recombination mechanism with different exponential behavior.

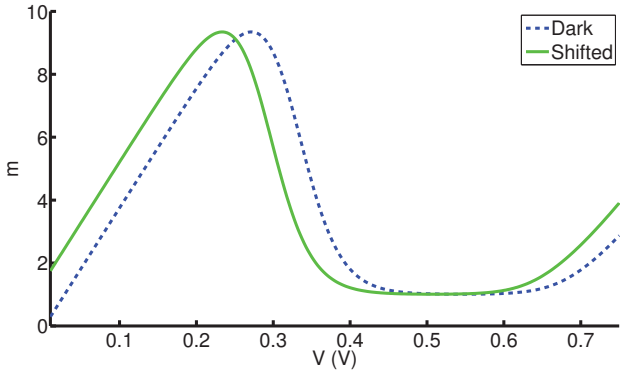

Figure 5.9: Dark (Eq. (5.14)) and shifted (Eq. (5.13)) m-V curves of a one-diode equivalent circuit with parasitic series (R_S) and shunt (R_{SH}) resistances. The saturation current density, J_0, was set to 10^{-9} A/cm^2, $R_S = 1\ \Omega$, and $R_{SH} = 10^6\ \Omega$

5.3 Tunneling

In a heavily doped p-n diode, charge carriers can tunnel through the junction barrier despite their insufficient energy. Tunneling through the bandgap can take place directly between bands on opposite sides of the barrier, so-called band-to-band tunneling (BBT)[119, 120], or via traps in the bandgap, so-called trap-assisted tunneling (TAT)[121], see Figure 5.10. For conventional front-contacted silicon solar cells this is not of any importance, as only one side of the p-n junction is heavily doped. In multi-junction solar cells controlled interband Esaki tunneling is used to let the current pass freely between the subcells[122, 123].

In solar cell designs where highly doped regions of opposite polarity are present on the same side, quantum mechanical tunneling of charge carrier can be a dominating effect. In combination with back-contacted silicon solar cells, tunneling and the effect of tunneling on the solar cell performance is not well described. Guo et al. discussed how tunneling could have an detrimental effect on the fill factor of double-side buried contact (DSBC) solar cells, but it was concluded that

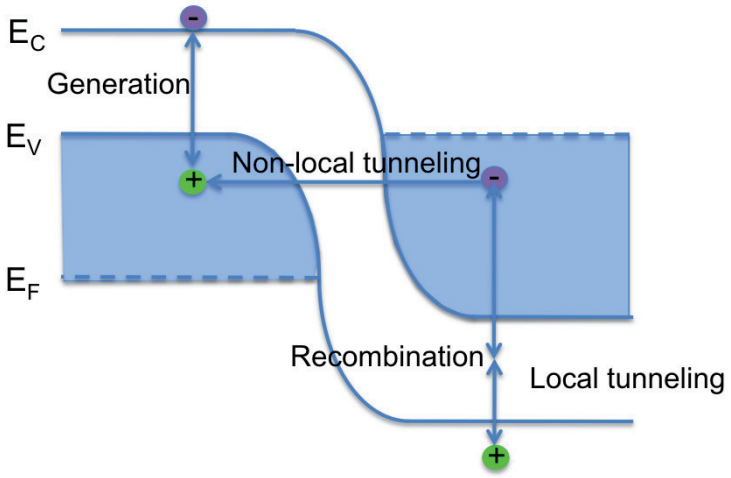

Figure 5.10: Schematic drawing of tunneling mechanisms in a highly doped p-n junction.

tunneling was not a likely cause of the low fill factor[124]. Both the Sunpower A-300 silicon solar cell and the RISE silicon solar cell of ISFH have highly doped regions of opposite polarity in direct contact with each other as a consequence of the design and production[37, 38], see section 2.3.

In order to get a better understanding of how the tunneling effect can influence the performance of BC-BJ silicon solar cells, we have performed simulations of BC-BJ silicon solar cells including lateral tunneling through the highly doped p- and n regions on the back of the cell, see Figure 5.11.

In order to be able to simulate the tunneling effect, a very fine rectangular mesh was superimposed on the original grid. The lateral distance between the grid points was set to 30 picometers in the tunneling direction. In Figure 5.12 the J-V curves of a small illuminated tunneling junction is shown when there is a doping density of 5×10^{19} cm^{-3} on both sides of an abrupt junction. The effect of the different doping mechanisms that dominate in different voltage ranges are

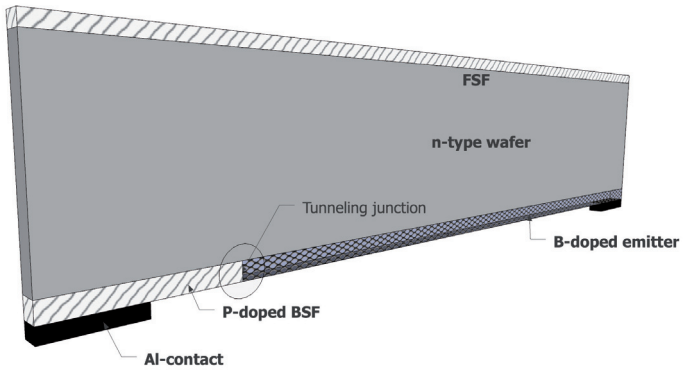

Figure 5.11: Schematic drawing of a BC-BJ silicon solar cell, including the tunneling junction. FSF and BSF are the front and back-surface fields, respectively.

clearly seen in the figure. The characteristic negative differential resistance region can be seen as a bump at low forward applied voltage, and is caused by BBT. Trap-assisted tunneling is the dominant tunneling mechanism in the forward applied voltage region around the maximum powerpoint, indicating that it will have a negative influence on the performance of a silicon solar cell. The effect of reducing the doping concentration to 1×10^{19} cm^{-3} can be seen in Figure 5.13. The negative resistance region is no longer visible in the curve, but the current density in the forward applied voltage region is still dominated by TAT. A more thorough discussion of quantum mechanical tunneling in back-junction silicon solar cells, can be found in paper VI.

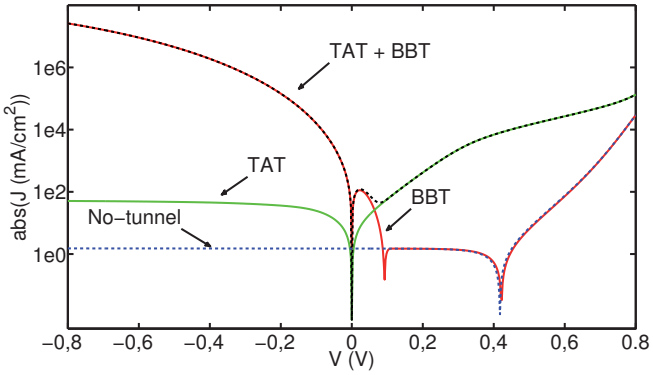

Figure 5.12: Current-density (absolute value)−voltage curves of an illuminated tunneling junction. The doping concentration was 5×10^{19} cm^{-3} on both sides of an abrupt junction. The different curves are result from simulations of the same p-n junction but with different tunneling mechanisms enabled. BBT and TAT are abbreviations for band-to-band and trap-assisted tunneling, respectively.

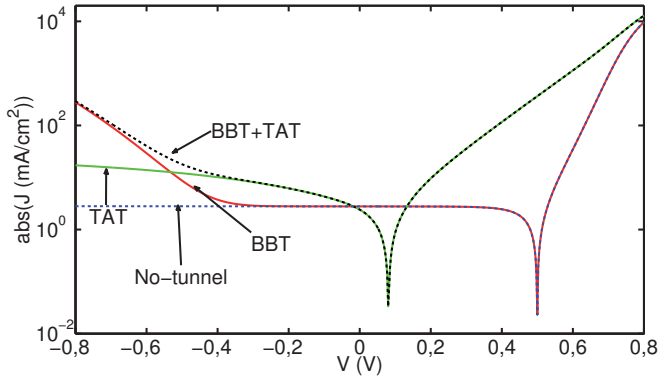

Figure 5.13: Current-density (absolute value)−voltage curves of an illuminated tunneling junction. The doping concentration was 1×10^{19} cm^{-3} on both sides of an abrupt junction. The different curves are result from simulations of the same p-n junction but with different tunneling mechanisms enabled. BBT and TAT are abbreviations for band-to-band and trap-assisted tunneling, respectively.

Chapter 6

Conclusions

In this thesis I have studied several important issues regarding back-contacted back-junction (BC-BJ) silicon solar cells. The work has been done both through experiments and simulations. The results are mainly presented in the six appended papers, while the background for the cell concept, experiments, and simulations are covered in the previous chapters of the thesis. In addition, two patents have been filed based on work presented herein. The main conclusions are summarized and presented below.

In the experimental work I have focused on the use of laser as a processing tool. A diode pumped, frequency doubled, Nd:YVO_4 green (532 nm) laser with pulse duration in the nanosecond regime was used in all the experiments. This laser is industrially well proven and relatively cheap. I showed how large areas of silicon could be ablated (removed) from a monocrystalline silicon wafer with this laser and subsequent etching in an aqueous KOH solution without degrading the minority carrier lifetime in the processed areas. The ablation was done with the aim of structuring a BC-BJ silicon solar cell, and high minority carrier lifetimes are necessary in order to obtain high conversion efficiencies in this solar cell design. A laser pulse fluence (energy density) of 2.0 J/cm^2 at a repetition frequency of 20 kHz with a spot to spot distance overlap of 75 % were found to give the best results with subsequent etching in an aqueous KOH solution with a concentration of 55 % (weight) at 80 °C. I also demonstrated how the same laser could be used

to make holes in a double passivating layer of amorphous silicon (a-Si) and silicon oxide (SiO_2) without damaging the underlying crystalline silicon wafer. The holes were opened with the aim of making local contacts on the back of a BC-BJ silicon solar cell. I explained how the high optical absorption and low thermal conductivity of a-Si were the key parameters to enable ablation of the covering SiO_2 with laser fluences five times lower than that needed to ablate crystalline silicon (c-Si) with the same laser. I also showed how the laser fluence threshold for SiO_2 ablation decreases with increasing thickness of the a-Si layer up to a thickness corresponding to the thermal diffusion length of a-Si. Furthermore, I looked in more detail on the interaction between laser and thin film a-Si on c-Si, and developed a thermodynamic model that was in good agreement with the previous experimental results. The model was able to predict the laser fluence threshold for SiO_2 ablation as a function of the a-Si thickness. The modeling also gave insight into the importance of the thermal resistance at the interface between a-Si and c-Si for the successful use of the laser in the damage-free ablation process. A thermal interface resistance of 0.0054 $cm^2 \cdot K/W$ gave the best match between the model and the experimental results. This resistance corresponds to an additional layer of native oxide between the two materials.

I investigated the quality of the laser ablated holes in the passivating double-layer of a-Si/SiO_2 by deposition of aluminum and use of the transfer length method to extract the specific contact resistance in the laser ablated holes. A specific contact resistance as low as 0.8 $m\Omega \cdot cm^2$ was measured for an a-Si layer with a thickness of 180 nm and a laser fluence of 0.59 J/cm^2. Despite our relatively standard laser, these results are better than what has been obtained by most state-of-the-art laser technologies using lasers with pulse durations in the pico- and femtosecond range. In order to investigate how the optimized specific contact resistance influences the performance of a full BC-BJ cell, I simulated the active area performance of a cell given the latest experimental results. The simulation model also included full optical loss analysis and so gave a good indication of the efficiency potential of the cell structure I have been working with. Given realistic values for material quality, physical parameters, and the size of the backside structures; I ended up with a simulated active area efficiency of 20.4 % on a 200 μm thick 2 $\Omega \cdot$cm n-type silicon wafer. The diffusion profiles used in the simulations were based on experimental,

and not fully optimized, results. There is also room for further improvement of the short-circuit current density by introducing slightly more advanced, but potentially costly, anti-reflection coating schemes than what was assumed in the ray tracing. Finally, tunneling mechanisms in the adjacent highly doped regions on the backside of a BC-BJ silicon solar cell was investigated through both device, process, and circuit simulations. I showed how so-called trap-assisted tunneling can have a deleterious effect on the efficiency of a silicon solar cell through a reduced shunt-resistance, and thus fill-factor. Band-to-band tunneling, on the other hand, does not influence the performance of a solar cell near the preferred operating point on the current-voltage curve, and so does not effect the efficiency. Band-to-band tunneling does, however, lead to current breakdowns at low to moderate reverse voltages. This implies that potential hotspots can be avoided under reverse voltage, as the heat dissipation will be distributed throughout the whole junction region. This cell type therefore has the potential of operating in a solar module without the need for bypass diodes.

Still, much work remains to be able to finalize a full version of a BC-BJ silicon solar cell. Processing steps related to the front-side have not been studied (experimentally). Texturization, anti-reflection coatings, passivation, and front-surface fields are all important parts of a successfully working back-junction cell. The metallization scheme used herein has been found suitable for small lab-scale solar cells, however, for large-area cells alternatives or a revised version of the sputtered aluminum need to be investigated.

Finally, it is also important to point out that most of the results obtained herein might separately be as useful for other solar cell designs as for BC-BJ silicon solar cells. Especially the idea of using a-Si as a combined passivation and laser irradiation buffer layer should be attractive for local contacting in both high-efficiency front-contacted cells as well as in other back-contacted silicon solar cell designs.

Appendix

Erratum

In paper II we investigated ablation of large areas of silicon from a silicon wafer. The work was done prior to proper measurements of laser beam characteristics. We therefore assumed the $\frac{1}{e^2}$ diameter of the laser spot to be 20 μm in focus, based on information from the laser system manufacturer. Later, by measuring the laser spot diameter by a BC106-VIS CCD camera beam profiler from Thorlabs, we found the actual $\frac{1}{e^2}$ diameter to be 40 μm in focus, and thus the information from the manufacturer erroneous. This implies that the optimized laser parameters obtained in paper II of 50 % spot to spot distance overlap of a 20 μm wide laser spot, in reality was 75 % spot to spot distance overlap of a 40 μm wide laser spot, see Figure 6.1. This does not influence the final results in any way. The correct laser spot characteristic are used in the papers following paper II.

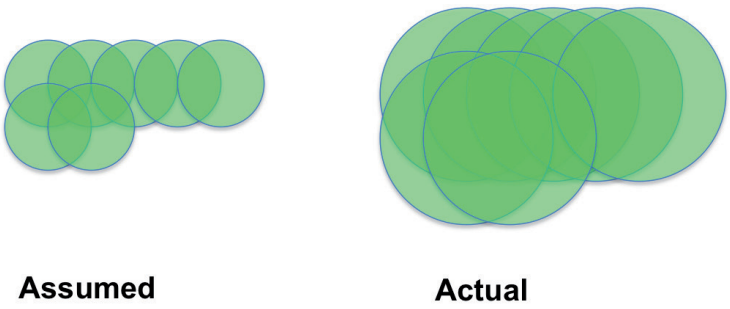

Figure 6.1: Left: Assumed 50 % spot to spot distance overlap for a laser spot with a diameter of 20 μm. **Right:** The actual 75 % spot to spot distance overlap for a laser spot with a diameter of 40 μm.

Abbreviations, physical parameters and constants

Abbreviations

Acronym	Description
AC	Alternating current
AM 1.5	Air mass 1.5 solar spectrum
BBT	Band-to-band tunneling
BC-BJ	Back-contacted back-junction
BGN	Bandgap narrowing
BSF	Back-surface field
CCD	Charge-coupled device
Cz	Czochralsky silicon
DC	Direct current
DFT	Density functional theory
DSBC	Double-side buried contact
EWT	Emitter-wrap-through
FCA	Free carrier absorption
FSF	Front-surface field
FWHM	Full width at half maximum
FZ	Float-zone silicon
GDP	Gross domestic product
HIT	Heterojunction with intrinsic thin layer
IBC	Interdigitated back-contacted
IEA	International Energy Agency

Acronym	Description
IFE	Institute for Energy Technology
IFE-Solar	Institute for Energy Technology, Department of Solar Energy
IPCC	Intergovernmental Panel on Climate Change
ISFH	Institut für Solarenergieforschung Hameln
MWT	Metallization-wrap-through
PCD	Photoconductance decay
PECVD	Plasma-enhanced chemical vapor deposition
PV	Photovoltaic
RF	Radio frequency
RISE	Rear interdigitated single evaporation
SEM	Scanning electron microscopy
SIMS	Secondary ion mass spectroscopy
SOD	Spin-on-dopant
SPICE	Simulation program with integrated circuit emphasis
TAT	Trap-assisted tunneling
TEM	Transmission electron microscopy
TFT	Thin film transistor
UV	Ultraviolet
VASP	Vienna ab-initio simulation package

Physical parameters

Symbol	Description	Unit
A_n	Auger coefficient, electrons	cm^6/s
A_p	Auger coefficient, holes	cm^6/s
C	Volumetric heat capacity	$J/cm^3 \cdot K$
C	Capacitance	F
c_p	Specific heat capacity	J/g·K
$C_{p,\mathrm{aSi}}$	Volumetric heat capacity of a-Si	$J/cm^3 \cdot K$
$C_{p,\mathrm{eff}}$	Effective volumetric heat capacity	$J/cm^3 \cdot K$
D	Thermal diffusivity	cm^2/s
d	Thickness of a-Si film	cm
d_BSF	Width of back-surface field	cm
d_i	Width of surface segment i in a simulation mesh	cm
d_s	Thickness of Si substrate	cm
E_p	Laser pulse energy	J
F	Fluence	J/cm^2
F_P	Peak fluence	J/cm^2
F_T	Fluence threshold	J/cm^2
F_{TM}	Fluence threshold for melting	J/cm^2
F_{TV}	Fluence threshold for vaporization	J/cm^2
FF	Fill factor	%
g_E	Generation rate	$cm^{-3}s^{-1}$
I	Optical intensity	W/cm^2
J	Current density	A/cm^2
J_0	Saturation current density	A/cm^2
J_{dark}	Current density in the dark	A/cm^2
J_{0e}	Emitter saturation current density	A/cm^2
J_S	Shifted current density	A/cm^2
J_{SC}	Short-circuit current density	A/cm^2
k	Optical extinction coefficient	
l_a	Optical absorption length	cm
L_T	Transfer length	cm
l_{th}	Thermal diffusion length	cm

Symbol	Description	Unit
$l_{th,\text{eff}}$	Effective thermal diffusion length	cm
$L_{\max}$	Maximum required diffusion length	μm
m	Local ideality factor	
n	Refractive index	
n	Electron concentration	cm^{-3}
n_0	Reference electron concentration	cm^{-3}
N_A	p-type doping concentration	cm^{-3}
N_D	n-type doping concentration	cm^{-3}
N_{eff}	Effective doping concentration	cm^{-3}
N_{ref}	Reference doping concentration	cm^{-3}
n_t	Density of electron traps	cm^{-3}
$\tilde{n}$	Complex refractive index	
p	Hole concentration	cm^{-3}
p_0	Reference hole concentration	cm^{-3}
P_{in}	Input power density	W/cm^2
P_{out}	Output power density	W/cm^2
P_{sun}	Power density incident from the sun	W/cm^2
p_t	Density of hole traps	cm^{-3}
Q	Total energy release	J
Q_{abs}	Absorbed laser energy density	J/cm^3
R	Reflection coefficient	
R_{int}	Thermal interface resistance	$\text{cm}^2\cdot\text{K/W}$
R_S	Series resistance	Ω
R_S	Sheet resistance	Ω
R_{SH}	Shunt resistance	Ω
R_a	Surface roughness	μm
R_i	Resistance at node i in a simulation mesh	Ω
S	Laser source power density	W/cm^3
S	Surface recombination velocity	cm/s
S_0	Reference surface recombination velocity	cm/s
S_{eff}	Effective emitter recombination velocity	cm/s
T	Absolute temperature	K

Symbol	Description	Unit
T_0	Ambient temperature	K
t	time	s
t_{auger}	Auger recombination lifetime	s
t_{rad}	Radiation recombination lifetime	s
t_{SRH}	Shockley-Read-Hall recombination lifetime	s
$t_{surface}$	Surface recombination lifetime	s
t_{bulk}	Bulk recombination lifetime	s
t_{peak}	Time for peak fluence	s
U	Recombination rate	$cm^{-3}s^{-1}$
U_{AUG}	Auger recombination rate	$cm^{-3}s^{-1}$
U_{SRH}	Shockley-Read-Hall recombination rate	$cm^{-3}s^{-1}$
V	Voltage	V
V_{OC}	Open-circuit voltage	V
V_{th}	Thermal voltage	V
W	Wafer thickness	μm
w	Width of unit cell in third dimension	cm
α	Absorption coefficient	cm^{-1}
α_{fc}	Absorption coefficient for free carriers	cm^{-1}
β	Absorption coefficient	cm^{-1}
ΔE_g	Change in bandgap due to doping	V
ΔH	Total enthalpy	J/cm^3
ΔH_m	Enthalpy of melting	$J/cm^3 \cdot K$
ΔH_v	Enthalpy of vaporization	$J/cm^3 \cdot K$
Δn	Excess electron density	cm^{-3}
Δp	Excess hole density	cm^{-3}
ΔT	Temperature increment	K
ΔT_M	Needed temperature increment for melting	K
ΔT_V	Needed temperature increment for vaporization	K
ϵ_t	Critical energy density	J/cm^3
η	Efficiency	%
κ	Thermal conductivity	$W/cm \cdot K$
κ_{aSi}	Thermal conductivity of a-Si	$W/cm \cdot K$

Symbol	Description	Unit
κ_{Si}	Thermal conductivity of Si	W/cm·K
κ_{total}	Total thermal conductivity of multi-layer	W/cm·K
λ	Wavelength	cm
μ_n	Electron mobility	cm^2/V·s
μ_n	Hole mobility	cm^2/V·s
ϕ_0	$1/e^2$ radius of a Gaussian beam profile	cm
ρ	Mass density	$\mathrm{g/cm}^3$
ρ_c	Specific contact resistance	$\Omega\cdot\mathrm{cm}^2$
σ_p	Photoconductance	S
τ_e	Emitter recombination lifetime	s
τ_{eff}	Effective lifetime	s
τ_p	Laser pulse duration	s
Θ	Heaviside function	

Physical constants

Symbol	Description	Value
k	Boltzmann's constant	1.38065×10^{-23} J·K^{-1}
n_i	Intrinsic carrier density in silicon	1.01×10^{10} cm^{-3}
q	Elementary charge	1.60218×10^{-19} C

Bibliography

[1] British Petroleum (BP). Statistical review of world energy. Technical report, 2009.

[2] International Energy Agency (IEA). Key world energy statistics. Technical report, 2009.

[3] U.S. Census Bureau. World population 1950-2050. Technical report, 2009.

[4] K. Aleklett, M. Hook, K. Jakobsson, M. Lardelli, S. Snowden, and B. Soderbergh. The peak of the oil age - analyzing the world oil production reference scenario in world energy outlook 2008. *Energy Policy*, 38(3): 1398–1414, 2010.

[5] N. A. Owen, O. R. Inderwildi, and D. A. King. The status of conventional world oil reserves-hype or cause for concern? *Energy Policy*, 38(8):4743–4749, 2010.

[6] Cambridge Energy Research Associates (CERA). CERA says peak oil theory is faulty. Technical report, 2006.

[7] The White House. The ongoing administration-wide response to the Deepwater BP oil spill. Press Release, May 5 2010.

[8] Intergovernmental Panel on Climate Change (IPCC). Summary for policymakers. Technical report, 2007.

[9] Renewable energy policy network for the 21st century (REN21). Renewables global status report. Technical report, 2009.

[10] M. Ito, K. Kato, K. Komoto, T. Kichimi, and K. Kurokawa. A comparative study on cost and life-cycle analysis for 100 MW very large-scale PV (VLS-PV) systems in deserts using m-Si, a-Si, CdTe, and CIS modules. *Progress in Photovoltaics: Research and Applications*, 16(1):17–30, 2008.

[11] U.S. Department of Energy. What is the energy payback for PV? Technical report, 2008.

[12] International Energy Agency (IEA). Technology roadmap for solar photovoltaic energy. Technical report, 2010.

[13] Solar Buzz. Www.Solarbuzz.com; Solar cell technologies, 2010.

[14] R. M. Swanson. A vision for crystalline silicon photovoltaics. *Progress in Photovoltaics: Research and Applications*, 14(5):443–453, 2006.

[15] E. Van Kerschaver and G. Beaucarne. Back-contact solar cells: A review. *Progress in Photovoltaics: Research and Applications*, 14(2):107–123, 2006.

[16] R. J. Schwartz and M. D. Lammert. Silicon solar cells for high concentration applications. In *IEEE International Electron Devices Meeting*, pages 350–352, 1975.

[17] D. De Ceuster, P. Cousins, D. Rose, D. Vicente, P. Tipones, and W. Mulligan. Low-cost, high-volume production of >22 % efficiency silicon solar cells. In *22nd European Photovoltaic Solar Energy Conference*, pages 816–19, 2007.

[18] P. J. Cousins, D. D. Smith, H.-C. Luan, J. Manning, T. D. Dennis, A. Waldhauer, K. E. Wilson, G. Harley, and W. P. Mulligan. Generation 3: Improved performance at lower cost. In *35th IEEE Photovoltaic Specialists Conference*, pages 275 – 278, 2010.

[19] W. Shockley and H. J. Queisser. Detailed balance limit of efficiency of p-n junction solar cells. *Journal of Applied Physics*, 32(3):510–519, 1961.

[20] A. E. Becquerel. Memoire sur les effets electriques produits sous l'influence des rayons solaires. *Les Compte Rendus des L'academie des sciences*, 9:561–567, 1839.

[21] J. Zhao, A. Wang, and M. A. Green. 24.5 % efficiency silicon PERT cells on MCZ substrates and 24.7 % efficiency PERL cells on FZ substrates. *Progress in photovoltaics: Research and Applications*, 7(6):471–474, 1999.

[22] M. A. Green, K. Emery, Y. Hishikawa, and W. Warta. Solar cell efficiency tables (version 37). *Progress in Photovoltaics: Research and Applications*, 19:84–92, 2011.

[23] M. A. Green, K. Emery, Y. Hishikawa, and W. Warta. Solar cell efficiency tables (version 33). *Progress in Photovoltaics: Research and Applications*, 17(1):85–94, 2009.

[24] O. Schultz, S. W. Glunz, and G. P. Willeke. Multicrystalline silicon solar cells exceeding 20 % efficiency. *Progress in Photovoltaics: Research and Applications*, 12(7):553–558, 2004.

[25] Z. Shi, S. Wenham, and J. Ji. Mass production of new high efficiency multicrystalline silicon solar cell technology with selective emitter. In *24th European Photovoltaic Solar Energy Conference*, pages 1090 – 1093, 2009.

[26] M. Köntges, M. Gast, R. Brendel, R. Meyer, A. Giegerich, and P. Merz. A novel photovoltaic-module assembly system for back contact solar cells using laser soldering technique. In *23rd European Photovoltaic Solar Energy Conference*, pages 2709–2712, 2008.

[27] M. Späth, P. C. de Jong, I. J. Bennett, T. P. Visser, and J. Bakker. A novel module assembly line using back contact solar cells. In *33rd IEEE Photovoltaic Specialists Conference*, Vols 1-4, pages 708–713, 2008.

[28] F. Granek, M. Hermle, D. M. Huljic, O. Schultz-Wittmann, and S. W. Glunz. Enhanced lateral current transport via the front n+ diffused layer

of n-type high-efficiency back-junction back-contact silicon solar cells. *Progress in Photovoltaics: Research and Applications*, 17(1):47–56, 2009.

[29] J. M. Gee, W. K. Schubert, and P. A. Basore. Emitter wrap-through solar-cell. In *23rd IEEE Photovoltaic Specialists Conference*, pages 265–270, 1993.

[30] E. Van Kerschaver, R. Einhaus, J. Szlufcik, J. Nijs, and R. Mertens. A novel silicon solar cell structure with both external polarity contacts on the back surface. In *2nd World Conference on Photovoltaic Energy Conversion.*, pages 1479–1482, 1998.

[31] M. D. Lammert and R. J. Schwartz. Interdigitated back contact solar cell: Silicon solar-cell for use in concentrated sunlight. *IEEE Transactions on Electron Devices*, 24(4):337–342, 1977.

[32] R. M. Swanson, S. K. Beckwith, R. A. Crane, W. D. Eades, Y. H. Kwark, R. A. Sinton, and S. E. Swirhun. Point-contact silicon solar cells. *IEEE Transactions on Electron Devices*, 31(5):661–664, 1984.

[33] R. A. Sinton and R. M. Swanson. Design criteria for Si point-contact concentrator solar cells. *IEEE Transactions on Electron Devices*, 34(10):2116–2123, 1987.

[34] R. A. Sinton and R. M. Swanson. Simplified backside-contact solar cells. *IEEE Transactions on Electron Devices*, 37(2):348–352, 1990.

[35] K. R. McIntosh, M. J. Cudzinovic, D. D. Smith, W. P. Mulligan, and R. M. Swanson. The choice of silicon wafer for the production of low-cost rear-contact solar cells. In *3rd World Conference on Photovoltaic Energy Conversion.*, pages 971–974, 2003.

[36] R. A. Sinton, P. Verlinden, D. E. Kane, and R. M. Swanson. Development efforts in silicon backside-contact solar cells. In *8th E.C. Photovoltaic Solar Energy Conference.*, pages vol.2 1472–6, 1988.

[37] M. J. Cudzinovic and K. R. McIntosh. Process simplifications to the Pegasus solar cell - SunPower's high-efficiency bifacial silicon solar cell. In *29th IEEE Photovoltaic Specialists Conference*, pages 70–73, 2002.

[38] P. Engelhart, N. P. Harder, A. Merkle, R. Grischke, R. Meyer, and R. Brendel. RISE: 21.5 % efficient back-junction silicon solar cell with laser technology as a key processing tool. In *IEEE 4th World Conference on Photovoltaic Energy Conversion*, pages 5 pp.|CD–ROM, 2006.

[39] P. Engelhart, S. Hermann, T. Neubere, H. Plagwitz, R. Grischke, R. Meyd, U. Klug, A. Schoonderbeek, U. Stute, and R. Brendel. Laser ablation of SiO_2 for locally contacted Si solar cells with ultra-short pulses. *Progress in Photovoltaics: Research and Applications*, 15(6):521–527, 2007.

[40] P. Engelhart, R. Grischke, S. Eidelloth, R. Meyer, A. Schoonderbeek, U. Stute, A. Ostendorf, and R. Brendel. Laser processing for back-contacted silicon solar cells. In *25th International Congress on Applications of Lasers and Electro-Optics*, page M703, 2006.

[41] P. Engelhart, N. P. Harder, R. Grischke, A. Merkle, R. Meyer, and R. Brendel. Laser structuring for back junction silicon solar cells. *Progress in Photovoltaics: Research and Applications*, 15(3):237–243, 2007.

[42] F. Granek. *High-efficiency back-contact back-junction silicon solar cells.* PhD thesis. Fraunhofer Institute für Solare Energiesysteme, Freiburg im Breisgau, 2009.

[43] S. W. Glunz, S. Rein, J. Knobloch, W. Wettling, and T. Abe. Comparison of boron- and gallium-doped p-type Czochralski silicon for photovoltaic application. *Progress in Photovoltaics: Research and Applications*, 7(6): 463–469, 1999.

[44] J. H. Guo, B. S. Tjahjono, and J. E. Cotter. 19.2 % efficiency n-type laser-grooved silicon solar cellls. In *21st IEEE Photovoltaic Specialists Conference*, pages 983–986, 2005.

[45] D. Macdonald and L. J. Geerligs. Recombination activity of interstitial iron and other transition metal point defects in p- and n-type crystalline silicon. *Applied Physics Letters*, 85(18):4061–4063, 2004.

[46] S. Martinuzzi, O. Palais, M. Pasquinelli, and F. Ferrazza. n-type multicrystalline silicon wafers and rear junction solar cells. *European Physical Journal-Applied Physics*, 32(3):187–192, 2005.

[47] J. E. Cotter, J. H. Guo, P. J. Cousins, M. D. Abbott, F. W. Chen, and K. C. Fisher. p-type versus n-type silicon wafers: Prospects for high-efficiency commercial silicon solar cells. *IEEE Transactions on Electron Devices*, 53 (8):1893–1901, 2006.

[48] M. Taguchi, Y. Tsunomura, H. Inoue, S. Taira, T. Nakashima, T. Baba, T. Sakata, and E. Maruyama. High-efficiency HIT solar cell on thin (<100 μm) silicon wafer. In *24th European Photovoltaic Solar Energy Conference*, pages 1690 – 1693, 2009.

[49] M. H. Rein. Wet chemical wafer cleaning of muliticrystalline silicon. Master's thesis. Department of Mathematical Science and Technology, University of Lifesciences, 2007.

[50] H. Seidel, L. Csepregi, A. Heuberger, and H. Baumgartel. Anisotropic etching of crystalline silicon in alkaline-solutions. 1. Orientation dependence and behavior of passivation layers. *Journal of the Electrochemical Society*, 137(11):3612–3626, 1990.

[51] H. Seidel, L. Csepregi, A. Heuberger, and H. Baumgartel. Anisotropic etching of crystalline silicon in alkaline-solutions. 2. Influence of dopants. *Journal of the Electrochemical Society*, 137(11):3626–3632, 1990.

[52] S. A. Campbell. *Bulk Micromachining Etching Techniques*, chapter 19, pages 527–535. Oxford Univeristy Press, 2001.

[53] M. M. Noor, B. Bais, and B. Y. Majlis. The effects of temperature and KOH concentration on silicon etching rate and membrane surface roughness. In

IEEE International Conference on Semiconductor Electronics, pages 524–528, 2002.

[54] Oxford Instruments, Tubney Woods, Abingdon, Oxfordshire, OX13 5QX, UK.

[55] E. D. Palik. Handbook of optical constants, 2007. ISBN 978-1-60119-270-7.

[56] D. G. Cahill, M. Katiyar, and J. R. Abelson. Thermal-conductivity of a-Si:H thin-films. *Physical Review B*, 50(9):6077–6081, 1994.

[57] C. K. Ong, H. S. Tan, and E. H. Sin. Calculations of melting threshold energies of crystalline and amorphous materials due to pulsed-laser irradiation. *Materials Science and Engineering*, 79(1):79–85, 1986.

[58] B. S. W. Kuo, J. C. M. Li, and A. W. Schmid. Thermal-conductivity and interface thermal-resistance of Si film on Si substrate determined by photothermal displacement interferometry. *Applied Physics a-Materials Science & Processing*, 55(3):289–296, 1992.

[59] S. Volz, X. Feng, C. Fuentes, P. Guerin, and M. Jaouen. Thermal conductivity measurements of thin amorphous silicon films by scanning thermal microscopy. *International Journal of Thermophysics*, 23(6):1645–1657, 2002.

[60] G. Kresse and J. Hafner. Ab-initio molecular-dynamics for liquid-metals. *Physical Review B*, 47(1):558–561, 1993.

[61] G. Kresse and J. Hafner. Ab-initio molecular-dynamics simulation of the liquid-metal amorphous-semiconductor transition in germanium. *Physical Review B*, 49(20):14251–14269, 1994.

[62] G. Kresse and J. Furthmuller. Efficiency of ab-initio total energy calculations for metals and semiconductors using a plane-wave basis set. *Computational Materials Science*, 6(1):15–50, 1996.

[63] G. Kresse and J. Furthmuller. Efficient iterative schemes for ab-initio total-energy calculations using a plane-wave basis set. *Physical Review B*, 54 (16):11169–11186, 1996.

[64] A. Bentzen, A Ulyashin, E. Sauar, D. Grambole, D. N. Wright, E. S. Marstein, B. G. Svensson, and A. Holt. Surface passivation of silicon solar cells by amorphous silicon/silicon nitride dual layers. In *15th international Photovoltaic Science and Engineering Conference*, pages 316–317, 2005.

[65] J. Perrin, J. Schmitt, C. Hollenstein, A. Howling, and L. Sansonnens. The physics of plasma-enhanced chemical vapour deposition for large-area coating: Industrial application to flat panel displays and solar cells. *Plasma Physics and Controlled Fusion*, 42:B353–B363, 2000.

[66] A. J. Flewitt, S. Lin, W. I. Milne, R. B. Wehrspohn, and M. J. Powell. Characterization of defect removal in hydrogenated and deuterated amorphous silicon thin film transistors. *Journal of Non-Crystalline Solids*, 352(9-20): 1700–1703, 2006.

[67] S. Guha. Light-induced effects in amorphous-silicon alloys - Design of solar-cells with improved stability. *Journal of Non-Crystalline Solids*, 77-8:1451–1460, 1985.

[68] D. L. Staebler and C. R. Wronski. Reversible conductivity changes in discharge-produced amorphous Si. *Applied Physics Letters*, 31(4):292–294, 1977.

[69] D. L. Staebler and C. R. Wronski. Optically induced conductivity changes in discharge-produced hydrogenated amorphous silicon. *Journal of Applied Physics*, 51(6):3262–3268, 1980.

[70] M. Hofmann, C. Schmidt, N. Kohn, J. Rentsch, S. W. Glunz, and R. Preu. Stack system of PECVD amorphous silicon and PECVD silicon oxide for silicon solar cell rear side passivation. *Progress in Photovoltaics: Research and Applications*, 16(6):509–518, 2008.

[71] M. Hofmann, S. Janz, C. Schmidt, S. Kambor, D. Suwito, N. Kohn, J. Rentsch, R. Preu, and S. W. Glunz. Recent developments in rear-surface passivation at Fraunhofer ISE. *Solar Energy Materials and Solar Cells*, 93 (6-7):1074–1078, 2009.

[72] D. N. Wright. *Optical and passivating properties of amorphous hydrogenated silicon nitride deposited by plasma enhanced chemical vapor deposition for application on silicon solar cells*. PhD thesis. Physics Department, University of Oslo, 2008.

[73] D. D. Smith and J. M. Gee. Review of back contact silicon solar cells for low cost application. In *16th European Photovoltaics Solar Energy Conference*, pages 1104–1107, 2000.

[74] A. G. Ulyashin, A. Bentzen, S. Diplas, A. Suphellen, A. E. Gunnaes, A. Olsen, B. C. Svensson, E. S. Marstein, A. Holt, D. Grambole, and E. Sauar. Hydrogen release and defect formation during heat treatments of SiN_x:H/a-Si:H double passivation layer on c-Si substrate. In *4th IEEE World Conference on Photovoltaic Energy Conversion*, page 4, 2006.

[75] M. Schaper, J. Schmidt, H. Plagwitz, and R. Brendel. 20.1 %-efficient crystalline silicon solar cell with amorphous silicon rear-surface passivation. *Progress in Photovoltaics: Research and Applications*, 13(5):381–386, 2005.

[76] A. G. Aberle. Surface passivation of crystalline silicon solar cells: A review. *Progress in Photovoltaics: Research and Applications*, 8(5):473–487, 2000.

[77] D. Bauerle. *Laser Processing and Chemistry*. Springer, 2 edition, 1996.

[78] G. E. Jellison and F. A. Modine. Optical absorption of silicon between 1.6 and 4.7 eV at elevated temperatures. *Applied Physics Letters*, 41(2): 180–182, 1982.

[79] B. Rezek, C. E. Nebel, and M. Stutzmann. Laser beam induced currents in polycrystalline silicon thin films prepared by interference laser crystallization. *Journal of Applied Physics*, 91(7):4220–4228, 2002.

[80] O. Yavas, N. Do, A. C. Tam, P. T. Leung, W. P. Leung, H. K. Park, C. P. Grigoropoulos, J. Boneberg, and P. Leiderer. Temperature dependence of optical properties for amorphous silicon at wavelengths of 632.8 nm and 752 nm. *Optics Letters*, 18(7):540–542, 1993.

[81] H. Kobatake, H. Fukuyama, I. Minato, T. Tsukada, and S. Awaji. Non-contact measurement of thermal conductivity of liquid silicon in a static magnetic field. *Applied Physics Letters*, 90(9), 2007.

[82] S. Tosto. Computer simulation of pulsed laser processing of amorphous Si. *Applied Physics a-Materials Science & Processing*, 71(3):285–297, 2000.

[83] A. Fell, D. Kray, and G. P. Willeke. Transient 3D/2D simulation of laser-induced ablation of silicon. *Applied Physics a-Materials Science & Processing*, 92(4):987–991, 2008.

[84] E. Matthias, M. Reichling, J. Siegel, O. W. Kading, S. Petzoldt, H. Skurk, P. Bizenberger, and E. Neske. The influence of thermal diffusion on laser-ablation of metal films. *Applied Physics a-Materials Science and Processing*, 58(2):129–136, 1994.

[85] A Bentzen. *Phosphorus Diffusion and Gettering in Silicon Solar Cells*. PhD thesis. Physics Department, Univeristy of Oslo, 2006.

[86] M. A. Kessler, T. Ohrdes, B. Wolpensinger, R. Bock, and N.-P. Harder. Characterisation and implications of the boron rich layer resulting from open-tube liquid source BBr_3 boron diffusion processes, 2009.

[87] A. Cuevas. The effect of emitter recombination on the effective lifetime of silicon wafers. *Solar Energy Materials and Solar Cells*, 57(3):277–290, 1999.

[88] D. E. Kane and R. M. Swanson. Measurement of the emitter saturation current by a contactless photoconductivity decay method. In *8th IEEE Photovoltaic Specialists Conference*, pages 578–583, 1985.

[89] H. Nagel, C. Berge, and A. G. Aberle. Generalized analysis of quasi-steady-state and quasi-transient measurements of carrier lifetimes in semiconductors. *Journal of Applied Physics*, 86(11):6218–6221, 1999.

[90] R. A. Sinton, A. Cuevas, and M. Stuckings. Quasi-steady-state photoconductance, a new method for solar cell material and device characterization. In *25th IEEE Photovoltaic Specialists Conference*, pages 457–460, 1996.

[91] D. K. Schroder and D. L. Meier. Solar Cell Contact Resistance - A Review. *IEEE Transactions on Electron Devices*, 31(5):637–647, 1984.

[92] D. L. Meier and D. K. Schroder. Contact Resistance - Its Measurement and Relative Importance to Power Loss in a Solar Cell. *IEEE Transactions on Electron Devices*, 31(5):647–653, 1984.

[93] N.-P. Harder, S. Hermann, A. Merkle, T. Neubert, T. Brendemuhl, P. Engelhart, R. Meyer, and R. Brendel. *Laser-processed high-efficiency silicon RISE-EWT solar cells and characterisation*, volume 6 of *Physica Status Solidi C-Current Topics in Solid State Physics*, pages 736–743. Wiley-V C H Verlag Gmbh, Weinheim, 2009.

[94] R. Hezel. High-efficiency OECO Czochralski-silicon solar cells for mass production. *Solar Energy Materials and Solar Cells*, 74(1-4):25–33, 2002.

[95] R. Hezel. Novel back-contact silicon solar cells designed for very high efficiencies and low-cost mass production. In *29th IEEE Photovoltaic Specialists Conference*, pages 114–117, 2002.

[96] J. W. Muller, A. Merkle, and R. Hezel. Self-aligning, industrially feasible back contacted silicon solar cells with efficiencies > 18 %. In *3rd World Conference on Photovoltaic Energy Conversion*, pages 1403–1406, 2003.

[97] Silvaco-Atlas. Atlas user's manual, Dated April 20, 2010.

[98] Silvaco-Atlas. Silvaco Inc., 4701 Patrick Henry Drive, Bldg 2, Santa Clara, CA 95054.

[99] F. Granek, M. Hermle, and S. W. Glunz. Analysis of the current linearity at low illumination of high-efficiency back-junction back-contact silicon solar cells. *Physica Status Solidi-Rapid Research Letters*, 2(4):151–153, 2008.

[100] M. Hermle, F. Granek, O. Schultz, and S. W. Glunz. Analyzing the effects of front-surface fields on back-junction silicon solar cells using the charge-collection probability and the reciprocity theorem. *Journal of Applied Physics*, 103(5), 2008.

[101] M. Hermle, Granek. F, S. W. Glunz, and O. Schults-Wittman. Shading effects in back-junction back-contacted silicon solar cells. In *33rd IEEE Photovoltaic Specialist Conference*, 2008.

[102] TracePro. Lambda Research Corporation, 25 Porter Road Littleton, MA 01460.

[103] D. Thorp and S. R. Wenham. Ray tracing of arbitrary surface textures for light-trapping in thin silicon solar cells. *Solar Energy Materials and Solar Cells*, 48(1-4):295–301, 1997.

[104] M. A Green. *Silicon Solar Cells; Advanced Principles & Practice*. Center for Photovoltaic systems and devices, UNSW, Sydney, 1995.

[105] A. Cuevas, G. Giroult-Matlakowski, P. A. Basore, C. DuBois, and R. R. King. Extraction of the surface recombination velocity of passivated phosphorus-doped silicon emitters. In *24th IEEE Photovoltaic Specialists Conference*, volume 2, pages 1446–1449, 1994.

[106] A. Cuevas, P. A. Basore, G. Matlakowski, and C. Dubois. Surface recombination velocity of highly doped n-type silicon. *Journal of Applied Physics*, 80(6):3370–3375, 1996.

[107] J. Dziewior and W. Schmid. Auger coefficients for highly doped and highly excited silicon. *Applied Physics Letters*, 31(5):346–348, 1977.

[108] J. G. Fossum and D. S. Lee. A physical model for the dependence of carrier lifetime on doping density in nondegenerate silicon. *Solid-State Electronics*, 25(8):741–747, 1982.

[109] M. E. Law, E. Solley, M. Liang, and D. E. Burk. Self-consistent model of minority-carrier lifetime, diffusion length, and mobility. *IEEE Electron Device Letters*, 12(8):401–403, 1991.

[110] D. J. Roulston, N. D. Arora, and S. G. Chamberlain. Modeling and measurement of minority-carrier lifetime versus doping in diffused layers of n^+-p silicon diodes. *IEEE Transactions on Electron Devices*, 29(2):284–291, 1982.

[111] J. W. Slotboom. pn-product in silicon. *Solid-State Electronics*, 20(4):279–283, 1977.

[112] J. R. Hauser and P. M. Dunbar. Performance limitations of silicon solarcells. *IEEE Transactions on Electron Devices*, 24(4):305–321, 1977.

[113] H. P. D. Lanyon and R. A. Tuft. Bandgap narrowing in moderately to heavily doped silicon. *IEEE Transactions on Electron Devices*, 26(7):1014–1018, 1979.

[114] J. W. Slotboom and H. C. Degraaff. Measurements of bandgap narrowing in Si bipolar-transistors. *Solid-State Electronics*, 19(10):857–862, 1976.

[115] J. del Alamo, S Swirhun, and R.M. Swanson. Simultaneous measuring of hole lifetime, hole mobility, and bandgap narrowing in heavily doped n-type silicon. *IEDM Technical Digest*, pages 290–293, 1985.

[116] M. A. Green. Modelling implications of recent silicon bandgap narrowing expressions. *Progress in Photovoltaics: Research and Applications*, 5(4): 261–263, 1997.

[117] J. O. Schumacher, P. P. Altermatt, G. Heiser, and A. G. Aberle. Application of an improved band-gap narrowing model to the numerical simulation of recombination properties of phosphorus-doped silicon emitters. *Solar Energy Materials and Solar Cells*, 65(1-4):95–103, 2001.

[118] A. Schenk. Finite-temperature full random-phase approximation model of band gap narrowing for silicon device simulation. *Journal of Applied Physics*, 84(7):3684–3695, 1998.

[119] L. Esaki. Discovery of the tunnel-diode. *IEEE Transactions on Electron Devices*, 23(7):644–647, 1976.

[120] E. O. Kane. Theory of tunneling. *Journal of Applied Physics*, 32(1):83–91, 1961.

[121] G. A. M. Hurkx, D. B. M. Klaassen, and M. P. G. Knuvers. A new recombination model for device simulation including tunneling. *IEEE Transactions on Electron Devices*, 39(2):331–338, 1992.

[122] M. Hermle, S. P. Philipps, G. Letay, and A. W. Bett. Numerical simulation of tunnel diodes and multi-junction solar cells. In *33rd IEEE Photovoltaic Specialists Conference*, pages 58–61, 2008.

[123] A. Hermle, G. Letay, S. P. Philipps, and A. W. Bett. Numerical simulation of tunnel diodes for multi-junction solar cells. *Progress in Photovoltaics: Research and Applications*, 16(5):409–418, 2008.

[124] J. H. Guo, P. J. Cousins, and J. E. Cotter. Investigations of parasitic shunt resistance in n-type buried contact solar cells. *Progress in Photovoltaics: Research and Applications*, 14(2):95–105, 2006.

Appended papers

Paper I

K. Mangersnes and S. E. Foss. "Numerical optimization of a back-junction solar cell." Proceedings of the 22nd EUROPEAN PHOTOVOLTAIC SOLAR ENERGY CONFERENCE, pages 1701-1704, Milano 2007.

Paper II

K. Mangersnes and S.E. Foss, "Laser ablation of PECVD oxide for structuring of interdigitated silicon solar cells". Proceedings of the 24th EUROPEAN PHOTOVOLTAIC SOLAR ENERGY CONFERENCE, pages 2001-2003, Hamburg 2009.

Paper III

K. Mangersnes, S. E. Foss, and A. Thøgersen. "Damage free laser ablation of SiO_2 for local contact opening on silicon solar cells using an a-Si:H buffer layer." JOURNAL OF APPLIED PHYSICS, 107, 043528, 2010.

Damage free laser ablation of SiO_2 for local contact opening on silicon solar cells using an a-Si:H buffer layer

Krister Mangersnes,[a] Sean Erik Foss, and Annett Thøgersen
Institute for Energy Technology, Department of Solar Energy, Instituttveien 18, 2007 Kjeller, Norway

(Received 30 October 2009; accepted 8 January 2010; published online 23 February 2010)

We have used a Q-switched $Nd:YVO_4$, diode pumped 532 nm laser with nanosecond pulses, and a spot diameter of 40 μm to ablate a layer of plasma enhanced chemical vapor deposited (PECVD) SiO_2 on n-type Cz silicon, with the aim of making local contact openings on back-junction silicon solar cells. Laser pulses within the ns range are usually believed to be incompatible with processing of high efficiency solar cells because such long pulses induce too much damage into the underlying silicon lattice. This is due to thermal dissipation. In this work, a PECVD layer of a-Si:H between the n-type silicon and the dielectric layer is shown to absorb much of the laser radiation and allows for ablation at laser fluences lower than the ablation threshold of crystalline silicon. In addition, the a-Si:H layer serves as an excellent surface passivation layer for the silicon substrate. We show that it is possible to ablate PECVD SiO_2 in a damage free way with fluences five times lower than those needed to ablate crystalline Si. Our results are verified experimentally with high resolution transmission electron microscopy of the crystal structure in the laser irradiated areas, and quasi-steady-state photoconductance measurements of emitter saturation currents. In addition, we have simulated the energy transfer from a ns 532 nm Gaussian shaped laser beam to a SiO_2 covered Si lattice with and without the a-Si:H buffer layer. A model that coincides very well with the experiments is found. © *2010 American Institute of Physics*. [doi:10.1063/1.3309382]

I. INTRODUCTION

Back-contacted silicon solar cells have served as an alternative to conventional solar cells for more than 30 years.[1] Several different solar cell designs, such as metallization-wrap-through, emitter-wrap-through, and back-junction cells, have been developed.[2] Back-junction solar cells have both the emitter and the complete metallization on the rear side. This eliminates the contact shading present in conventional solar cells. The sunward surface and back-side of the solar cell can therefore be independently optimized for optical and electrical performance, respectively. Moreover, having both contacts on the back side may significantly simplify module assembly, and allow for an increased packing density of the cells.[2] Back-junction solar cells require high quality monocrystalline silicon wafers with long minority carrier lifetimes and excellent surface passivation. Low surface recombination losses in silicon solar cells can be obtained by passivating the surface by SiO_2, SiN_x, a-Si, Al_2O_3, and different stacks thereof,[3–9] and by limiting the metal semiconductor contact area. Lasers have in the recent years been shown to be a very promising tool for making local contact openings to silicon through a dielectric layer.[10–13] Cell concepts that earlier only have been possible to realize in low throughput, high-cost laboratory facilities are expected to enter the commercial market in the coming years. Lasers with pulses within the nanosecond range are usually believed to be unsuitable for local contact opening through SiO_2 and other dielectrics. This is because oxide is transparent to the most commonly used wavelengths, and the ablation takes place through an indirect process where the SiO_2 is lifted off as a result of thermal expansion of molten or vaporized silicon.[10,14,15] The relatively long laser pulses will affect the underlying silicon through heat dissipation. Laser energies above the ablation threshold have been shown to be detrimental to the minority carrier lifetime.[16–18] The extent of the thermal diffusion can be approximated by[14]

$$I_d = 2\sqrt{\alpha t}, \tag{1}$$

where I_d is the thermal penetration depth, α is the thermal diffusivity, and t is the pulse length of the laser. In silicon, the thermal penetration depth of a 100 ns long laser pulse will be around 3 μm at 1000 K.[15] In this paper, we show that local contact can be made with a ns laser without damaging the crystalline silicon, and thus maintain a high minority carrier lifetime, which is a necessity in high efficiency silicon solar cells. Our solution is to add a buffer layer of plasma enhanced chemical vapor deposited (PECVD) a-Si:H (a-Si for simplicity) between the oxide and the silicon, and utilize the thermal diffusivity of a-Si, which is two orders of magnitude lower than that of silicon,[14] to isolate the laser damage. The higher optical absorption coefficient of a-Si compared to crystalline silicon also contributes to the concentration of laser energy within the a-Si buffer layer.

II. EXPERIMENTAL

n-type Cz 1–3 Ω cm Si wafers were used in all the experiments. Before processing, the wafers were cleaned in piranha ($H_2SO_4:H_2O_2$, 4:1) and HF (5%).

[a]Electronic addresses: krister.mangersnes@ife.no and kristermangersnes@gmail.com.

A. Laser ablation energy threshold

We prepared one set of wafers for laser fluence ablation threshold experiments. Laser fluence is the pulse energy density, and it is given in units of J/cm^2. We refer in the following to the laser fluence at the peak of the Gaussian beam profile. The laser we used was a Q-switched $Nd:YVO_4$, diode pumped 532 nm laser with nanosecond pulses, and a $1/e^2$ spot diameter of 40 μm. For these experiments, the wafers were cut into four parts. Thereafter, a PECVD layer of a-Si of varying thickness (0–1000 nm) was deposited on the different samples. The samples were then covered with 500 nm of PECVD SiO_2. The thickness of the a-Si layer was measured by a variable angle spectroscopic ellipsometer. Each sample was exposed to the same matrix of single laser pulses with varying fluence in the range $0.1-2$ J/cm^2. In this energy range, the pulse duration decreases close to linearly with increasing fluence, from 150 ns at 0.1 J/cm^2 to 80 ns at 2 J/cm^2. We then determined the ablation threshold of the oxide by visual inspection in an optical microscope.

B. Local emitter saturation current

A set of four wafers was prepared for phosphorus doping. Each wafer was doped on both sides by spraying on a diluted phosphorus containing dopant source with a custom-built spray-on system and subsequent drying and indiffusion in a belt furnace. The phosphorus source was P509 from Filmtronics. Similarly, four wafers were boron-doped with boron-A from Filmtronics as a dopant source. A third set of four wafers was left undoped. The diffused phosphorus layers had a sheet resistivity of 50 ± 5 $\Omega/\blacksquare$ (measured on a p-type wafer added for monitoring the sheet resistance), while the more shallow boron emitters had sheet resistivities of 150 ± 20 $\Omega/\blacksquare$. After the diffusion, the phosphorus and boron containing glass layers were removed in HF (5%) and in a belt furnace. The required back side surface passivation for lifetime measurements was obtained by depositing a thin layer of a-Si on the back side of the samples by parallel plate PECVD in an Oxford Plasmalab 133 system. The amorphous layer was deposited at 230 °C with a flow of 25 SCCM (SCCM denotes standard cubic centimeter per minute at STP) of undiluted silane (SiH_4). On two wafers of each set, nondiffused, phosphorus diffused, and boron-diffused, a thicker layer of a-Si was deposited on the front side. All the wafers were then covered with 500 nm of PECVD SiO_2 and cut into four samples of equal size. The different samples were exposed to a matrix of single laser pulses, covering approximately 20% of the sample area. The laser fluence was varied from 0.2 to 1.4 J/cm^2. After the laser ablation, the SiO_2 was stripped off in HF (5%). Thereafter, a new thin layer of a-Si was deposited on the front of all samples, using the same method as before. Finally, all samples were annealed for 2 min at 450 °C in a belt furnace.

We used quasi-steady-state photoconductance technique measurements under high injection conditions to extract the local emitter saturation current.[19–21] The effective saturation current before and after laser ablation was used together with the fraction, a, of the laser ablated area to the total sample area to calculate the emitter saturation current in the laser ablated spots. $J_{oe,eff}=a\times J_{oe}+(1-a)\times J_{oe,pass}$, where $J_{oe,eff}$ is the effective emitter saturation current, J_{oe} is the local emitter saturation current in the laser ablated spots, and $J_{oe,pass}$ is the emitter saturation current of the passivated sample before laser ablation. This gives $J_{oe}=a^{-1}[J_{oe,eff}-(1-a)\times J_{oe,pass}]$ for the local emitter saturation current in the laser radiated spots. A similar analysis was done by Engelhart *et al.*[10] when comparing contact openings made by ns and picosecond lasers.

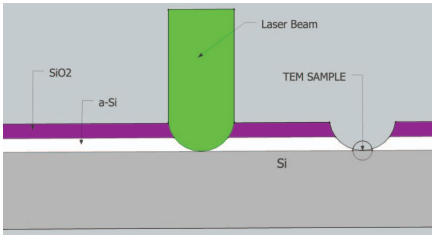

FIG. 1. (Color) The figure shows the laser ablation sequence and the cross section area used for TEM analysis.

C. Transmission electron microscopy

High resolution transmission electron microscopy (HR-TEM) was used to analyze the defects induced in the crystal lattice from the laser ablation at different laser energies with and without an a-Si buffer layer of 500 nm. We used a 200 keV JEOL 2010F microscope equipped with a Gatan imaging filter and detector. Cross sectional samples were prepared by gluing two sample substrates together, front to front, with epoxy glue. The cross sectional samples were thinned using ion-milling with a Gatan precision ion-polishing system operated at 5 kV gun voltage. Figure 1 shows the laser ablation process sequence, and the cross section area used for TEM analysis.

III. SIMULATIONS

We used the ATLAS device simulator, within the Silvaco simulation framework,[22] to simulate the energy transfer from a laser beam to a SiO_2 covered silicon substrate with and without a 500 nm thick a-Si buffer layer between the oxide and the silicon. The simulations were done to illustrate the general idea presented herein, of using an optically and thermally absorbing buffer layer for avoiding defect formation in the silicon substrates. They do not, however, give an exact measure of any physical quantity. In the simulations, a 532 nm Gaussian shaped laser beam, with a pulse duration of 90 ns was directed normally toward the surface of the two different samples. The ramping time of the beam was set to 100 ps. A low beam power was used to avoid temperatures near the melting point of a-Si and Si, as the device simulator is not meant to handle phase transitions. The heat capacity of the a-Si layer was modeled according to Endo *et al.*[23] as

$$C_p = 13.1 + 2.25\times10^{-2}T - 8.3\times10^{-6}T^2 \quad (\mathrm{Jmol^{-1}\,K^{-1}}), \tag{2}$$

where C_p is the molar heat capacity and T is the temperature ranging from 300 to 1000 K. The heat conductivity of a-Si

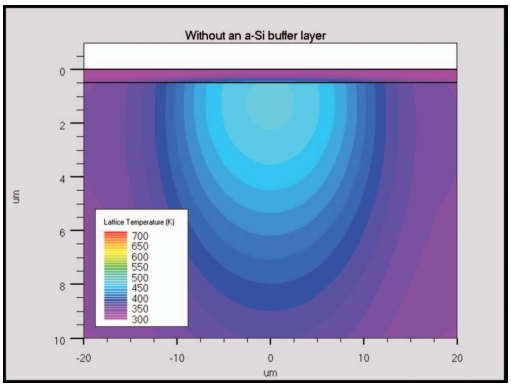

FIG. 2. (Color) The temperature distribution in a Si sample covered with 500 nm SiO_2 after a 90 ns laser pulse. The wavelength and beam width was 532 nm and 20 μm, respectively, and the beam power was set to 1×10^8 W/cm^2. The axis units are in μm.

was assumed to be a constant value of 0.010 W/cm-K.[14,23] The simulated heat distribution after one single laser pulse for the two samples without and with the a-Si layer is shown in Figs. 2 and 3, respectively. These figures clearly show that the a-Si layer concentrates the laser energy both optically and thermally, thereby confining the damage to a smaller volume.

IV. RESULTS AND DISCUSSION

A. Laser ablation energy threshold

The fluence needed to ablate the PECVD SiO_2 on bare silicon was determined experimentally to be 1.5 J/cm^2, but with a 500 nm thick layer of a-Si between the silicon and the oxide the ablation fluence threshold was reduced to a much lower value of 0.3 J/cm^2. We found that the ablation threshold decreases with an increasing thickness of the a-Si layer, as shown in Fig. 4. Already at an a-Si thickness of 25 nm, the

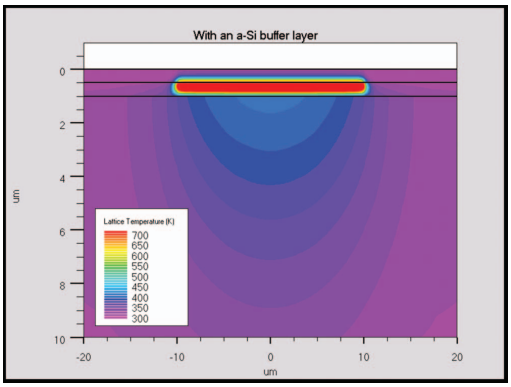

FIG. 3. (Color) The temperature distribution in a Si sample covered with 500 nm a-Si and 500 nm SiO_2 after a 90 ns laser pulse. The wavelength and beam width was 532 nm and 20 μm, respectively, and the beam power was set to 1×10^8 W/cm^2. The axis units are in μm.

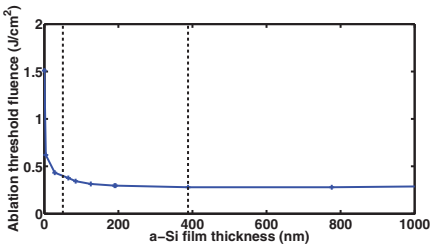

FIG. 4. (Color online) The laser ablation fluence threshold vs the thickness of the a-Si layer. The data can be divided into three different regions, as indicated in the figure, an exponentially decreasing region, a linearly decreasing region, and a constant threshold fluence region.

fluence ablation threshold is reduced to less than one third of the fluence needed to ablate SiO_2 on crystalline silicon. For a-Si films thinner than approximately 40 nm, there is an exponential decay in the laser fluence ablation threshold. We believe that the exponentially decreasing ablation threshold with increasing film thickness is a result of more energy being optically absorbed in the a-Si film rather than being transmitted through to the silicon substrate where the energy will be less spatially confined. For thicker films, where the optical absorption is no longer a limiting factor, we find a linear decrease in ablation threshold, before the laser fluence ablation threshold reaches a constant value for films thicker than approximately 400 nm. The onset of the constant fluence ablation threshold is equal to our estimated thermal diffusion length of a-Si. A thermal diffusion length of 400 nm corresponds to a thermal diffusivity of 3.5×10^{-3} cm^2/s, two orders of magnitude less than of that of crystalline silicon.[14] The laser fluence ablation threshold for thin metal films on fused silica was studied by Matthias *et al.*,[24] who also developed a thermodynamic model for the fluence ablation threshold of the thin film. They found a linear and a constant region, both experimentally and theoretically, but in their case with a linear decrease in the threshold fluence with increasing film thickness. The energy density in the metal film decreases with increasing film thickness since the substrate is a poor thermal conductor compared to the metal film. The fluence ablation threshold was found to be constant for films equal to or thicker than the thermal diffusion length of the metal film. In our case, the substrate is a better thermal conductor than the film, and more heat will dissipate into the substrate as the film gets thinner. This is the reason why we have opposite linear dependence in the two cases. The exponentially decreasing region was not observed by Matthias *et al.*[24] due to the very short optical penetration depth of the metals studied, and the short wavelength of the laser, but it was discussed that this region should exist only if the model would be valid. Figure 5 shows an optical microscope image of contact openings locally ablated with the ns laser, at fluences just above the ablation threshold of the a-Si layer. It should also be noted that we have tested the variation in the laser fluence ablation threshold energy with varying annealing times and temperatures of the a-Si layer. For temperatures up to 500 °C only very small changes in the ablation threshold energy was found. We, therefore, believe

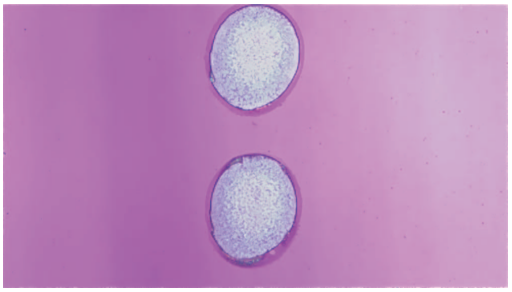

FIG. 5. (Color) An optical microscope picture of local contact openings of SiO_2 ablated together with a buffer layer of amorphous silicon on a crystalline silicon sample. The laser fluence used to make the openings was about 0.3 J/cm^2; five times lower then the laser fluence needed to ablate crystalline silicon. The diameter of the ablated spots is 20 μm.

that the amount of hydrogen in the a-Si layer is not important for the laser fluence ablation threshold energy.

B. Local emitter saturation current

The emitter saturation current gives an indication of the electronic quality of the emitter. It is a measure of the total recombination taking place in the emitter, also including surface recombination, recombination at laser induced defects, and band gap narrowing.[25–27] For a diffused emitter the saturation current can be given in terms of the effective surface recombination velocity through

$$S_{\text{eff}} = \frac{J_{\text{oe,eff}} N_{\text{A}}}{n_{\text{i}}^2}, \tag{3}$$

where S_{eff} is the effective surface recombination velocity, $J_{\text{oe,eff}}$ the emitter saturation current, N_{A} is the doping level of the diffused emitter, and n_{i} the intrinsic carrier density.[3] In the absence of a diffused emitter, as for the undoped samples, $J_{\text{o,eff}}$ will give an indication of the surface passivation quality. Figure 6 shows the local emitter saturation current and the local saturation current for the doped and undoped samples, respectively, as a function of the laser fluence for the samples prepared without the extra a-Si layer. For the undiffused samples J_{o} increases with increasing laser fluence, indicating that the laser damage reduces the minority

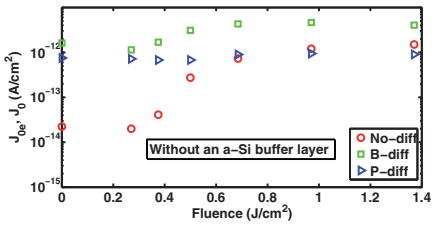

FIG. 6. (Color online) Local emitter saturation current density and local saturation current density for the doped and undoped samples, respectively, as a function of laser fluence for samples without an a-Si buffer layer, shown for undiffused samples (circles), P-diffused samples (triangles), and B-diffused samples (squares). The reference values for the nonablated samples are shown at zero fluence.

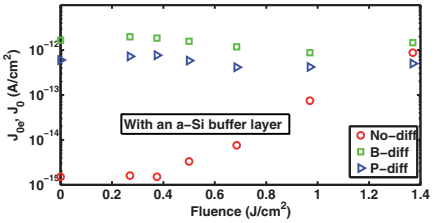

FIG. 7. (Color online) Local emitter saturation current density and local saturation current density for the doped and undoped samples, respectively, as a function of laser fluence for samples with a 500 nm thick a-Si buffer layer, shown for undiffused samples (circles), P-diffused samples (triangles), and B-diffused samples (squares). The reference values for the nonablated samples are shown at zero fluence.

carrier lifetime. However, for small laser fluences J_{o} seems more or less unaffected by the laser pulse. The same trend is also seen for the shallow (150 $\Omega/\blacksquare$) boron emitter. For the deeper phosphorus emitter (50 $\Omega/\blacksquare$), no effect of the laser pulse can be seen from the figure. The fluctuation in J_{oe} observed in Fig. 6 is most likely to result from a small spread in sheet resisitivity over the wafer. The effect of increasing emitter damage is less pronounced for the samples prepared with a buffer layer of a-Si. This is shown in Fig. 7. In the low laser fluence region, near the a-Si ablation threshold, J_{o} of the undiffused samples seems to be more or less unaffected by the laser ablation. It is also worth noting that the reference value of J_{o} at zero fluence for the undiffused samples is lower than the reference value of the corresponding samples without the buffer layer. We believe that this is because the relatively thick buffer layer of a-Si passivates the surface even better than the thin layer used for passivation. The threshold laser fluence where laser damage occurs is shifted to higher fluences compared to the experiments without an a-Si layer. The same can be seen for the shallow boron emitters. As for the phosphorus doped samples, there seems to be little influence from the laser irradiation on the local emitter saturation current.

C. Damage to the crystal structure

Figure 8 shows a HRTEM picture of a sample that was prepared with 500 nm a-Si under the oxide layer. The sample was exposed to single laser pulses with fluences just above the minimum ablation threshold of SiO_2 on a-Si. The SiO_2 is stripped off, as before, but it can also be seen that the a-Si layer has been locally removed. Still, there is no visible damage to the crystalline silicon. Several HRTEM pictures were taken, and no visible damage could be found on this sample. This was also indicated by the emitter saturation current measurements, showing no increase with low laser fluences compared to the nonlaser processed reference. We found that a laser fluence of 0.3 J/cm^2, which corresponds to the minimum ablation threshold fluence of SiO_2 on a-Si, is not enough to cause visible damage to the crystal lattice even without the a-Si buffer layer. This implies that we are able to make local contact through an a-Si–SiO_2 stack without damaging the underlying crystalline silicon. A more thorough analysis of the HRTEM induced defects will be presented

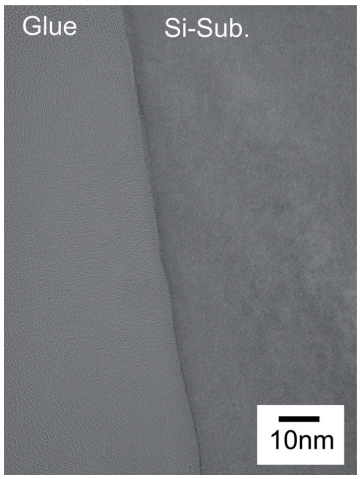

FIG. 8. HRTEM picture of a sample where the SiO_2 and the buffer layer of a-si have been ablated with a single laser pulse without any damage to the silicon crystal structure. The fluence used was 0.3 J/cm^2.

elsewhere,[28] but a short summary follows. For laser fluences above 0.5 J/cm^2, the a-Si layer has been found to reduce the density of laser induced defects significantly. In addition, the a-Si buffer layer changes the nature of the defects. For samples prepared without the a-Si layer the laser pulse seems to amorphize large parts of the crystalline substrate. With the a-Si buffer layer the same laser fluence does not cause the crystalline silicon to amorphize but induces stacking faults and twins. Figure 9 shows a sample that was also prepared with a 500 nm a-Si layer under the oxide. The sample was exposed to single laser pulses. Each with a fluence of 0.8 J/cm^2, and the damage to the crystal structure is easily seen from the picture. The damage origins from a specific depth of 26 nm under the silicon surface. Several HRTEM pictures were taken on this sample, and the same defects at the same specific depth were found on every picture. The details of the HRTEM experiments will be presented in an upcoming article.[28]

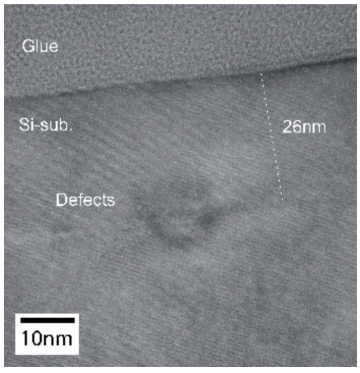

FIG. 9. HRTEM picture of a sample where the SiO_2 and the buffer layer of a-Si have been ablated with a single laser pulse. The fluence used was 0.8 J/cm^2, and considerable damage has been induced to the silicon crystal structure.

V. CONCLUSION

We have shown that it is possible to locally ablate a dielectric layer on silicon in a damage free way with the use of a long pulsed laser by adding a buffer layer of a-Si between the dielectric and the silicon. The a-Si has a larger optical absorption coefficient, and the thermal diffusivity is more than two orders of magnitude lower than that of crystalline silicon. Therefore, the laser energy will be confined to a much smaller volume, and the ablation takes place at significantly lower fluences. The laser fluence needed to ablate a-Si film decreases with increasing film thickness upto a thickness of 400 nm, corresponding to our estimated thermal penetration depth of a-Si, where the threshold energy reaches its minimum value of 0.3 J/cm^2. a-Si is also known to be an excellent surface passivation layer for both p- and n-type silicon solar cells. We believe that this general idea, of introducing an absorbing and insulating a-Si buffer layer, will be even more relevant for lasers with shorter pulse durations, as the thickness of the a-Si layer and thereby the deposition time can be significantly reduced.

ACKNOWLEDGMENTS

The authors would like to thank Gunnar Rustad, Øystein Farsund, and Magnus W. Haakestad at the Norwegian Defense Research Establishment for valuable help and advice regarding measurements of the laser characteristics.

[1] R. J. Schwartz and M. D. Lammert, 1975 International Electron Devices Meeting, Vol.21, pp. 350–352.
[2] E. Van Kerschaver and G. Beaucarne, Prog. Photovoltaics **14**, 107 (2006).
[3] A. G. Aberle, Prog. Photovoltaics **8**, 473 (2000).
[4] A. Bentzen, A. Ulyashin, E. Sauar, D. Grambole, D. Wright, E. S. Marstein, B. Svensson, and A. Holt, 15th International Photovoltaic Science and Engineering Conference (Shanghai, China, 2005), pp. 316–317.
[5] S. Gatz, H. Plagwitz, P. P. Altermatt, B. Terheiden, and R. Brendel, Appl. Phys. Lett. **93**, 173502 (2008).
[6] B. Hoex, J. Schmidt, R. Bock, P. P. Altermatt, M. C. M. van de Sanden, and W. M. M. Kessels, Appl. Phys. Lett. **91**, 112107 (2007).
[7] P. Panek, K. Drabczyk, A. Fosca, and A. Slaoui, Mater. Sci. Eng., B **165**, 64 (2009).
[8] M. Schaper, J. Schmidt, H. Plagwitz, and R. Brendel, Prog. Photovoltaics **13**, 381 (2005).
[9] A. G. Ulyashin, A. Bentzen, S. Diplas, A. Suphellen, A. E. Gunnaes, A. Olsen, B. C. Svensson, E. S. Marstein, A. Holt, and D. Grambole, Fourth IEEE World Conference on Photovoltaic Energy Conversion (Waikoloa, Hawaii, 2006), Vol. 4, pp.4.
[10] P. Engelhart, S. Hermann, T. Neubere, H. Plagwitz, R. Grischke, R. Meyd, U. Klug, A. Schoonderbeek, U. Stute, and R. Brendel, Prog. Photovoltaics **15**, 521 (2007).
[11] P. Engelhart, N. P. Harder, R. Grischke, A. Merkle, R. Meyer, and R. Brendel, Prog. Photovoltaics **15**, 237 (2007).
[12] S. Hermann, T. Neubert, B. Wolpensinger, N. P. Harder, and R. Brendel, 23rd European Photovoltaic Solar Energy Conference (Valencia, Spain, 2008).
[13] A. Knorz, M. Peters, A. Grohe, C. Harmel, and R. Prett, Prog. Photovoltaics **17**, 127 (2009).
[14] D. Bauerle, *Laser Processing and Chemistry*, 2nd ed. (Springer, Berlin, 1996).
[15] H. R. Shanks, P. D. Maycock, P. H. Sidles, and G. C. Danielson, Phys. Rev. **130**, 350 (1963).
[16] P. Engelhart, R. Grischke, S. Eidelloth, R. Meyer, A. Schoonderbeek, U.

Stute, A. Ostendorf, and R. Brendel, 25th International Congress on Applications of Lasers and Electro-Optics—ICALEO (Scottsdale, AZ, 2006).
[17]K. Mangersnes and S. Foss, 24th European Photovoltaic Solar Energy Conference (Hamburg, Germany, 2009).
[18]M. D. Abbott, Ph.D. thesis, University of New South Wales, Centre for Photovoltaic Engineering, 2006.
[19]A. Cuevas, Sol. Energy Mater. Sol. Cells **57**, 277 (1999).
[20]R. A. Sinton and A. Cuevas, Appl. Phys. Lett. **69**, 2510 (1996).
[21]R. A. Sinton, A. Cuevas, and M. Stuckings 25th IEEE Photovoltaic Specialists Conference, Washington, DC, 1996), pp. 457–460.
[22]Silvaco-Atlas, http://www.silvaco.com/
[23]R. K. Endo, Y. Fujihara, and M. Susa, High Temp. - High Press. **35/36**, 505 (2003).
[24]E. Matthias, M. Reichling, J. Siegel, O. W. Kading, S. Petzoldt, H. Skurk, P. Bizenberger, and E. Neske, Appl. Phys. A **58**, 129 (1994).
[25]R. R. King, R. A. Sinton, and R. M. Swanson, IEEE Trans. Electron Devices **37**, 365 (1990).
[26]R. R. King and R. M. Swanson, IEEE Trans. Electron Devices **38**, 1399 (1991).
[27]A. Cuevas, P. A. Basore, G. Matlakowski, and C. Dubois, J. Appl. Phys. **80**, 3370 (1996).
[28]A. Thøgersen, K. Mangersnes, and S. E. Foss, "A detailed TEM study of the structural defects in Si caused by laser ablation of SiO_2" *In Progress*.

Paper IV

K. Mangersnes and S. E. Foss. "A thermodynamic model for the laser fluence ablation threshold of PECVD SiO_2 on thin a-Si:H films deposited on crystalline silicon." AMORPHOUS AND POLYCRYSTALLINE THIN-FILM SILICON SCIENCE AND TECHNOLOGY, (Mater. Res. Soc. Symp. Proc. Volume 1245, A16.02 , 2010).

Mater. Res. Soc. Symp. Proc. Vol. 1245 © 2010 Materials Research Society 1245-A16-02

A thermodynamic model for the laser fluence ablation threshold of PECVD SiO_2 on thin a-Si:H films deposited on crystalline silicon

Krister Mangersnes and Sean E. Foss
Institute for Energy Technology, Solar Energy Department, Instituttveien 18, 2027 Kjeller, Norway.

ABSTRACT

We have developed a thermodynamic model that predicts the heat distribution in a stack of PECVD SiO_2 and a-Si:H on crystalline Si after laser irradiation. The model is based on solving the total enthalpy heat equation with a finite difference scheme. The laser used in the model is a frequency doubled Nd:YVO_4 green laser with pulse duration in the nanosecond range. The modeling was done with the aim of getting a better understanding of our newly developed laser ablation process for making local contacts on back-junction silicon solar cells. Lasers with pulse duration within the nanosecond range are usually believed to induce too much thermal damage into the underlying silicon to make them suitable for high efficiency solar cells. In our case, insertion of a thin layer of a-Si:H between the SiO_2 and the Si absorbs much of the laser irradiation both optically and thermally. This makes it possible to form local contacts to Si in a damage-free way. In addition, the residual a-Si:H serves as an excellent surface passivation layer for the Si substrate. We have also developed a simple static model to determine the onset of SiO_2 ablation on a-Si:H layers of varying thickness. The models, both the static and the dynamic, are in good agreement with experimental data.

INTRODUCTION

Lasers have in the recent years been shown to be a very promising tool for making local contacts on silicon solar cells through a dielectric layer[1-7]. The local ablation is done to reduce the total metal semiconductor area of the solar cells, and thus improve the efficiency of the device. Lasers in the nanosecond (ns) range are usually believed to induce too much thermal damage into the underlying silicon lattice to make them suitable for high efficiency solar cell concepts[4, 5, 8]. In the case of a frequency doubled Nd:YVO_4 green laser, SiO_2 is transparent to the laser light. Ablation of SiO_2 on Si takes place through an indirect process where the oxide is lifted off from expansion of molten or vaporized silicon. We have recently shown that insertion of a buffer layer of amorphous silicon, a-Si:H (a-Si for simplicity), between the SiO_2 and the Si will absorb much of the laser irradiation[7]. The high optical absorption and low thermal conductivity of a-Si compared to Si confines the laser energy to a much smaller volume. This makes it possible to ablate SiO_2 in a damage free way with a laser fluence five times lower than that needed to ablate SiO_2 on crystalline silicon. In addition, the residual a-Si serves as an excellent surface passivation layer for the Si substrate[9-11]. a-Si is not a very well defined material as most of the material parameters are very sensitive to the deposition technique and parameters. Especially the absorption coefficient and the thermal conductivity vary over a broad range according to different references[12-19]. Previous work on laser interaction with a-Si has mostly focused on melting and recrystallization of a-Si, both experimentally[15, 20-22] and numerically[21, 23-25]. The goal of this paper is to develop a thermodynamic model that predicts the laser fluence ablation threshold of SiO_2 on a-Si layers of varying thickness, and that also describes the heat distribution in the SiO_2 - a-Si - Si stack after laser irradiation.

THEORY

To find an expression for the laser fluence ablation threshold we make some simple assumptions. We assume that the onset of melting or vaporization is given by a critical energy density $E_T = F_T/L_{th,eff}$, where F_T is the threshold fluence. $L_{th,eff}$ is the effective thermal diffusion length defined by $L_{th} = \sqrt{2D_{eff}\tau_p}$, where D_{eff} is the effective thermal diffusivity and τ_p is the pulse duration of the laser at full width half maximum. D_{eff} is the ratio between the effective thermal conductivity, k_{eff}, and the volumetric heat capacity. k_{eff} is weighted between the thermal conductivity of a-Si and Si, also including a thermal resistance at the interface between the two. A version of this model, not including interface resistance, was proposed by Matthias et al., when investigating laser ablation of metal films on quartz[26]. Herein we also need to account for an optically absorbing substrate under the thin film. If we assume a uniform temperature rise throughout the volume defined by $L_{th,eff}$, it can be shown that the threshold fluence for melting is given by

$$F_{TM} = \frac{\Delta T_M}{(1-R)\left[(1-e^{-\alpha d}) + (1-e^{-\beta d_s})e^{-\alpha d}\right]} C_{P,eff} L_{th,eff} \tag{1}$$

ΔT_M is the needed temperature increment for melting, d and d_s are the thicknesses of the a-Si layer and the Si substrate, respectively. We assume that the transparent SiO_2 constitutes a thermal barrier and only influences the reflection, R, at the surface. α and β are the optical absorption coefficients of a-Si and Si, respectively. $C_{p,eff}$ is the effective volumetric heat capacity; linearly weighted between a-Si and Si. The corresponding model for the onset of surface vaporization is the same as for melting but with ΔT_M replaced by $\Delta Tv + \Delta H_m/C_{p.a\text{-}Si}$, where ΔTv is the needed temperature rise for vaporization, ΔH_m is the latent heat of melting, and $C_{p.a\text{-}Si}$ is the volumetric heat capacity of a-Si. The parameters used in the model are taken from Table I. We used the respective values at 1000 K for the temperature dependent parameters, and a pulse duration of 142 ns. Our experimental data from reference 7 is plotted together with the static thermodynamic models for surface melting and vaporization in Figure 1. There is a good fit between the experimental data and the static model for surface evaporation even without temperature dependent parameters, and with the assumption of a uniform temperature rise. Still, this model only gives an indication of the onset of evaporation and does not include any information about the actual temperature distribution within the film and the substrate. Neither have we taken into account that the pulse length of our laser varies with fluence as given in Table I. A more dynamic description that also includes phase transitions will require a solution of the total enthalpy version of the heat equation. The diameter of our laser spot is much wider than the thermal diffusion length of a-Si, and it is a good approximation to solve the one-dimensional version of the equation[27].

$$\frac{\partial \Delta H(x,t)}{\partial t} = \frac{\partial}{\partial x}\kappa(T)\left(\frac{\partial}{\partial x}T(x,t)\right) + S(x,t) \tag{2}$$

$\kappa(T)$ is the temperature dependent thermal conductivity, x is the depth from the top of the a-Si layer, and $S(x,t)$ is the laser source given by

$$S(x,t) = \sqrt{\frac{4\ln 2}{\pi}} \frac{(1-R)F \cdot \alpha}{\tau_p} \exp\left(-\alpha x - 4\ln 2 - \frac{(t-t_{peak})^2}{\tau_p^2}\right) \tag{3}$$

F is the fluence at the peak of the Gaussian pulse, and t_{peak} is the time for the peak fluence. The total enthalpy, ΔH, is given by[27]

$$\Delta H(T) \approx \int_{T_0}^{T} \rho(T')c_p(T')dT' + \eta(T-T_M)\Delta H_M + \eta(T-T_V)\Delta H_V \tag{4}$$

T_0 is the ambient temperature, and T_M and T_V are the melting and vaporization temperatures, respectively. η is the Heaviside function (1 or 0 if the argument is positive or negative, respectively) and ΔH_m and ΔH_v are the latent heat of melting and vaporization, respectively.

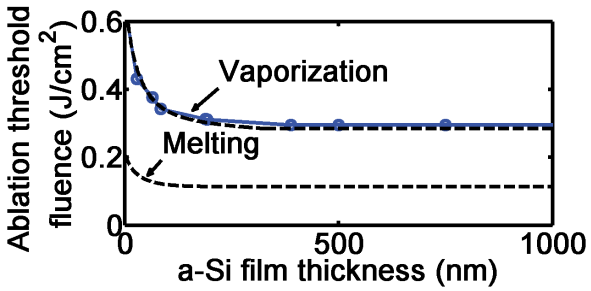

Figure 1: The fluence threshold for laser ablation as a function of the thickness of the a-Si film. Our experimental data from reference 7 (solid line with circles) is shown together with the modeled data for surface melting and vaporization.

To omit numerical instabilities we have assumed that the phase transitions occur over a temperature interval of $\Delta T = 5$ K. The SiO_2 is assumed to be optically transparent and thermally insulating, and is only influencing the surface reflection. The structure is at ambient temperature before the laser heating starts. We have used the following initial and boundary conditions:

$$T(x,t) = T_0\big|_{t=0} \qquad T(x,t) = T_0\big|_{x\to\infty} \qquad \frac{\partial T(x,t)}{\partial x} = 0\big|_{x=0} \tag{5}$$

A finite difference scheme was used to solve the total enthalpy heat equation. The simulation parameters are listed in Table I. a, c, and l in the table refer to amorphous Si, crystalline Si, and liquid Si, respectively

DISCUSSION

In Figure 2 we show the temperature distribution in a SiO_2 covered silicon wafer at different depths after laser irradiation with a single laser pulse with a fluence of 0.32 J/cm^2. In Figure 3 we show the temperature distribution in a similar sample, but now with a 300 nm buffer layer of a-Si. We observe that the a-Si obtains a much higher surface temperature, and that 0.32 J/cm^2 is enough to reach the onset of surface vaporization. This result, and also results for a-Si layers of different thicknesses (not shown) are in good agreement with our experimental data.

TABLE I

Parameters	Value/Expression	Reference
Absorption coefficient (cm^{-1})	a: 1.9×10^5	28
	c: $5.02\times10^3 e^{T/430}$	20
	l: 1×10^6	23
Density (g/cm^3)	a: 2.20	23
	c: 2.32	27
	l: 2.52	27
Thermal Conductivity (W/cm K)	a: $1.3\times10^{-11}\times (T-900)^3 + 1.3\times10^{-9}\times (T-900)^2 + 1\times10^{-6}\times (T-900) + 1\times10^{-2}$	20
	c: $1521/T^{1.226}$ (T<1200 K) $8.96/T^{0.502}$ (1200 K <= T <1690 K)	20
	l: 0.62	29
Heat capacity (J/cm^3 K)	a: $2.2\times(0.952 + 0.171\times T/685)$	20
	c: $2.32\times (0.711 +0.255\times (T^{1.85}-1)/(T^{1.85}-0.255/0.711)$	30
	l: 1.0	29
Melting temp (K)	a: 1420 c: 1690	27 27
Vaporization temp. (K)	l: 2680	27
Interface thermal resistance (cm^2 K/W)	0.0054	16
Latent heat of melting (J/K)	a: 1250	27
	c: 1780	27
Latent heat of Vaporization (J/K)	l: 15000	27
Reflection	a: 0.18	Measured
	c: 0.18	Measured
	l: 0.07	Calculated with data from ref 31
Pulse duration, full width at half maximum (ns)	$-37\times F + 154$	Measured. F is the peak fluence in the Gaussian beam profile (J/cm^2)
Pulse peak (ns)	200	Set

Interface thermal resistance

Kuo et al. measured the thermal resistance of the interface between a-Si films and crystalline Si[16]. The value we have used in our simulations, 0.54 mm^2 K/ W, is the resistance

they measured for a structure with a native oxide between the a-Si and the Si. This value was found to give the best fit between the modeling and our experiments. A clean surface, prepared by pre-sputtering in a vacuum chamber, showed an interface resistance of 0.15 mm^2 K/ W[16]. A lower interface resistance increases the laser fluence ablation threshold in our model, as less heat is contained in the film. The increased thermal resistance at the interface between a-Si and the Si (presumably provided by an oxide) is therefore a necessary element of our damage-free laser-ablation process.

CONCLUSIONS

We have developed a static thermodynamic model that describes the fluence threshold for pulsed laser ablation of SiO_2 on Si with a buffer layer of a-Si of varying thickness. We have also solved the heat equation for the SiO_2 – a-Si –Si stack to predict the temperature distribution within the a-Si film and the Si substrate. We found that an interface thermal resistance between a-Si and Si is important for lowering the laser fluence ablation threshold and for protecting the underlying silicon lattice. The results are in good agreement with our experimental data, when we include in the model the expected contribution from the native oxide layer to the thermal resistance of the interface.

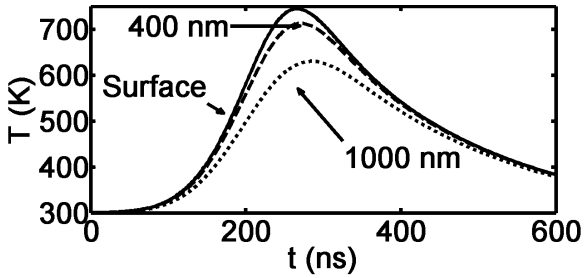

Figure 2: Heat distribution in Si as a function of time at different depths after single pulse laser irradiation with a fluence of 0.32 J/cm^2 and a pulse duration of 142 ns. $x = 0$ (surface) corresponds to the top of the Si substrate.

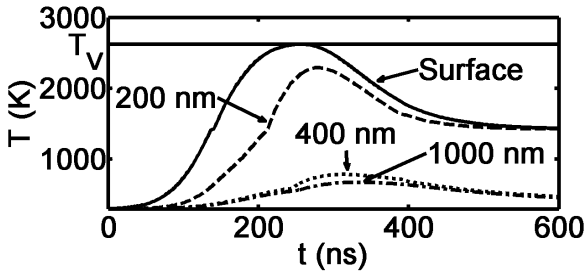

Figure 3: Heat distribution as a function of time at different depths in a stack of 300 nm a-Si on Si after single pulse laser irradiation with a fluence of 0.32 J/cm^2 and a pulse duration of 142 ns. *x = 0* (surface) corresponds to the top of the a-Si film.

REFERENCES

1. P. Engelhart, N. P. Harder, T. Horstmann, R. Grischke, R. Meyer and R. Brendel, Conference Record of the 2006 IEEE 4th World Conference on Photovoltaic Energy Conversion (IEEE Cat. No. 06CH37747), 4 pp.|CD-ROM (2006).
2. A. Grohe, C. Harmel, A. Knorz, S. W. Glunz, R. Preu, G. P. Willeke, presented at the 4th IEEE World Conference on Photovoltaic Energy Conversion, Vols 1 and 2, 2006.
3. P. Engelhart, N. P. Harder, R. Grischke, A. Merkle, R. Meyer and R. Brendel, Progress in Photovoltaics **15** (3), 237-243 (2007).
4. P. Engelhart, S. Hermann, T. Neubere, H. Plagwitz, R. Grischke, R. Meyd, U. Klug, A. Schoonderbeek, U. Stute and R. Brendel, Progress in Photovoltaics **15** (6), 521-527 (2007).
5. S. Hermann, T. Neubert, B. Wolpensinger, N.-P. Harder and R. Brendel, presented at the 23rd European Photovoltaic Solar Energy Conference, Valencia, Spain, 2008.
6. A. Knorz, M. Peters, A. Grohe, C. Harmel and R. Prett, Progress in Photovoltaics **17** (2), 127-136 (2009).
7. K. Mangersnes, S. E. Foss and A. Thøgersen, Journal of Applied Physics **107** (4) (2010).
8. K. Mangersnes and S. E. Foss, presented at the 24th European PVSEC, Hamburg, Germany, 2009.
9. A. G. Aberle, Progress in Photovoltaics **8** (5), 473-487 (2000).
10. A. Bentzen, A. Ulyashin, E. Sauar, D. Grambole, D. N. Wright, E. S. Marstein, B. G. Svensson and A. Holt, presented at the 15th international Photovoltaic Science and Engineering Conference, Shanghai, China, 2005.
11. M. Hofmann, C. Schmidt, N. Kohn, J. Rentsch, S. W. Glunz and R. Preu, Progress in Photovoltaics **16** (6), 509-518 (2008).
12. N. Attaf, M. S. Aida and L. Hadjeris, Solid State Communications **120** (12), 525-530 (2001).
13. D. G. Cahill, M. Katiyar and J. R. Abelson, Physical Review B **50** (9), 6077-6081 (1994).
14. R. K. Endo, Y. Fujihara and M. Susa, High Temperatures - High Pressures **35-36** (5), 505-511 (2003).
15. M. G. Grimaldi, P. Baeri, M. A. Malvezzi and C. Sirtori, International Journal of Thermophysics **13** (1), 141-151 (1992).
16. B. S. W. Kuo, J. C. M. Li and A. W. Schmid, Applied Physics a-Materials Science & Processing **55** (3), 289-296 (1992).
17. S. Moon, M. Hatano, M. H. Lee and C. P. Grigoropoulos, International Journal of Heat and Mass Transfer **45** (12), 2439-2447 (2002).
18. S. Volz, X. Feng, C. Fuentes, P. Guerin and M. Jaouen, International Journal of Thermophysics **23** (6), 1645-1657 (2002).
19. H. Wada and T. Kamijoh, Japanese Journal of Applied Physics Part 2-Letters **35** (5B), L648-L650 (1996).
20. C. K. Ong, H. S. Tan and E. H. Sin, Materials Science and Engineering **79** (1), 79-85 (1986).
21. Y. R. Chen, C. H. Chang and L. S. Chao, Journal of Crystal Growth **303** (1), 199-202 (2007).
22. L. Mariucci, A. Pecora, G. Fortunato, C. Spinella and C. Bongiorno, Thin Solid Films **427** (1-2), 91-95 (2003).
23. Z. Yuan, Q. Lou, J. Zhou, J. Dong, Y. Wei, Z. Wang, H. Zhao and G. Wu, Optics and Laser Technology **41** (4), 380-383 (2009).
24. S. Tosto, Applied Physics a-Materials Science & Processing **71** (3), 285-297 (2000).
25. C. H. Chang and L. S. Chao, International Communications in Heat and Mass Transfer **35** (5), 571-576 (2008).
26. E. Matthias, M. Reichling, J. Siegel, O. W. Kading, S. Petzoldt, H. Skurk, P. Bizenberger and E. Neske, Applied Physics a-Materials Science and Processing **58** (2), 129-136 (1994).
27. D. Bauerle, Laser Processing and Chemistry, 2 ed. (Springer, 1996).
28. E. D. Palik, Handbook of Optical Constants of Solids. (pp: 571-586), Elsevier.
29. H. Kobatake, H. Fukuyama, I. Minato, T. Tsukada and S. Awaji, Applied Physics Letters **90** (9) (2007).
30. V. Palankovski, R. Schultheis and S. Selberherr, IEEE Transactions on Electron Devices **48** (6), 1264-1269 (2001).
31. G. E. Jellison and D. H. Lowndes, Applied Physics Letters **51** (5), 352-354 (1987)

Paper V

K. Mangersnes, S. E. Foss, and J. Gjessing. "Investigating the specific contact resistance on boron emitters in laser ablated holes in a passivating double-layer of a-Si:H and a-SiO_x:H". Submitted to Solar Energy Materials and Solar Cells, Oct 2010.

Paper VI

K. Mangersnes and S. E. Foss. "Tunneling in back-junction silicon solar cells."
To be submitted to Solar Energy Materials and Solar Cells, 2010.